# Synthesis and Growth Mechanism of Two-Dimensional Atomic Sheets of Hexagonal Boron Nitride

内田，勇気

Synthesis and Growth Mechanism of

Two-Dimensional Atomic Sheets of Hexagonal Boron Nitride



A Dissertation Presented to Interdisciplinary Graduate School of

Engineering Sciences of Kyushu University



Yuki Uchida

2019

# Abstract

Hexagonal boron nitride (h-BN), a layered material composed of boron (B) and nitrogen (N) atoms, is expected to be an ideal dielectric layer for two-dimensional (2D) materials due to its atomically smooth and dangling bond-free surface, low polarizable surface optical phonons, and a layered structure, contributing to bring out intrinsic physical, electrical, and optical properties of 2D materials. Most of the previous studies have used mechanically exfoliated h-BN flakes obtained from bulk h-BN crystals using adhesive tape. However, the size of the exfoliated h-BN flakes is relatively small (1-30 $\mu$m) and they contain various thicknesses, limiting the developing of practical applications based on 2D materials, such as graphene and transition metal chalcogenides (TMCs). Chemical vapor deposition (CVD) utilizing catalytic substrates is expected to be a promising method to synthesize large-area h-BN film with controllable thickness and shape at low-cost. However, in contrast to CVD growth of monolayer graphene whose large scale growth has been reported by many groups, the CVD growth of h-BN with controlled thickness and lattice orientation has been a still challenging issue.

This thesis reports the epitaxial growth of monolayer h-BN on Cu(111) film and uniform growth of multilayer h-BN on Ni-Fe film in large-scale. In most of the previous works, polycrystalline metal catalysts have been used. Polycrystalline metal catalyst for the h-BN growth gives a h-BN sheet with different lattice orientations, resulting in the poorly connected small grains as well as inhomogeneous film thickness due to segregation from many grain boundaries existing in the metal catalyst. The Cu(111) film was prepared on a c-plane sapphire substrate by sputtering, allowing to grow highly oriented h-BN sheet with a monolayer thickness, as confirmed by scanning electron

microscope (SEM) and low-energy electron diffraction (LEED) measurements. Moreover, it was found that the epitaxially grown h-BN protects the Cu(111) surface from the oxidation in air in spite of its monolayer thickness.

In this thesis the uniform growth of multilayer h-BN using a Ni-Fe alloy film deposited on single-crystal spinel and sapphire substrates is also reported. The alloy film can tune the B and N solubilities in the metal catalyst and contribute to the controlling of the crystal structure during CVD process. This thesis also reveals the dynamics of h-BN growth on the alloy metal catalyst which is strongly dependent on the crystalline plane of the initial alloy. Moreover, the optical property of monolayer tungsten disulfide (WS$_2$) was found to be significantly improved when the WS$_2$ was grown on the CVD-grown multilayer h-BN. The result indicates that the present CVD-grown h-BN can be effective as a substrate for various 2D materials. This work is expected greatly contribute to the further development of 2D materials-based devices and other applications.

# Table of contents

**Abstract**

**Table of contents**

**Abbreviation**

# Abbreviation

0D: Zero-dimensional

1D: One-dimensional

2D: Two-dimensional

AFM: Atomic force microscopy

APS: Ammonium persulfate

ARPES: Angle-resolved photoemission spectroscopy

BSSE: Basis set superposition error

CB: Conduction band

CCD: Charge coupled device

CDW: Charge density wave

CL: Cathodoluminescence

CVD: Chemical vapor deposition

DFT: Density functional theory

DOS: Density of states

EBSD: Electron back scattered diffraction

EDX: Energy dispersive X-ray spectrometry

EELS: Electron energy loss spectroscopy

FET: field effect transistor

FIB: Focused-ion beam

FWHM: Full-width at half-maximum

GB: Grain boundarie

HF: Hartree-fock

HOPG: Highly oriented pyrolytic graphite

HPHT: High pressure and high remperature

IR: Infrared

LED: Light emitting diode

LEED: Low-energy electron diffraction

LMP2: Local second-order Møller-Plesset perturbation

LO: Longitudinal-optical

LPE: Liquid phase exfoliation

MBE: Molecular beam epitaxy

MOCVD: Metal organic chemical vapor deposition

PBEsol: Perdew-Burke-Ernzerhof revised for solid

PCT: Patent cooperation treaty

PDMS: Poly(dimethylsiloxane)

PL: Photoluminescence

PMMA: Poly(methyl methacrylate)

PVD: Physical vapor deposition

RDCP: Relative database citation potential

RF: Radio frequency

RIP: Raw impact per paper published in the journal

RMS: Root-mean-square

SEM: Scanning electron microscopy

SNIP: Source normalized impact per paper

SO: Surface optical

TEM: Transmission electron microscopy

TMC: Transition metal chalcogenide

TMDC: Transition metal dichalcogenide

TRT: Thermal release tape

VB: Valence band

WFC: Weighted fractional count

XPS: X-ray photoelectron spectroscopy

bcc: Body-centered cubic

c-BN: Cubic boron nitride

fcc: Face-centered cubic

h-BN: hexagonal boron nitride

hcp: Hexagonal close packed

r-BN: Rhombohedral boron nitride

vdW: van der Waals

w-BN: Wurtzite boron nitride

# Chapter 1

# Introduction

## 1.1 History of boron nitride

### 1.1.1 Allotropes of boron nitride

Boron nitride (BN) is an inorganic compound consisting of boron (B) and nitrogen (N) atoms with a stoichiometric ratio of 1. BN has several crystal structures, such as hexagonal BN (h-BN), rhombohedral BN (r-BN), cubic BN (c-BN), and wurtzite BN (w-BN). Some of these structures are similar to those of carbon allotropes (e.g. hexagonal: graphite, cubic: diamond), because a B-N bond is isoelectronic with a C-C bond. For this similarity, $sp^2$ and $sp^3$-bonded BN structures can exist.

W. H. Balmain firstly synthesized boron nitride in 1842 by reacting $H_3BO_3$ and KCN.[1,2] This synthesized boron nitride had a layered structure with the hexagonal lattice of B and N (h-BN shown in Figure 1a). B and N atoms form $sp^2$ covalent bonds within a plane, while each layer is stacked with weak van der Waals (vdW) interaction. The stacking order of h-BN layer is AA' stacking in which the N atoms are located on top of B atoms of the adjacent layers. A different type of stacking order of boron nitride is a rhombohedral structure (r-BN), whose stacking order is expressed as ABC stacking (Figure 1b). These layered structures show lubricity due to weak inter-layer vdW interaction. For instance, h-BN have been used as a solid lubricant for a long time.[3] After the first h-BN synthesis reported by W. H. Balmain, many researchers started to study on synthesizing various BN compounds including h-BN due to the possibility of making carbon analogous structure (graphite).[4,5] The first synthesis of c-BN, diamond-like
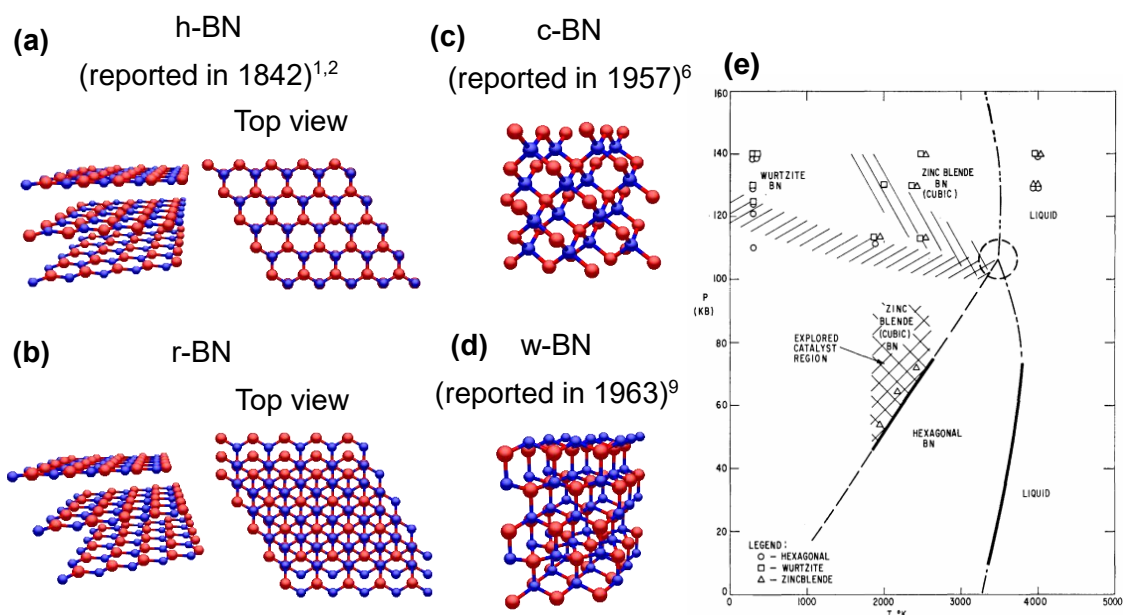
**Figure 1-1** Atomic models of various BN structures. (a) h-BN, (b) r-BN, (c) c-BN, (d) w-BN. (e) Pressure-temperature phase diagram with the equilibrium lines.[9]

structure by $sp^3$ covalent bods of B and N atoms, was reported by R. H. Wentorf in 1957.[6] The cubic BN structure was synthesized from h-BN by applying extremely high pressure and high temperature (HPHT, 1800 °C and 8.6 GPa), being similar to diamond synthesis from graphite.[7] Similar to diamond, c-BN is known as a hard material (second hardest material in the world) so that it is applicable to cutting tools for processing stiff materials.[8] In 1963, the existence of wurtzite type BN (w-BN) was reported by Bundy and Wentorf.[9] The synthesis of w-BN was also carried out under high pressure from h-BN, but this transformation occurred at much lower temperature (300 °C) than that used for c-BN synthesis. As shown in Figure 1-1e, the pressure-temperature phase diagram of boron nitride has several phase equilibrium lines, indicating the presence of different crystalline phases of boron nitride. These different BN structures have common excellent properties, such as high resistivity, thermal conductivity, and oxidation resistance. The physical properties of h-BN, c-BN, and w-BN are summarized in Table 1-1.[10–17] Reflecting many

**Table 1-1** Physical properties of three polymorphs of boron nitride. //c and ⊥c show the direction of parallel and normal to the c axis, respectively.

| | Density (g/cm³) | Band gap (eV) | Dielectric constant | Thermal conductivity (W/mK) | Young's modulus (TPa) | Oxidation temperature (˚C) |
|---|---|---|---|---|---|---|
| h-BN | 2.25 [16] | 5.5-6.0 [15] | 3.38(//c) [12] 6.61(⊥c) [12] | 400(⊥c) [15] | 0.81-1.3 [15] | 840 [15] |
| c-BN | 3.48 [17] | 6.3 [17] | 6.74 [12] | 1300 [17] | 0.79-9.0 [11] | 1200 [17] |
| w-BN | 3.45 [13] | 5.8 [10] | 6.99(//c) [12] 6.50(⊥c) [12] | — | 0.79-0.83 [11] | — |

attractive properties, industrial development of boron nitride has proceeded extensively, realizing many applications such as filler, crucible, lubricant, and catting tools.[4,5]

In the past two decades, the quality of boron nitride crystals has been significantly improved by employing highly purified solvent with extremely high temperature and pressure, mainly developed by Watanabe, Taniguchi, and Kanda.[18] This method allows to synthesize single crystalline c-BN and h-BN which show an intense exciton related cathodoluminescence (CL) peak at around 200 nm. This enabled to determine the intrinsic band gap experimentally. It had not been considered that h-BN shows intense luminescence due to the indirect band gap nature, but the result suggested a direct band gap nature in h-BN.[19] These reports stimulate further investigation of the band structure of h-BN[20–28], and finally it was concluded again that h-BN has an indirect band gap in spite of its strong photoluminescence.[20,29–31] Recently, application of h-BN to a substrate and/or a protection layer for two-dimensional (2D) materials as well as investigation of the optical properties of encapsulated 2D materials has been receiving increased interest, because the h-BN surface is atomically smooth and free of dangling bonds, which brings out the intrinsic properties of 2D materials[32]. This application of h-BN will be explained later in more details.

### 1.1.2   Allotropes of low-dimensional boron nitride

When material size becomes sufficiently small, typically 10 nm or less, the quantum confinement effect appears. This effect can be observed mainly by the change of the electronic and optical properties, which are deeply related to the electronic density of states (DOS), as shown in Figure 1-2a. For this, nanomaterials are fascinating objects for exploring new physical phenomena and also offer a possibility to create outstanding applications. In addition, surface area to volume ratio increases greatly with decreasing material size (Figure 1-2b), which is very useful for applications, such as catalyst, electrode for battery, and gas adsorbent. Carbon materials can form low-dimensional nanostructures, such as zero-dimensional (0D) fullerene, one-dimensional (1D) carbon nanotube, and 2D graphene. These kinds of low-dimensional structures of BN can be also observed, thanks to the similarity of a B-N bond to a C-C bond. These BN-based nanostructures have been actively studied, because the finding of new nanostructures is one of active fields in material science.[33]

The synthesis of 1D BN nanotube using an arc discharge method, similar to that used for the production of fullerene and carbon nanotube, was reported in 1995 by N. G. Chopra et al.[34] Like carbon nanotube, BN nanotube is composed of a h-BN sheet wrapped into a cylindrical tube (Figure 1-2c) and various chiralities can be formed, changing the band structure (also band gap).[35] In addition to BN nanotube, 1D BN nanostructures, such as nanowires, nanofibers, nanorods and nanoribbons, based on h-BN have been reported.[36–39] D. Golberg et al. reported the synthesis of 0D octahedral BN fullerene by electron beam irradiation to polygonal BN particles in 1998.[40] Afterwards, various works on theoretical and experimental studies have been widely performed to find different forms of BN fullerene.[41–46] The synthesis of 2D h-BN with monolayer

**(a)** Quantum confinement effect

**(b)** Increase of specific surface area

**(c)**

0D BN fullerene
(reported in 1998)[40]

1D BN nanotube
(reported in 1995)[34]

2D BN nanosheet
(reported in 1995)[47]
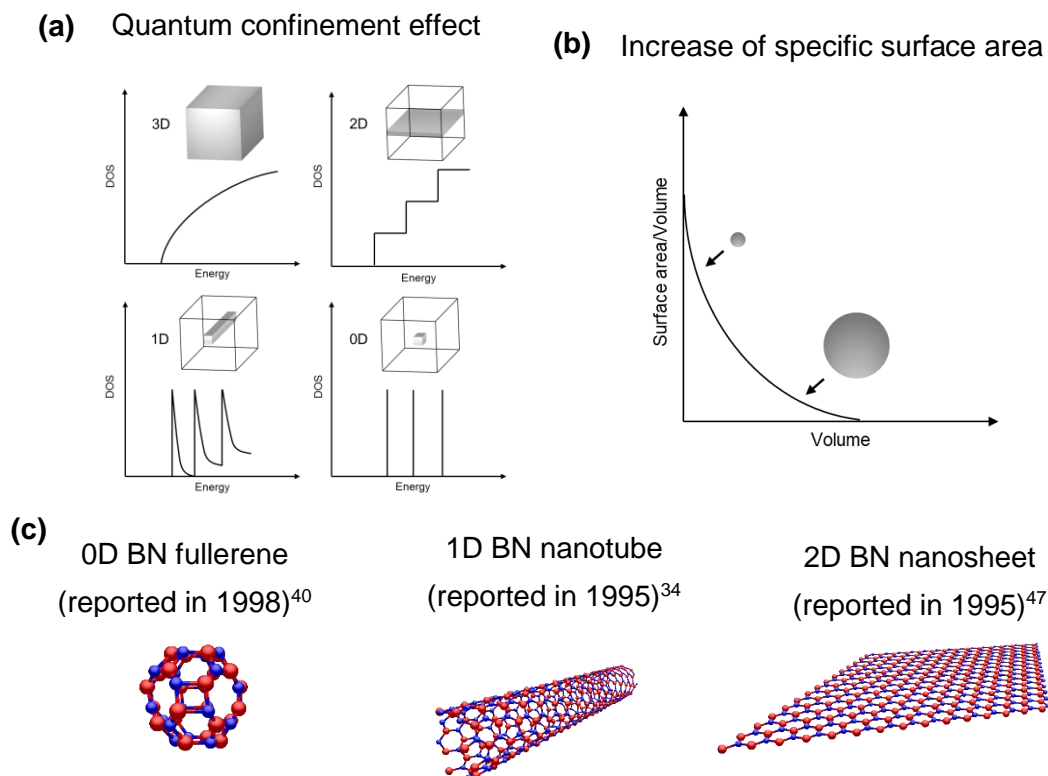
**Figure 1-2** (a) Electron density of states (DOS) for a bulk 3D, 2D structured, 1D structured, and 0D structured materials. (b) Surface to volume ratio of a nanoparticle plotted against the volume. (c) Atomic models of low-dimensional BN nanostructures.

thickness was reported by reacting borazine on metal surfaces, including Ni(111), Pd(111), and Pr(111) by A. Nagashima et al. in 1995.[47] Moreover, they investigated the electronic band structure of h-BN deposited on these metals by angle-resolved electron spectroscopy (ARPES) and found that h-BN is physisorbed on metal surfaces. As another 2D BN structure, nanomesh structure of BN was synthesized in 2004 by M. Corso.[48] Recently, research on 2D h-BN have been extensively performed in the world inspired by intensive reports on graphene and related 2D materials.

## 1.2 h-BN: an ideal dielectric sheet for 2D materials

### 1.2.1 Atomically thin 2D materials

About 100 years ago, R. E. Peierls, L. D. Landau, and N. D. Mermin theoretically predicted that atomically thin 2D crystal cannot exist due to its instability.[49–51] In spite of their theoretical prediction, thinnest 2D material, called graphene consisting of carbon honeycomb lattices with only one atom thickness, was experimentally prepared under ambient condition by K. S. Novoselov *et al.* in 2004.[52] The atomic model of graphene is described in Figure 1-3. Surprisingly, this graphene flake was obtained by a simple mechanical exfoliation from highly-oriented pyrolytic graphite (HOPG) using adhesive tape. Few-layer graphene showed an exceptionally high carrier mobility (~10,000 $cm^2/Vs$), which suggests such simple exfoliation method can produce high quality 2D materials (Figure 1-4a). Afterwards, they reported that monolayer graphene is a zero-gap semiconductor from the measured transport properties.[53] These results infer that the charge carriers in graphene behave as massless Dirac fermions which is expressed by the Dirac equation instead of Schrödinger equation that describes the electronic properties of most of the materials (Figure 1-4b).[53] The discovery of graphene and its quantum confinement effects attracted great interest in 2D system. At the early stage of the graphene research, peculiar physical properties of graphene, such as a massless charge carrier, high optical transparency, high mechanical flexibility, and high mechanical strength, were extensively studied.[54] These outstanding properties make graphene a promising candidate as main component in next generation devices.[55]

A few years later, scientists also paid attention to other 2D materials. Various layered materials were peeled off to form atomically-thin flakes, like graphene[56], leading to many important findings in 2D materials reported to date. Figure 1-3 shows atomic

Graphene
(carbon)

h-BN
(boron, nitrogen)

$MoS_2$
(Molybdenum, sulfur)

Phosphorene
(phosphorus)

**Common properties**

· Atomically thin thickness
and smooth surface

· Optical transparency

· Mechanical flexibility

· Quantum confinement effect

· High surface to volume ratio
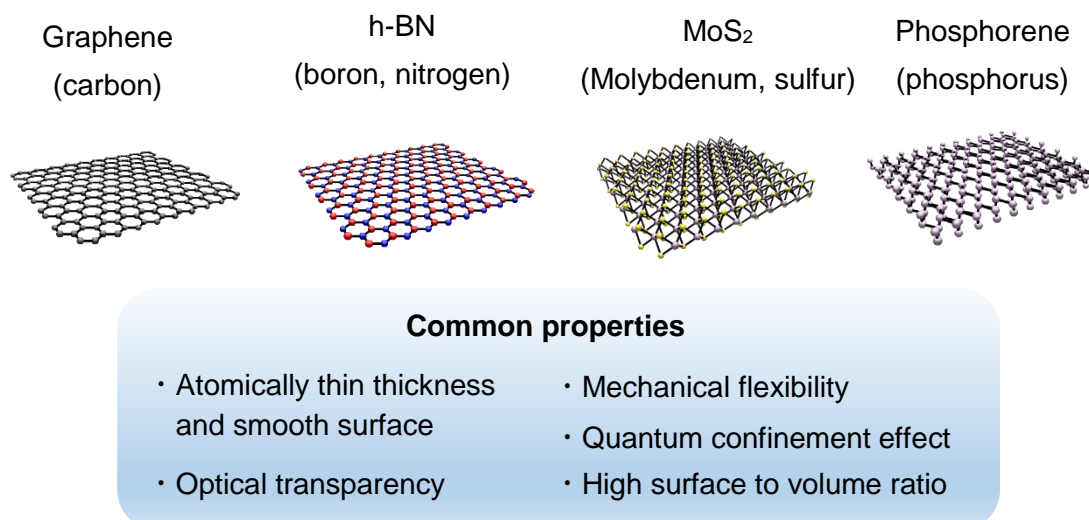
**Figure 1-3** Atomic structures of representative 2D materials and the common properties of these 2D materials.

**Table 1-2** List of various 2D materials (modified from ref.57)

| **Structures** | Graphene, h-BN, BCN | | **Buckled structure**: Phosphorene, Silicene, Germanene | |
|---|---|---|---|---|
| **2D chalcogenides** | **Semiconducting dichalcogenides**: $MoS_2$, $WS_2$, $MoSe_2$, $WSe_2$, etc. | **Semiconducting monochalcogenides**: GaSe, GaTe, InSe, SnS, etc. | | **Metallic dichalcogenides**: $NbSe_2$, $NbS_2$, $TiS_2$, $NiSe_2$, etc. |
| **2D oxides** | **Metal oxides**: Micas, Layered $CuO_x$, $MoO_3$, $WO_3$, etc | **Perovskite-type**: $LaNb_2O_7$, $(Ca,Sr)_2Nb_3O_{10}$, $Bi_4Ti_3O_{12}$, $Ca_2Ta_2TiO_{10}$, etc | | **Hydroxides**: $Ni(OH)_2$, $Eu(OH)_2$, etc |

structures of representative 2D materials. Table 1-2[57] lists a wide variety of 2D materials including metal oxide. Among them, 2D transition metal chalcogenides (TMCs) have been widely studied. In 2010, unique indirect to direct band gap transition was reported for molybdenum disulfide ($MoS_2$), a family of TMCs.[58,59] With decreasing the number of layers of $MoS_2$, the band structure of $MoS_2$ gradually changes and eventually it forms a direct band gap when it becomes monolayer. Thus, the monolayer $MoS_2$ shows strong exciton-related photoluminescence, while bilayer and multilayer $MoS_2$ do not show strong luminescence due to indirect gap nature (Figure 1-4c).[59] Because monolayer
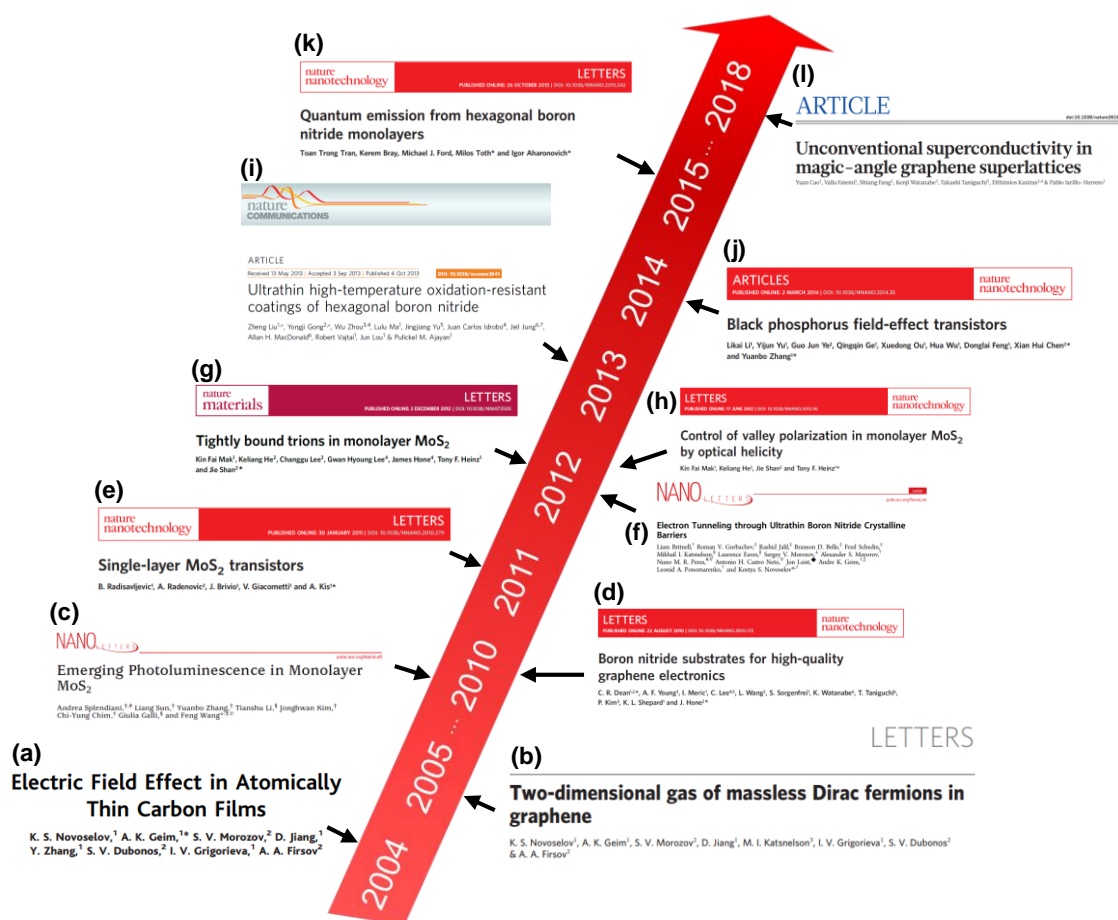
**Figure 1-4** Representative reports regarding **i**mportant findings of physical properties in 2D materials.

TMCs, such as $MoS_2$, tungsten disulfide ($WS_2$), and tungsten diselenide ($WSe_2$), are materials having the strong interaction of charges, tightly bound trions (binding energy is ~20 meV for $MoS_2$) and biexitons (binding energy is ~52 meV for $WSe_2$) were experimentally observed,[60,61] offering a new platform to explore many-body effects (Figure 1-4g). Moreover, due to the lack of inversion symmetry in odd numbers of layers of $MoS_2$, valley polarization was observed by optical pumping with circularly polarized light, which enables us to manipulate valley degree of freedom as an information carrier like charge carriers and spin polarized carriers (Figure 1-4h).[62–65] These experimental observations carve out new possibility that 2D TMCs are suitable for photonics, optoelectronics, and valleytronics.

Demands for electronic devices, such as low power consumption with high performance, device flexibility, and optical transparency, 2D materials have also attracted great attention.[66] For example, it was found that monolayer $MoS_2$ shows a high on/off ratio of ~$10^8$ with carrier mobility of ~217 $cm^2$/Vs in spite that the channel is only a few atom thickness (Figure 1-4e).[67] Therefore, 2D semiconductors have attracted a great interest from the expectation for future electronics, because it is likely that it can overcome the limitation of performance from the short channel effect, which is one of main issues in ultra-scale devices. In 2014, it was reported that the carrier mobility of phosphorene, mono or few-layer black phosphorus, is higher than that of TMCs, while having an enough band gap for switching of transistors (observed mobility was ~1,000 $cm^2$/Vs with an on/off ratio of ~$10^5$) (Figure 1-4j).[68]

2D superconductivity has been widely studied for a long time, because of its wealth of quantum phenomena.[69] Recent progress of synthesis of various 2D materials made the 2D superconductivity a hot topic again. In 2015, superconductivity in monolayer $NbSe_2$ produced by mechanical exfoliation was observed.[70,71] Moreover, it was found that this 2D $NbSe_2$ shows enhanced charge-density-wave (CDW) due to enhanced electron-phonon interactions. To modulate superconducting transition temperature ($T_c$) in 2D system, electro-static doping via ion gating using ionic liquid was found to be an excellent approach. For instance, ZrNCl and $MoS_2$ measured at different gate voltages showed increased $T_c$.[72,73] Very recently, inspired by the theoretical prediction,[74] superconducting behavior were observed in twisted bilayer graphene with a specific stacking angle, which is called a magic angle (in spite of the conductive nature of graphene),[75] which was realized by precise angle-controlled transfer technique.[76–78] This is because under the magic angle strongly correlated electrons due to the flat band make

superconducting state that can be induced by applied gate voltage. This report stimulates tremendous recent interest in moiré superlattices using 2D materials (Figure 1-4l).[79–90]

In 2017, magnetic order in 2D materials was found by two research groups.[91,92] Cheng Gong et al. discovered ferromagnetism in $Cr_2Ge_2Te_6$ atomic layers.[91] In contrast to bulk materials, it was found that transition temperature from paramagnetic and ferromagnetic states in $Cr_2Ge_2Te_6$ atomic layers can be controlled by small magnetic field (smaller than 0.3 tesla). Huang et al. demonstrated ferromagnetism in $CrI_3$ with even monolayer thickness.[92] However, these magnetisms were observed at cryogenic temperatures. More recently, M. Bonilla et al. reported that monolayer $VSe_2$ deposited on graphite and $MoS_2$ substrates by MBE method shows ferromagnetism at room temperature.[93] Thanks to the discovery of these 2D magnets, it is expected that further efforts on studying 2D magnetic materials provide new kinds of devices, such as 2D spin valves and single-photon sources with electric polarization control.[94]

2D h-BN is an attractive material as a tunnel barrier layer for charge carriers and spin-polarized electrons due to its large band gap, atomically flat surface, atom-level thickness uniformity, and controllable thickness. Several fundamental studies regarding electron tunneling through h-BN layers suggested that it has great potential for tunneling devices,[95,96] which stimulates various studies on devices utilizing tunneling effect through 2D h-BN (Figure 1-4f).[97–101] Moreover, chemical inertness and impermeable in-plane structure of h-BN make it a fascinating material as a passivation layer. For example, several studies reported that 2D h-BN prevents certain 2D materials from oxidation even when monolayer h-BN was used (Figure 1-4i).[102,103] Also, the application of h-BN to passivation barriers for ions was demonstrated in several fields, such as biology, electronics, and optoelectronics.[104–107] Recently, it is also proposed that h-BN is a

promising material for 2D quantum light emitter (Figure 1-4k),[108] ultrabright , photostable, and room temperature quantum emitter like diamond partly due to a wide band gap (~6 eV) and clear structure.[109] For this, there are several promising applications based on quantum emission from h-BN including quantum computing, quantum sensing, and platform to explore basic quantum phenomena.[108] More importantly, the application which attracts the most attention nowadays is utilization as a dielectric layer to bring out intrinsic physical properties of other 2D materials, such as graphene and TMCs (Figure 1-4d).[110] Detailed explanation related to this point will be described in the next section.

## 1.2.2   h-BN-based van der Waals (vdW) heterostructures

As mentioned in the 1.2.1 section, Most of 2D materials can exist under ambient condition. However, due to atomic thickness and high surface area, 2D materials are highly sensitive to their environment, including changes in temperature, humidity, adsorbates, and charged impurities, which hinders the observation of intrinsic physical properties of 2D materials. This is because most or even all of the atoms of 2D materials locate on the surface of other materials, unlike bulk materials. An example of this inherent sensitivity of 2D materials is illustrated in Figure 1-5 (graphene and its heterostructures with h-BN). Carrier mobility in graphene/$SiO_2$ is usually limited by the surface roughness, charged impurities, dangling bonds, and optical phonons of the underlying $SiO_2$ surface (most of substrate materials have similar surfaces interacting with 2D materials).[111–116] In addition, the electronic properties of graphene is affected by physisorption of molecules.[117] In certain cases, this phenomenon can be advantageous when 2D materials are used as gas sensor. However, the properties of the 2D materials are generally degraded by physisorbed oxygen and water

**Graphene/SiO$_2$**　　　　**Graphene/h-BN/SiO$_2$**　　　**h-BN/Graphene/h-BN/SiO$_2$**



$\mu$(RT): 17,000 cm$^2$/Vs [118]　　$\mu$(RT): 60,000 cm$^2$/Vs [110]

$\mu$(RT): 140,000 cm$^2$/Vs [119]

(theoretical limitation: 200,000 cm$^2$/Vs)

**Bottom h-BN**　　　**Top h-BN**

Limited carrier mobility mainly due to scattering effect by SiO$_2$ surface

Realization of clean interface and screening of long range interaction from SiO$_2$ surface

Realization of clean interface on top side and protection from adsorbates

**SiO$_2$ surface**

· Slightly rough
· Charged impurities
· dangling bonds
· Highly polarized optical phonons

**h-BN surface**

· Atomically smooth
· Dangling bond-free
· Lowly polarized optical phonons
· Impermeable in-plane structure

**Figure 1-5** Carrier mobilities of graphene transistors combined with multilayer h-BN layers. $\mu$ is measured carrier mobility of graphene.[133-135]

when exposed to ambient. Therefore, it is essential to eliminate the influences suffered from the environment in 2D materials.

To solve these issues, h-BN is expected to be an ideal dielectric substrate and protection layer for 2D materials. This is because the h-BN surface is atomically smooth and free from dangling bonds, and h-BN can be stacked with other 2D materials via weak van der Waals (vdW) interaction, which is generally called as vdW heterostructue. Actually, the introduction of h-BN to the interface between a 2D material and substrate surface significantly improves the physical properties of the 2D materials. For example, the carrier mobility of graphene can be increased from 17,000 cm$^2$/Vs to 60,000 cm$^2$/Vs, by simply introducing multilayer h-BN between a graphene channel and SiO$_2$ surface (Figure 1-5).[110,118] This mobility can be further increased to 140,000 cm$^2$/Vs, which is

close to the theoretical limit value, by encapsulating the graphene channel with h-BN using the improved transfer process.[119]

The carrier mobility of TMCs was also increased by h-BN, reaching 1,000-34,000 cm$^2$/Vs at low temperatures.[120] Furthermore, optical properties of TMCs can be substantially improved by growing WS$_2$ on h-BN instead of SiO$_2$ surface.[121] The photoluminescence (PL) of WS$_2$ becomes much stronger and sharper (full width at half maximum (FWHM) is 26 meV) on h-BN, as compared with that grown on SiO$_2$ substrate surface (61 meV).[121] Such drastic improvement by h-BN is accounted for by the reduction of the influences (charged impurities, polar optical phonons, and relatively rough surface) from the underlying substrates (e.g. SiO$_2$/Si substrate). As another important aspect, 2D materials encapsulated by h-BN becomes stable because of the gas barrier property of h-BN. Actually, it was demonstrated that black phosphorous, very easy to be oxidized in air, can be stabilized by covering with h-BN.[122] Due to such large contribution, h-BN is now widely used in both fundamental study and applications of 2D materials. Therefore, h-BN is a highly desirable dielectric layer for applications to various 2D materials.

## 1.3　Purpose of the research

Since the first report on the significant increase of the graphene's carrier mobility by h-BN, fundamental studies on the h-BN-based vdW heterostructures have been extensively performed in the world. Most of the studies have used mechanically exfoliated h-BN flakes. Although the exfoliated h-BN flakes have high crystalline quality, h-BN flake size is small and its thickness is not uniform on a substrate. Now h-BN is an essential material in the field of 2D materials. Therefore, development of the scalable and low cost fabrication of vdW heterostructure using h-BN is highly required for practical

**Studies in this thesis**

**Previous studies**

Growth of h-BN on polycrystalline metal foils[103,124–135]
⇒Random h-BN orientation

**Chapter 4**

Large-area epitaxial growth of h-BN using Cu(111) film

**Chapter 5**

Growth of uniform multilayer h-BN using Ni-Fe film

Growth of multilayer h-BN on polycrystalline Fe foils[136,137]
⇒Non-uniform h-BN thickness

Significant enhancement of optical properties of WS$_2$ using CVD multilayer h-BN

**Figure 1-6** Novel points and achievement in this thesis

applications. Different types of h-BN production methods have been reported.[32] For instance, liquid-phase exfoliation is a good candidate for producing large amount of h-BN flakes suitable for wet processes to make large-area h-BN sheets.[123] However, the quality of flakes is low and also the realization of good connection between flakes is difficult, preventing the application to 2D substrate. Bottom up approach has a great potential to make high quality h-BN with controllable shape, stacking order, and thickness in large-scale. In particular, chemical vapor deposition (CVD) method employing catalytic

substrate is expected to meet above requirements so that many researchers have studied the synthesis of h-BN by CVD method. However, in spite of the significant efforts, the controlled synthesis of h-BN has not achieved so far. For realizing the synthesis of high-quality h-BN by CVD method, metal catalyst becomes very important. For example, the selection of metals with suitable crystal structure, melting point, and solubilities of B and N is important to control h-BN growth. Moreover, structural morphologies of metals, such as density of grain boundaries and crystal planes, are also important factors. In previous literatures, polycrystalline meal foils have been mainly used, but these foils produced randomly oriented h-BN grains.[103,124–135] Also, uniform growth of multilayer h-BN is still a challenging issue, because highly controlled B, N dissolution and segregation processes are required.[136,137] In this thesis, CVD growth and mechanisms of monolayer, epitaxially aligned h-BN on Cu(111) film and uniform multilayer h-BN on Ni-Fe alloy film are extensively investigated.

## 1.4   Outline of this thesis

This thesis consists of two main parts, (1) epitaxial CVD growth of monolayer h-BN on Cu(111) film and (2) uniform growth of multilayer h-BN on Ni-Fe alloy film and its growth mechanism. Prior to the experimental results and discussion regarding these main parts, I would like to describe research trends in 2D materials to show how this research field has advanced in Chapter 2. After that, several properties of h-BN and details of preparation methods, especially CVD method, are described in Chapter 3. Chapter 4 and 5 demonstrate epitaxial growth of monolayer h-BN on Cu(111) film in large-scale and growth of uniform multilayer h-BN on Ni-Fe alloy film, respectively. Finally, I conclude this thesis and describe future outlook in Chapter 6.

# References

1. Balmain, W. H. Observations on the formation of compounds of boron and silicon with nitrogen and certain metals. *Philos. Mag. J. Series 3,* **21**, 270–277 (1842).

2. Balmain, W. H. Bemerkungen über die bildung von verbindungen des bors und siliciums mit stickstoff und gewissen metallen. *J. Prakt. Chem.* **27**, 422–430 (1842).

3. Watanabe, S., Miyake, S. and Murakawa, M. Tribological properties of cubic, amorphous and hexagonal boron nitride films. *Surf. Coat. Technol.* **49**, 406–410 (1991).

4. Vel, L., Demazeau, G. and Etourneau, J. Cubic boron nitride: synthesis, physicochemical properties and applications. *Mater. Sci. Eng. B* **10**, 149–164 (1991).

5. Lipp, A., Schwetz, K. A. and Hunold, K. Hexagonal boron nitride: Fabrication, properties and applications. *J. Eur. Ceram. Soc.* **5**, 3–9 (1989).

6. Wentorf, R. H. Cubic form of boron nitride. *J. Chem. Phys.* **26**, 956–956 (1957).

7. Bundy, F. P., Hall, H. T., Strong, H. M. and Jun, R. H. W. Man-made diamonds. *Nature* **176**, 51–55 (1955).

8. Murakawa, M. Surface coatings of super hard materials for tool applications. *Mater. Sci. Forum* **246**, 1-28 (1997).

9. Bundy, F. P. and Wentorf, R. H. Direct transformation of hexagonal boron nitride to denser forms. *J. Chem. Phys.* **38**, 1144–1149 (1963).

10. Xu, Y.-N. and Ching, W. Y. Calculation of ground-state and optical properties of boron nitrides in the hexagonal, cubic, and wurtzite structures. *Phys. Rev. B* **44**, 7787–7798 (1991).

11. Edgar, J. H., Smith, D. T., Eddy, C. R., Carosella, C. A. and Sartwell, B. D. c-Boron–aluminum nitride alloys prepared by ion-beam assisted deposition. *Thin Solid Films* **298**, 33–38 (1997).

12. Ohba, N., Miwa, K., Nagasako, N. and Fukumoto, A. First-principles study on

structural, dielectric, and dynamical properties for three BN polytypes. *Phys. Rev. B* **63**, 115207 (2001).

13. Soma, T., Sawaoka, A. and Saito, S. Characterization of wurtzite type boron nitride synthesized by shock compression. *Mat. Res. Bull.* **9**, 755-762 (1974).

14. Li, L. H., Cervenka, J., Watanabe, K., Taniguchi, T. and Chen, Y. Strong oxidation resistance of atomically thin boron nitride nanosheets. *ACS Nano* **8**, 1457–1462 (2014).

15. Xiang-Fen Jiang, Q. W. and Xiang-Fen Jiang, Q. W. Recent progress on fabrications and applications of boron nitride nanomaterials: A review. *J. Mater. Sci. Technol.* **31**, 589–598 (2015).

16. Chen, L. *et al.* Thermal conductivity performance of polypropylene composites filled with polydopamine-functionalized hexagonal boron nitride. *PLOS ONE* **12**, e0170523 (2017).

17. Narayan, J., Bhaumik, A., Gupta, S., Haque, A. and Sachan, R. Progress in Q-carbon and related materials with extraordinary properties. *Mater. Res. Lett.* **6**, 353–364 (2018).

18. Watanabe, K., Taniguchi, T. and Kanda, H. Ultraviolet luminescence spectra of boron nitride single crystals grown under high pressure and high temperature. *Phys. Status Solidi A* **201**, 2561–2565 (2004).

19. Watanabe, K., Taniguchi, T. and Kanda, H. Direct-bandgap properties and evidence for ultraviolet lasing of hexagonal boron nitride single crystal. *Nat. Mater.* **3**, 404–409 (2004).

20. Arnaud, B., Lebègue, S., Rabiller, P. and Alouani, M. Huge excitonic effects in layered hexagonal boron nitride. *Phys. Rev. Lett.* **96**, 026402 (2006).

21. Wirtz, L., Marini, A. and Rubio, A. Excitons in boron nitride nanotubes: dimensionality effects. *Phys. Rev. Lett.* **96**, 126104 (2006).

22. Giovannetti, G., Khomyakov, P. A., Brocks, G., Kelly, P. J. and van den Brink, J. Substrate-induced band gap in graphene on hexagonal boron nitride: ab initio density functional calculations. *Phys. Rev. B* **76**, 073103 (2007).

23. Kubota, Y., Watanabe, K., Tsuda, O. and Taniguchi, T. Deep ultraviolet light-emitting hexagonal boron nitride synthesized at atmospheric pressure. *Science* **317**, 932–934 (2007).

24. Evans, D. A. *et al.* Determination of the optical band-gap energy of cubic and hexagonal boron nitride using luminescence excitation spectroscopy. *J. Phys.: Condens. Matter* **20**, 075233 (2008).

25. Park, C.-H. and Louie, S. G. Energy gaps and stark effect in boron nitride nanoribbons. *Nano Lett.* **8**, 2200–2203 (2008).

26. Gao, R. *et al.* High-yield synthesis of boron nitride nanosheets with strong ultraviolet cathodoluminescence emission. *J. Phys. Chem. C* **113**, 15160–15165 (2009).

27. Watanabe, K., Taniguchi, T., Niiyama, T., Miya, K. and Taniguchi, M. Far-ultraviolet plane-emission handheld device based on hexagonal boron nitride. *Nat. Photonics* **3**, 591–594 (2009).

28. Yu, J. *et al.* Vertically aligned boron nitride nanosheets: chemical vapor synthesis, ultraviolet light emission, and superhydrophobicity. *ACS Nano* **4**, 414–422 (2010).

29. Watanabe, K. and Taniguchi, T. Jahn-Teller effect on exciton states in hexagonal boron nitride single crystal. *Phys. Rev. B* **79**, 193104 (2009).

30. Gao, S.-P. Crystal structures and band gap characters of h-BN polytypes predicted by the dispersion corrected DFT and GW method. *Solid State Commun.* **152**, 1817–1820 (2012).

31. Cassabois, G., Valvin, P. and Gil, B. Hexagonal boron nitride is an indirect bandgap semiconductor. *Nat. Photonics* **10**, 262–266 (2016).

32. Zhang, K., Feng, Y., Wang, F., Yang, Z. and Wang, J. Two dimensional hexagonal

boron nitride (2D-hBN): synthesis, properties and applications. *J. Mater. Chem. C* **5**, 11992–12022 (2017).

33. Pakdel, A., Bando, Y. and Golberg, D. Nano boron nitride flatland. *Chem. Soc. Rev.* **43**, 934–959 (2014).

34. Chopra, N. G. *et al.* Boron nitride nanotubes. *Science* **269**, 966–967 (1995).

35. Golberg, D. *et al.* Boron nitride nanotubes and nanosheets. *ACS Nano* **4**, 2979–2993 (2010).

36. Chen, Y. J., Zhang, H. Z. and Chen, Y. Pure boron nitride nanowires produced from boron triiodide. *Nanotechnology* **17**, 786 (2006).

37. Zhang, H., Yu, J., Chen, Y. and Gerald, J. F. Conical boron nitride nanorods synthesized via the ball-milling and annealing method. *J. Amer. Ceram. Soc.* **89**, 675–679 (2006).

38. Chen, Z.-G. *et al.* Novel boron nitride hollow nanoribbons. *ACS Nano* **2**, 2183–2191 (2008).

39. Qiu, Y. *et al.* Synthesis of continuous boron nitride nanofibers by solution coating electrospun template fibers. *Nanotechnology* **20**, 345603 (2009).

40. Golberg, D., Bando, Y., Stéphan, O. and Kurashima, K. Octahedral boron nitride fullerenes formed by electron beam irradiation. *Appl. Phys. Lett.* **73**, 2441–2443 (1998).

41. Alexandre, S. S., Mazzoni, M. S. C. and Chacham, H. Stability, geometry, and electronic structure of the boron nitride $B_{36}N_{36}$ fullerene. *Appl. Phys. Lett.* **75**, 61–63 (1999).

42. Pokropivny, V. V. *et al.* Boron nitride analogs of fullerenes (the fulborenes), nanotubes, and fullerites (the fulborenites). *J. Solid State Chem.* **154**, 214–222 (2000).

43. Oku, T., Kuno, M., Kitahara, H. and Narita, I. Formation, atomic structures and properties of boron nitride and carbon nanocage fullerene materials. *Int. J. Inorg.*

*Mater.* **3**, 597–612 (2001).

44. Oku, T., Nishiwaki, A., Narita, I. and Gonda, M. Formation and structure of $B_{24}N_{24}$ clusters. *Chem. Phys. Lett.* **380**, 620–623 (2003).

45. Oku, T., Nishiwaki, A. and Narita, I. Formation and atomic structure of $B_{12}N_{12}$ nanocage clusters studied by mass spectrometry and cluster calculation. *Sci. Technol. Adv. Mater.* **5**, 635–638 (2004).

46. Monajjemi, M. and Boggs, J. E. A new generation of $B_nN_n$ rings as a supplement to boron nitride tubes and cages. *J. Phys. Chem. A* **117**, 1670–1684 (2013).

47. Nagashima, A., Tejima, N., Gamou, Y., Kawai, T. and Oshima, C. Electronic structure of monolayer hexagonal boron nitride physisorbed on metal surfaces. *Phys. Rev. Lett.* **75**, 3918–3921 (1995).

48. Corso, M. *et al.* Boron nitride nanomesh. *Science* **303**, 217–220 (2004).

49. Peierls, R. E. *Helv. Phys. Acta* **7**, 81 (1923).

50. Landau, L. D. Zur theorie der phasenumwandlungen II. *Phys. Z. Sowjet.* **11**, 26-35 (1937).

51. Mermin, N. D. Crystalline order in two dimensions. *Phys. Rev.* **176**, 250–254 (1968).

52. Novoselov, K. S. *et al.* Electric field effect in atomically thin carbon films. *Science* **306**, 666–669 (2004).

53. Novoselov, K. S. *et al.* Two-dimensional gas of massless Dirac fermions in graphene. *Nature* **438**, 197–200 (2005).

54. Geim, A. K. and Novoselov, K. S. The rise of graphene. *Nat. Mater.* **6**, 183–191 (2007).

55. Schwierz, F. Graphene transistors. *Nat. Nanotechnol.* **5**, 487–496 (2010).

56. Novoselov, K. S. *et al.* Two-dimensional atomic crystals. *Proc. Natl. Acad. Sci. U.S.A.* **102**, 10451–10453 (2005).

57. Geim, A. K. and Grigorieva, I. V. Van der Waals heterostructures. *Nature* **499**, 419–425 (2013).

58. Mak, K. F., Lee, C., Hone, J., Shan, J. and Heinz, T. F. Atomically thin $MoS_2$: a new direct-gap semiconductor. *Phys. Rev. Lett.* **105**, 136805 (2010).

59. Splendiani, A. *et al.* Emerging photoluminescence in monolayer $MoS_2$. *Nano Lett.* **10**, 1271–1275 (2010).

60. Mak, K. F. *et al.* Tightly bound trions in monolayer $MoS_2$. *Nat. Mater.* **12**, 207–211 (2013).

61. You, Y. *et al.* Observation of biexcitons in monolayer $WSe_2$. *Nat. Phys.* **11**, 477–481 (2015).

62. Cao, T. *et al.* Valley-selective circular dichroism of monolayer molybdenum disulphide. *Nat. Commun.* **3**, 887 (2012).

63. Mak, K. F., He, K., Shan, J. and Heinz, T. F. Control of valley polarization in monolayer $MoS_2$ by optical helicity. *Nat. Nanotechnol.* **7**, 494–498 (2012).

64. Zeng, H., Dai, J., Yao, W., Xiao, D. and Cui, X. Valley polarization in $MoS_2$ monolayers by optical pumping. *Nat. Nanotechnol.* **7**, 490–493 (2012).

65. Suzuki, R. *et al.* Valley-dependent spin polarization in bulk $MoS_2$ with broken inversion symmetry. *Nat. Nanotechnol.* **9**, 611–617 (2014).

66. Fiori, G. *et al.* Electronics based on two-dimensional materials. *Nat. Nanotechnol.* **9**, 768–779 (2014).

67. Radisavljevic, B., Radenovic, A., Brivio, J., Giacometti, V. and Kis, A. Single-layer $MoS_2$ transistors. *Nat. Nanotechnol.* **6**, 147–150 (2011).

68. Li, L. *et al.* Black phosphorus field-effect transistors. *Nat. Nanotechnol.* **9**, 372–377 (2014).

69. Saito, Y., Nojima, T. and Iwasa, Y. Highly crystalline 2D superconductors. *Nat. Rev. Mater.* **2**, 16094 (2017).

70. Cao, Y. *et al.* Quality heterostructures from two-dimensional crystals unstable in air by their assembly in inert atmosphere. *Nano Lett.* **15**, 4914–4921 (2015).

71. Xi, X. *et al.* Strongly enhanced charge-density-wave order in monolayer NbSe$_2$. *Nat. Nanotechnol.* **10**, 765–769 (2015).

72. Ye, J. T. *et al.* Liquid-gated interface superconductivity on an atomically flat film. *Nat. Mater.* **9**, 125–128 (2010).

73. Ye, J. T. *et al.* Superconducting dome in a gate-tuned band insulator. *Science* **338**, 1193–1196 (2012).

74. Bistritzer, R. and MacDonald, A. H. Moire bands in twisted double-layer graphene. *Proc. Natl. Acad. Sci. U.S.A.* **108**, 12233–12237 (2011).

75. Cao, Y. *et al.* Unconventional superconductivity in magic-angle graphene superlattices. *Nature* **556**, 43–50 (2018).

76. Cao, Y. *et al.* Superlattice-induced insulating states and valley-protected orbits in twisted bilayer graphene. *Phys. Rev. Lett.* **117**, 116804 (2016).

77. Kim, K. *et al.* van der Waals heterostructures with high accuracy rotational alignment. *Nano Lett.* **16**, 1989–1995 (2016).

78. Kim, K. *et al.* Tunable moiré bands and strong correlations in small-twist-angle bilayer graphene. *Proc. Natl. Acad. Sci. U.S.A.* **114**, 3364–3369 (2017).

79. Dodaro, J. F., Kivelson, S. A., Schattner, Y., Sun, X. Q. and Wang, C. Phases of a phenomenological model of twisted bilayer graphene. *Phys. Rev. B* **98**, 075154 (2018).

80. Efimkin, D. K. and MacDonald, A. H. Helical network model for twisted bilayer graphene. *Phys. Rev. B* **98**, 035404 (2018).

81. Fidrysiak, M., Zegrodnik, M. and Spałek, J. Unconventional topological superconductivity and phase diagram for an effective two-orbital model as applied to twisted bilayer graphene. *Phys. Rev. B* **98**, 085436 (2018).

82. Guo, H., Zhu, X., Feng, S. and Scalettar, R. T. Pairing symmetry of interacting fermions on a twisted bilayer graphene superlattice. *Phys. Rev. B* **97**, 235453 (2018).

83. Kang, J. and Vafek, O. Symmetry, maximally localized wannier states, and a low-

energy model for twisted bilayer graphene narrow bands. *Phys. Rev. X* **8**, 031088 (2018).

84. Koshino, M. *et al.* Maximally localized wannier orbitals and the extended hubbard model for twisted bilayer graphene. *Phys. Rev. X* **8**, 031087 (2018).

85. Ochi, M., Koshino, M. and Kuroki, K. Possible correlated insulating states in magic-angle twisted bilayer graphene under strongly competing interactions. *Phys. Rev. B* **98**, 081102 (2018).

86. Ribeiro-Palau, R. *et al.* Twistable electronics with dynamically rotatable heterostructures. *Science* **361**, 690–693 (2018).

87. Thomson, A., Chatterjee, S., Sachdev, S. and Scheurer, M. S. Triangular antiferromagnetism on the honeycomb lattice of twisted bilayer graphene. *Phys. Rev. B* **98**, 075109 (2018).

88. Xu, C. and Balents, L. Topological superconductivity in twisted multilayer graphene. *Phys. Rev. Lett.* **121**, 087001 (2018).

89. Yuan, N. F. Q. and Fu, L. Model for the metal-insulator transition in graphene superlattices and beyond. *Phys. Rev. B* **98**, 045103 (2018).

90. Zou, L., Po, H. C., Vishwanath, A. and Senthil, T. Band structure of twisted bilayer graphene: Emergent symmetries, commensurate approximants, and Wannier obstructions. *Phys. Rev. B* **98**, 085435 (2018).

91. Gong, C. *et al.* Discovery of intrinsic ferromagnetism in two-dimensional van der Waals crystals. *Nature* **546**, 265–269 (2017).

92. Huang, B. *et al.* Layer-dependent ferromagnetism in a van der Waals crystal down to the monolayer limit. *Nature* **546**, 270–273 (2017).

93. Bonilla, M. *et al.* Strong room-temperature ferromagnetism in $VSe_2$ monolayers on van der Waals substrates. *Nat. Nanotechnol.* **13**, 289 (2018).

94. 2D magnetism gets hot. *Nat. Nanotechnol.* **13**, 269 (2018).

95. Lee, G.-H. *et al.* Electron tunneling through atomically flat and ultrathin hexagonal boron nitride. *Appl. Phys. Lett.* **99**, 243114 (2011).

96. Britnell, L. *et al.* Electron tunneling through ultrathin boron nitride crystalline barriers. *Nano Lett.* **12**, 1707–1710 (2012).

97. Britnell, L. *et al.* Field-effect tunneling transistor based on vertical graphene heterostructures. *Science* **335**, 947–950 (2012).

98. Kamalakar, M. V., Dankert, A., Bergsten, J., Ive, T. and Dash, S. P. Enhanced tunnel spin injection into graphene using chemical vapor deposited hexagonal boron nitride. *Sci. Rep.* **4**, 6146 (2014).

99. Vu, Q. A. *et al.* Two-terminal floating-gate memory with van der Waals heterostructures for ultrahigh on/off ratio. *Nat. Commun.* **7**, 12725 (2016).

100. Wang, J. *et al.* High mobility $MoS_2$ transistor with low schottky barrier contact by using atomic thick h-BN as a tunneling layer. *Adv. Mater.* **28**, 8302–8308 (2016).

101. Piquemal-Banci, M. *et al.* 2D-MTJs: introducing 2D materials in magnetic tunnel junctions. *J. Phys. D: Appl. Phys.* **50**, 203002 (2017).

102. Liu, Z. *et al.* Ultrathin high-temperature oxidation-resistant coatings of hexagonal boron nitride. *Nat. Commun.* **4**, 2541 (2013).

103. Sinha, S., Takabayashi, Y., Shinohara, H. and Kitaura, R. Simple fabrication of air-stable black phosphorus heterostructures with large-area hBN sheets grown by chemical vapor deposition method. *2D Mater.* **3**, 035010 (2016).

104. Parra, C. *et al.* Suppressing bacterial interaction with copper surfaces through graphene and hexagonal-boron nitride coatings. *ACS Appl. Mater. Interfaces* **7**, 6430–6437 (2015).

105. Ergen, O., Gilbert, S. M., Turner, S. J. and Zettl, A. Hexagonal boron nitride as a cationic diffusion barrier to form a graded band gap perovskite heterostructure. *Phys. Status Solidi B* **253**, 2478–2480 (2016).

106. Lo, C.-L. *et al.* Studies of two-dimensional h-BN and MoS$_2$ for potential diffusion barrier application in copper interconnect technology. *npj 2D Mater. and Appl.* **1**, 42 (2017).

107. Chilkoor, G. *et al.* Hexagonal boron nitride: the thinnest insulating barrier to microbial corrosion. *ACS Nano* **12**, 2242–2252 (2018).

108. Aharonovich, I. and Toth, M. Quantum emitters in two dimensions. *Science* **358**, 170–171 (2017).

109. Aharonovich, I. *et al.* Diamond-based single-photon emitters. *Rep. Prog. Phys.* **74**, 076501 (2011).

110. Dean, C. R. *et al.* Boron nitride substrates for high-quality graphene electronics. *Nat. Nanotechnol.* **5**, 722–726 (2010).

111. Hwang, E. H., Adam, S. and Sarma, S. D. Carrier transport in two-dimensional graphene layers. *Phys. Rev. Lett.* **98**, 186806 (2007).

112. Ishigami, M., Chen, J. H., Cullen, W. G., Fuhrer, M. S. and Williams, E. D. Atomic structure of graphene on SiO$_2$. *Nano Lett.* **7**, 1643–1648 (2007).

113. Chen, J.-H., Jang, C., Xiao, S., Ishigami, M. and Fuhrer, M. S. Intrinsic and extrinsic performance limits of graphene devices on SiO$_2$. *Nat. Nanotechnol.* **3**, 206–209 (2008).

114. Fratini, S. and Guinea, F. Substrate-limited electron dynamics in graphene. *Phys. Rev. B* **77**, 195415 (2008).

115. Katsnelson, M. I. and Geim, A. K. Electron scattering on microscopic corrugations in graphene. *Phil. Trans. R. Soc. A* **366**, 195–204 (2008).

116. Morozov, S. V. *et al.* Giant intrinsic carrier mobilities in graphene and its bilayer. *Phys. Rev. Lett.* **100**, 016602 (2008).

117. Wehling, T. O. *et al.* Molecular doping of graphene. *Nano Lett.* **8**, 173–177 (2008).

118. Hong, X., Zou, K. and Zhu, J. Quantum scattering time and its implications on scattering sources in graphene. *Phys. Rev. B* **80**, 241415 (2009).

119. Wang, L. *et al.* One-dimensional electrical contact to a two-dimensional material. *Science* **342**, 614–617 (2013).

120. Cui, X. *et al.* Multi-terminal transport measurements of $MoS_2$ using a van der Waals heterostructure device platform. *Nat. Nanotechnol.* **10**, 534–540 (2015).

121. Okada, M. *et al.* Direct chemical vapor deposition growth of $WS_2$ atomic layers on hexagonal boron nitride. *ACS Nano* **8**, 8273–8277 (2014).

122. Doganov, R. A. *et al.* Transport properties of pristine few-layer black phosphorus by van der Waals passivation in an inert atmosphere. *Nat. Commun.* **6**, 6647 (2015).

123. Nicolosi, V., Chhowalla, M., Kanatzidis, M. G., Strano, M. S. and Coleman, J. N. Liquid Exfoliation of Layered Materials. *Science* **340**, 1226419 (2013).

124. Song, L. *et al.* Large scale growth and characterization of atomic hexagonal boron nitride layers. *Nano Lett.* **10**, 3209–3215 (2010).

125. Kim, K. K. *et al.* Synthesis of monolayer hexagonal boron nitride on Cu foil using chemical vapor deposition. *Nano Lett.* **12**, 161–166 (2012).

126. Guo, N. *et al.* Controllable growth of triangular hexagonal boron nitride domains on copper foils by an improved low-pressure chemical vapor deposition method. *Nanotechnology* **23**, 415605 (2012).

127. Iqbal, M. W., Iqbal, M. Z., Jin, X., Eom, J. and Hwang, C. Superior characteristics of graphene field effect transistor enclosed by chemical-vapor-deposition-grown hexagonal boron nitride. *J. Mater. Chem. C* **2**, 7776–7784 (2014).

128. Tay, R. Y. *et al.* Growth of large single-crystalline two-dimensional boron nitride hexagons on electropolished copper. *Nano Lett.* **14**, 839–846 (2014).

129. Khan, M. H. *et al.* Synthesis of large and few atomic layers of hexagonal boron nitride on melted copper. *Sci. Rep.* **5**, 7743 (2015).

130. Wu, Q. *et al.* Single crystalline film of hexagonal boron nitride atomic monolayer by controlling nucleation seeds and domains. *Sci. Rep.* **5**, 16159 (2015).

131. Lee, Y.-H. *et al.* Growth selectivity of hexagonal-boron nitride layers on Ni with various crystal orientations. *RSC Adv.* **2**, 111–115 (2011).

132. Ismach, A. *et al.* Toward the controlled synthesis of hexagonal boron nitride films. *ACS Nano* **6**, 6378–6385 (2012).

133. Cho, H. *et al.* Growth kinetics of white graphene (h-BN) on a planarised Ni foil surface. *Sci. Rep.* **5**, 11985 (2015).

134. Caneva, S. *et al.* Nucleation control for large, single crystalline domains of monolayer hexagonal boron nitride via Si-doped Fe catalysts. *Nano Lett.* **15**, 1867–1875 (2015).

135. Kim, G. *et al.* Growth of high-crystalline, single-layer hexagonal boron nitride on recyclable platinum foil. *Nano Lett.* **13**, 1834–1839 (2013).

136. Kim, S. M. *et al.* Synthesis of large-area multilayer hexagonal boron nitride for high material performance. *Nat. Commun.* **6**, 8662 (2015).

137. Caneva, S. *et al.* Controlling catalyst bulk reservoir effects for monolayer hexagonal boron nitride CVD. *Nano Lett.* **16**, 1250–1261 (2016).

# Chapter 2

# Research trend in 2D materials

## 2.1   Why do 2D materials attract researchers attention?

Over the past several decades, nanoscience has become one of main scientific research fields because of unique properties obtained by nanomaterials, such as nanoparticles, nanotubes, and nanowires. As mentioned in Chapter 1, nanomaterials have low-dimensional structures (0D, 1D, and 2D). In 1959, R. P. Feynman proposed that nanoscale materials will show many interesting physical phenomena at the annual meeting of the American Physical Society.[1] A few years later, K. Ryogo predicted that nanoparticle, representative of 0D nanomaterials, can exhibit physical properties peculiar in nanostructure (Kubo effect).[2] These predictions were spread across the scientists, and many related works have been performed to date.[3–7] For instance, K. Shunichi *et al.* demonstrated that Cu nanoparticles have finite spacing of the electron energy levels originated from the size effect.[8] Also, nanowires and nanosheets, representative 1D and 2D nanomaterials, respectively, have shown unique properties originating in the quantum confinement effect and specific band structures related to low dimensionality. For these unique properties, low-dimensional nanomaterials have tremendous attention, because they offer an excellent platform to explore new phenomena and also applicable to various potential applications.

Carbon nanomaterials, known as fullerene (0D), carbon nanotube (1D), and graphene (2D), opened up the new research of ultimately low-dimensional materials.[9–12] For example, the diameters of fullerene and carbon nanotube with certain chiralities are

less than 1 nm. Notably, the thickness of graphene is only one carbon atom thick (0.345 nm), which is the thinnest material in the world. In particular, the discovery of carbon nanotubes in 1991 by S. Iijima triggered the nanotechnology research.

Since the first preparation of graphene in 2004,[13] various kinds of 2D structured materials with a few atoms thick have attracted great attention, because high quality flakes are easily obtained by mechanical exfoliation, which enable us to experimentally explore new phenomena originated from low dimensionality.[14] Recently, not only the studies on fundamental phenomena, but also the researches on industrial applications have been increasing, and several big projects related to 2D materials started in many countries.[15]

In this Chapter, research and development trends in the field of 2D materials are discussed to indicate the current situation of this active field. The trend in 2D materials research was investigated based on the number of scientific papers and patents. In addition, active communities working with 2D materials were investigated. The above studies were performed utilizing Scopus and Patent Scope. In the counting patents number using Patent Scope, only the patents belonging to Patent Cooperation Treaty (PCT) was regarded as international patents.

## 2.2　Development of 2D materials research field

Figure 2-1 shows trend of scientific publication and patent summarized during 2004-2017. Although there are numerous number of reported 2D materials, only graphene, transition metal chalcogenides (TMCs), and h-BN have been selected, because these are major 2D materials which occupy large portion of publications and patents. As can be seen in Figure 2-1a,b, both publications and patents have dramatically increased
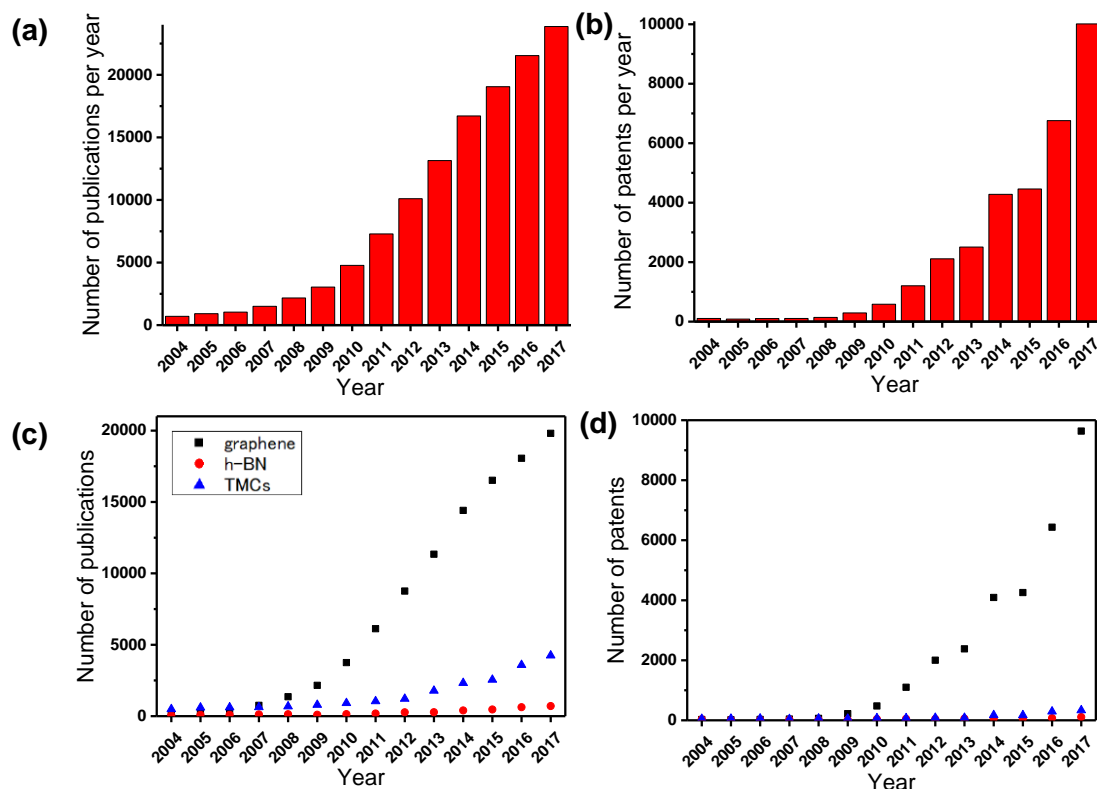
**Figure 2-1** The number of publication (a) and patents (b) of 2D materials research. (c,d) The trend of graphene, h-BN, and TMCs publications and patents.

since the first report of graphene in 2004. In particular, the numbers of publications and patents have risen significantly around 2010 where this is the year that two graphene researchers, Geim and Novoselov, were awarded the Nobel Prize in Physics. Therefore, it can be seen from Figure 2-1a,b that this prize further stimulated attraction to 2D materials research. Figure 2-1c,d indicates the number of publications and patents categorized with 2D materials. Although graphene-related publications occupy more than 50%, the number of publication related to TMCs and h-BN have increased from 2013 (see Figure 2-1c). The increased interest in these materials can be attributed to several important findings related to TMCs and h-BN.[16,17] The reports on an indirect to direct band gap transition and transistor operation observed in monolayer TMCs triggered the TMC research.[16,18] For h-BN research, significant enhancement of carrier

mobility of graphene by using h-BN as a dielectric substrate was a noticeable achievement. These findings triggered the exponential increase of publications and patents handling TMCs and h-BN.

## 2.3   Research activities categorized by countries

### 2.3.1   Scientific papers

Figure 2-2a shows share distributions of scientific papers published in 2004, 2010, and 2017 in the field of 2D materials research. In 2004, USA published the largest number of papers, which occupied about one-quarter of the all publications (22 %), followed by Japan (14 %) and China (10 %). However, in 2004, the most of publications reported graphene-related works and other 2D materials, such as TMCs and h-BN are very few. In 2010 when A. K. Geim and K. S. Novoselov won Nobel Prize in Physics for the first report of graphene, publications from China has rapidly increased and exceeded that from Japan as compared with the share in 2004. Moreover, China became the country that publishes the largest number of scientific papers with almost one third of the all publications in 2017. This significant increase implies that China is intensively investing in the field of 2D materials research. Furthermore, South Korea, Singapore, Spain, and Iran are newly ranked in top 10 during 2010-2017. This also suggests that these countries started to pay a lot of attention to this research field. On the other hand, the shares of USA, Japan, Germany, France, and Italy have gradually declined. Figure 2-2b shows the annual trend of publication share. Significant increase of publications in China from 2008 to 2013 is clearly seen in this graph, while the decrease of the USA is also apparent. It is noted that the share of China exceeds that of USA in 2011. The above
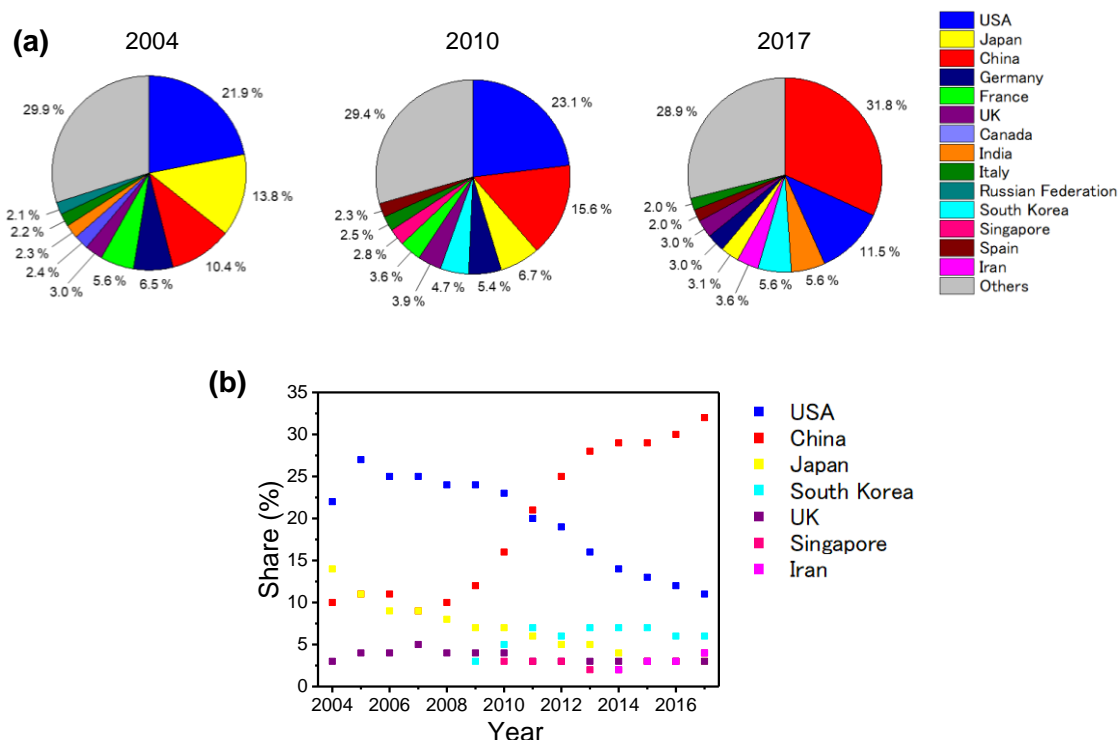
**Figure 2-2** (a) Pie chart for publication trend in 2D materials research by country. (b) Annual trend of share rate by country.
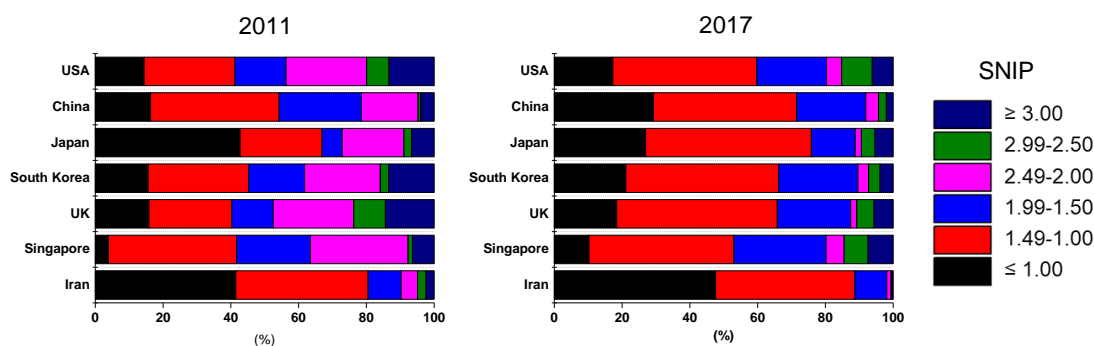


**Figure 2-3** Bar graphs to compare journal level published from representing countries in 2011 and 2017.

analysis is based only on the number of publications. To study the quality of each publication, I investigated the levels of journals in which papers were published. For classifying the journal level, "Source Normalized Impact per Paper (SNIP)" was used as an index of the journal level. SNIP is defined as follows: Raw Impact per Paper Published in the Journal (RIP) divided by the Relative Database Citation Potential (RDCP).

Because SNIP is defined to consider the difference in frequency of quotation by field, this factor allows us to fairly compare scientific papers in different fields.[19] Figure 2-3 shows bar graphs that compare the journal level published from different countries (which published relatively many scientific papers) in 2011 and 2017. In 2011, South Korea and UK are the top 2 countries that have a high ratio of publications with the SNIP higher than 3.0 (SNIP 3.0 includes prestigious scientific journals, such as Nature and Science). On the other hand, China and Iran ranked 6th and 7th in producing such high level of publications. Although the number of publications was relatively high in Japan and Iran in 2011, these countries have a high ratio of publications SNIP lower than 1.0.

During 2011-2017, a ratio of high SNIP journals decreases on the whole, suggesting that the impact of research of 2D materials on scientific community has slightly declined as compared with the early stage of graphene research. Starting a number of new journals handling 2D materials can be another reason for this. In 2017, the top two countries produced a high ratio of publications with SNIP higher than 3.0 were the USA and Singapore, and the bottom two countries with high journal level (SNIP >3.0) were China and Iran. Moreover, China and Iran also have a high ratio of publications with SNIP less than 1.0, as compared to other countries in 2017. Therefore, many of those papers in these countries do not have high impact, although China and Iran recently produced a large number of scientific papers.

## 2.3.2 Patents

Figure 2-4a shows share distributions of patents of 2D materials categorized by country in 2004, 2010, and 2017. In 2017, China and the USA occupied large share in the number of patents. Especially, it is seen that China has been producing huge

**(a)**



**(b)**
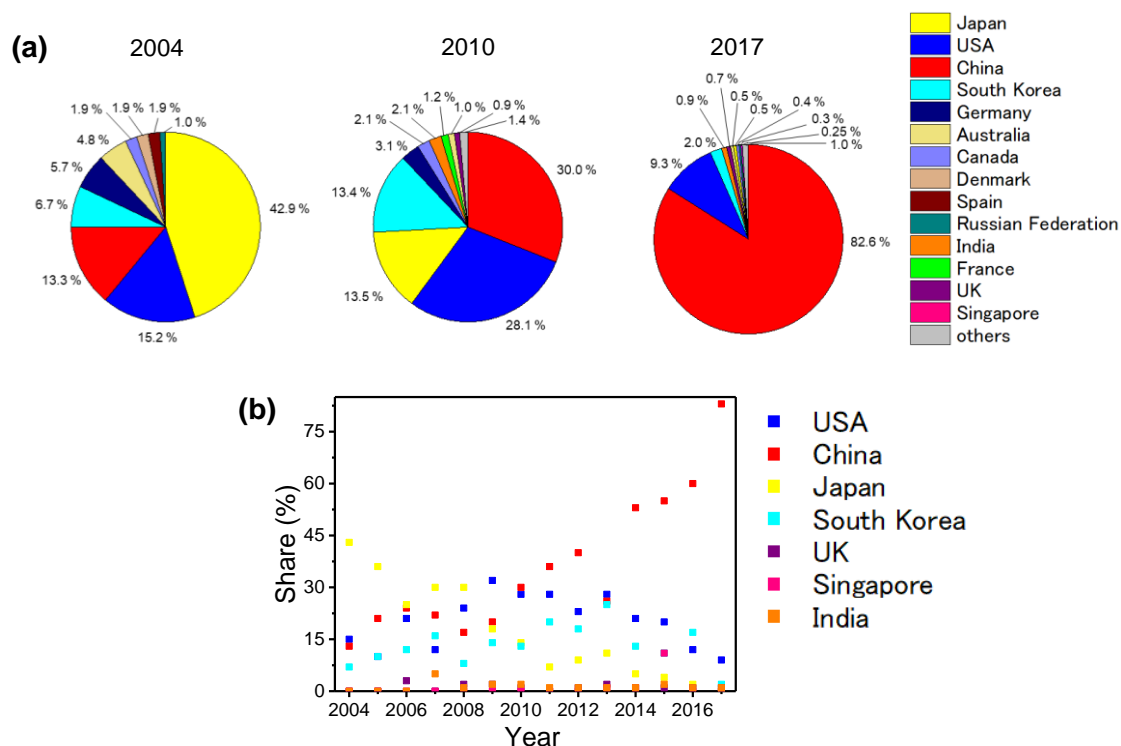


**Figure 2-4** (a) Pie charts showing the patent trend in 2D materials research. (b) Annual trend of country share.
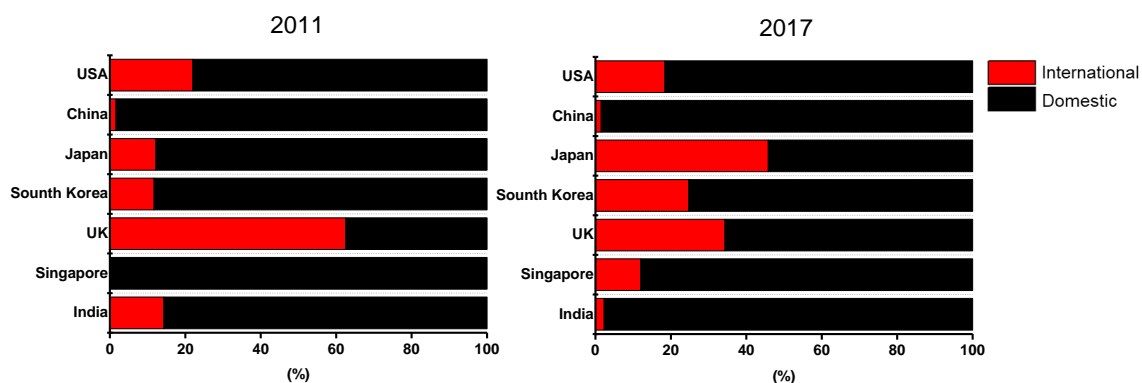


**Figure 2-5** Bar graphs that compares the ratios of international and domestic patents produced from representing countries in 2011 and 2017.

numbers of patents. Surprisingly, China accounts for a share of 84 % in 2017, which means that most of the patents are originated from China. Being different from the trend of the scientific papers, South Korea often ranked in top three patent holder. It is likely that groups in South Korea tends to concentrate on practical products using 2D materials.

As can be seen in Figure 2-4b, share of patents in China has been rapidly increasing. Moreover, during 2008-2017, the number of patents has increased steeply. From 2004-2011, the shares in the USA and South Korea had been gradually increased. Afterwards, the share has gradually decreased due to the steep increase of the number of patents from China.

To investigate the quality of patents issued from each country, I examined the ratio of international to domestic patents in major countries. Figure 2-5 shows bar graphs of the relative ratios of international and domestic patents in 2011 and 2017. Although China dominates in the number of patents in 2D materials, most of these patents are categorized to domestic in both 2011 and 2017. This trend suggests that patents in China may not have a high impact on a global development regarding 2D materials. The ratios of international patent issued from Singapore in 2011 and India in 2017 are relatively low. On the other hand, UK in both 2011 and 2017, Japan in 2017, and South Korea have relatively high ratios of international patents.

## 2.4   Active communities in 2D materials research

As shown in Figures 2-3 and 2-5, although the relative ratios of high-level papers and international patents are not high in China, the numbers of scientific papers and patents from China are dominant in the field of 2D materials research. Therefore, it can be regarded that the presence of China in this field is strong. In this section, I collected and organized the numbers of publications and patents produced from individual institutes to understand the active institutes that show strong presence in 2D materials research.

Figure 2-6 shows the top 7 institutes that published scientific papers and patents

related to 2D materials during 2004-2017. Regarding scientific papers, the institutes in China dominate this ranking. In particular, Chinese Academy of Science (CAS), which is a network of different institutes in China, has the largest share. This institute is the largest scientific organization, including around 60,000 researchers and receives the highest rating for research activity (Weighted fractional count (WFC): 1510.38).[20] While the CAS dominates the number of publications, two Singaporean institutes and one French institute ranked in the top 7 publishers. As mentioned before, Singapore is a country that tends to produce papers with a high level (Figure 2-3). Therefore, it seems that Nanyang Technological University (NTU) and National University of Singapore (NUS) contribute the production of highly rated papers. In the patent ranking, South Korea has a strong presence thanks to the high activities of Samsung Electronics Co., Ltd. (Samsung) and Korea Advanced Institute of Science & Technology (KAIST). These two organizations have submitted large quantities of patents. In particular, Samsung concentrates on 2D materials based electronics and batteries, because this company has various electronic productions. IBM has also intensively studied 2D materials-based electronics, resulting in the 4th institute for having a number of patents. China also has a strong presence in patent ranking as well. In particular, a number of patents regarding graphene-based optoelectronics occupies a high percentage.

**(a)**
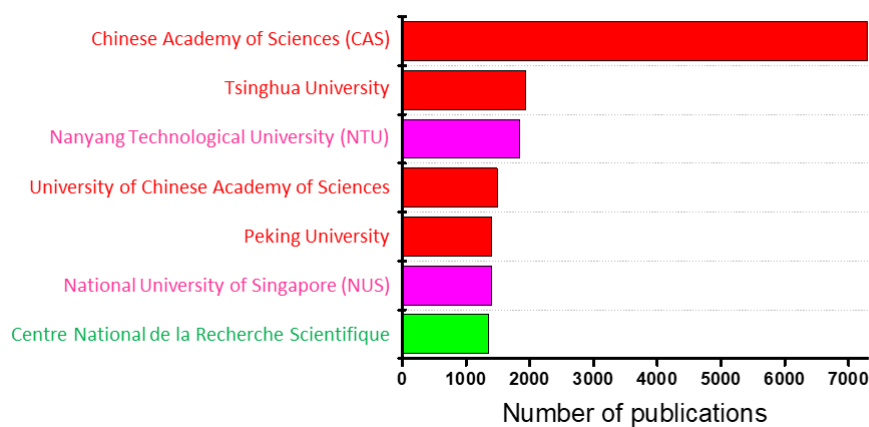


**(b)**
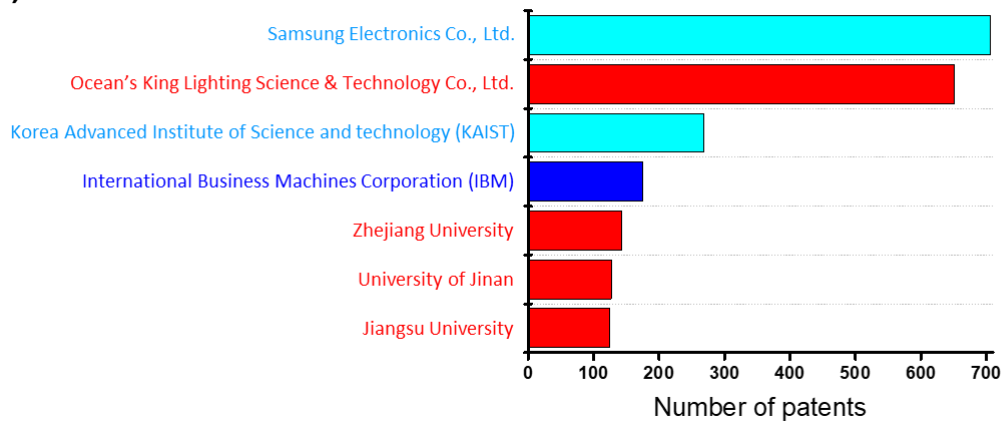


**Figure 2-6** Top 7 institutes that published scientific papers (a) and patents (b) during 2004-2017. Red, pink, yellow green, light blue, and blue correspond to institutes in China, Singapore, France, South Korea, and USA, respectively.

# References

1. Feynman, R. P. There's plenty of room at the bottom. *Resonance* **16**, 890 (2011).

2. Kubo, R. Electronic properties of metallic fine particles. I. *J. Phys. Soc. Jpn.* **17**, 975–986 (1962).

3. Morokhov, I. D., Petinov, V. I., Trusov, L. I. and Petrunin, V. F. Structure and properties of fine metallic particles. *Sov. Phys. Usp.* **24**, 295-317 (1981).

4. Wood, D. M. and Ashcroft, N. W. Quantum size effects in the optical properties of

small metallic particles. *Phys. Rev. B* **25**, 6255–6274 (1982).

5. Klier, K. Structure and function of real catalysts. *Appl. Surf. Sci.* **19**, 267–297 (1984).

6. Jefferson, D. A. *et al.* Atomic structure of ultrafine catalyst particles resolved with a 200-keV transmission electron microscope. *Nature* **323**, 428–431 (1986).

7. Rancourt, D. G. and Scorzelli, R. B. Low-spin $\gamma$-Fe-Ni($\gamma_{LS}$) proposed as a new mineral in Fe-Ni-bearing meteorites: epitaxial intergrowth of $\gamma_{LS}$ and tetrataenite as a possible equilibrium state at ~20–40 at% Ni. *J. Magn. Magn. Mater.* **150**, 30–36 (1995).

8. Kobayashi, S., Takahashi, T. and Sasaki, W. Size effect of metallic fine particle of Cu. *J. Phys. Soc. Jpn.* **32**, 1234–1236 (1972).

9. Baughman, R. H., Zakhidov, A. A. and Heer, W. A. de. Carbon nanotubes--the route toward applications. *Science* **297**, 787–792 (2002).

10. Rao, C. N. R., Biswas, K., Subrahmanyam, K. S. and Govindaraj, A. Graphene, the new nanocarbon. *J. Mater. Chem.* **19**, 2457–2469 (2009).

11. Mochalin, V. N., Shenderova, O., Ho, D. and Gogotsi, Y. The properties and applications of nanodiamonds. *Nat. Nanotechnol.* **7**, 11–23 (2012).

12. Acquah, S. F. A. *et al.* Review—the beautiful molecule: 30 years of $C_{60}$ and its derivatives. *ECS J. Solid State Sci. Technol.* **6**, M3155–M3162 (2017).

13. Novoselov, K. S. *et al.* Electric field effect in atomically thin carbon films. *Science* **306**, 666–669 (2004).

14. Das, S., Robinson, J. A., Dubey, M., Terrones, H. and Terrones, M. Beyond graphene: progress in novel two-dimensional materials and van der Waals solids. *Annu. Rev. Mater. Res.* **45**, 1–27 (2015).

15. Peplow, M. Graphene booms in factories but lacks a killer app. *Nat. News* **522**, 268 (2015).

16. Splendiani, A. *et al.* Emerging photoluminescence in monolayer $MoS_2$. *Nano Lett.* **10**, 1271–1275 (2010).

17. Dean, C. R. *et al.* Boron nitride substrates for high-quality graphene electronics. *Nat. Nanotechnol.* **5**, 722–726 (2010).

18. Radisavljevic, B., Radenovic, A., Brivio, J., Giacometti, V. and Kis, A. Single-layer MoS$_2$ transistors. *Nat. Nanotechnol.* **6**, 147–150 (2011).

19. Measuring a journals impact. Available at: https://www.elsevier.com/authors/journal-authors/measuring-a-journals-impact.

20. 2018 Annual Tables: Ten institutions that dominated science. Available at: https://www.natureindex.com/news-blog/twenty-eighteen-annual-tables-ten-institutions-that-dominated-sciences.

# Chapter 3

# Properties and preparation methods of h-BN

## 3.1   Structures and properties of h-BN

### 3.1.1   Structures

h-BN has several stacking orders such as AA', A'B, and AB', as shown in Figure 3-1b.[1] Among them, AA' stacking is the most energetically favorable structure (Figure 3-1c), because B and N atoms are slightly positively and negatively charged, respectively, due to their different electronegativities, which gives the alternating order of B and N atoms in the stacking direction (positively charged B atoms locate on negatively charged N atoms, and *vice versa*). This can be seen in Figure 3-1c which compares the energies of different stacking orders calculated by different calculation methods including solid state and surface system (PBEsol) with basis set superposition errors (BSSEs) (blue square), local second-order Møller-Plesset perturbation (LMP2) theory without BSSEs (black down-pointing triangle), LMP2 with BSSEs (red up-pointing triangle), and hartree-fock (HF) theory with BSSEs (green circle). The space group of this AA' stacking is P63/mmc with a unit cell shown in Figure 3-1a.
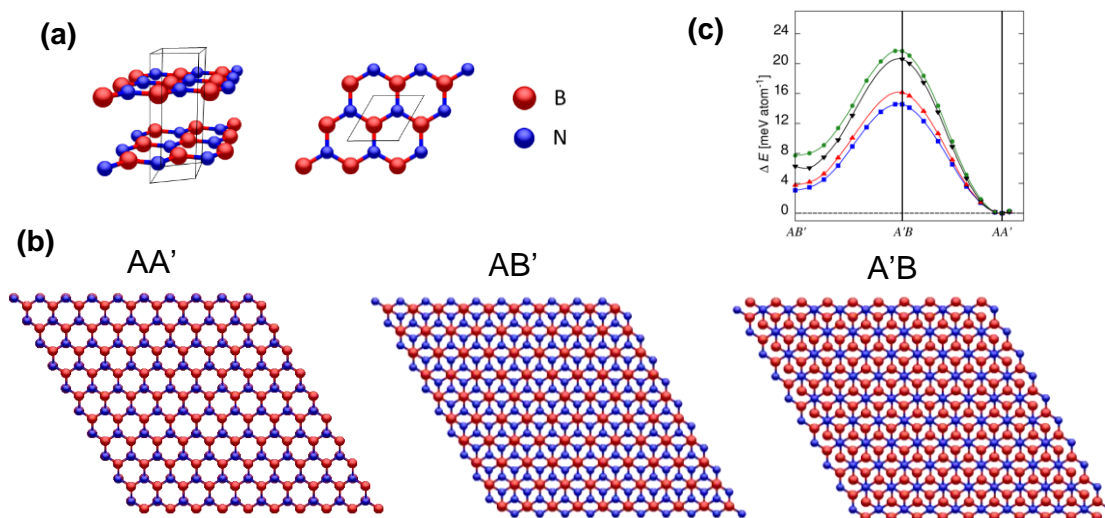
**Figure 3-1** (a) Atomic models of AA' stacked h-BN. (b) Atomic models of 3 types of stacking order of h-BN. (c) Stacking energies of h-BN calculated by solid state and surface system (PBEsol) with basis set superposition errors (BSSEs) (blue square), local second-order Møller-Plesset perturbation (LMP2) theory without BSSEs (black down-pointing triangle), LMP2 with BSSEs (red up-pointing triangle), and hartree-fock (HF) theory with BSSEs (green circle).[1]

### 3.1.2　Lattice vibrations

Bulk, AA' stacked h-BN has several vibration modes, such as $A_{2u}$, $B_{1g}$, $E_{1u}$, and $E_{2g}$ (Figure 3-2a).[2] Some of these modes are Raman or Infrared (IR) active. When vibration causes a change in polarizability, it is Raman active, while it becomes IR active when the vibration induces a change in dipole moment.　The $A_{2u}$ and $E_{1u}$ modes shown in Figure 3-2(a) are IR active. The $E_{1g}$ mode is Raman active, but the $B_{1g}$ mode is inactive both for Raman and IR.

Raman spectroscopy has been widely used to identify a crystalline phase of BN and also to evaluate their crystal quality. Figure 3-2b compares the Raman spectra of one to three layers of h-BN and bulk h-BN.[3] The Raman peak originated from the $E_{2g}$ mode

reflects quality of h-BN, such as crystallinity (line width), thickness (intensity and peak position shift), strain (peak shift), and doping level (peak shift).
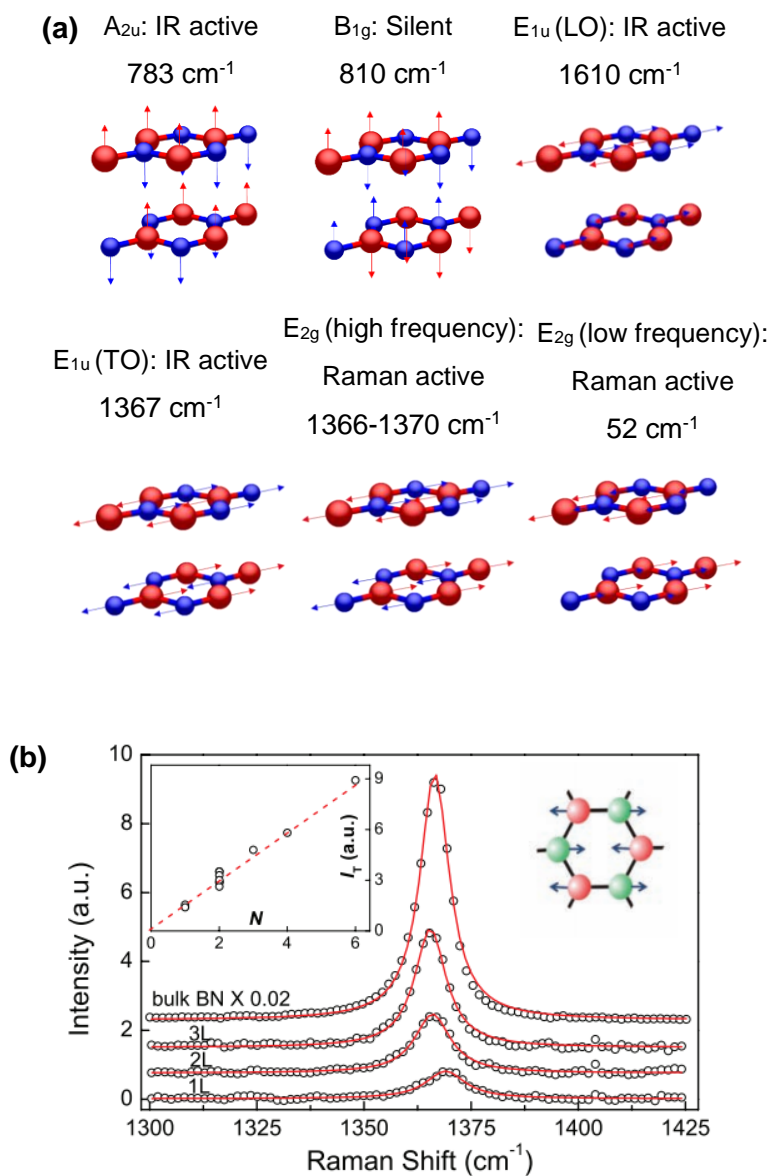


**Figure 3-2** (a) Different vibration modes of h-BN. Frequencies are taken from ref. 2 (b) Raman spectra from exfoliated h-BN flakes with the different number of layers and bulk h-BN. Inset of (b) is a change in integrated intensity of the $E_{2g}$ peak plotted against the number of layers.[3]

### 3.1.3 Electronic band structure

h-BN is an insulating material with a wide band gap, unlike graphene in spite of the similarity of their structures, because $\pi$-electrons in h-BN localize on N atoms originated from a large difference in electronegativities of B and N atoms. The band structure of AA' bulk h-BN is shown in Figure 3-3a calculated by GW ab initio method.[4] The h-BN has an indirect band gap of 5.80 eV (GW ab initio calculation.[4] The conduction band (CB) minimum and valence band (VB) maximum correspond to $\Gamma$ and near-K points, respectively.[4] Interestingly, according to theoretical calculation (GW ab initio calculation), monolayer h-BN shows a direct band gap of 7.25 eV at K point, as shown in Figure 3-3b.[5] Although optical properties of relatively thin h-BN (6 layers) was studied recently,[6] there is still no experimental report that proves such direct band gap nature expected in monolayer h-BN.
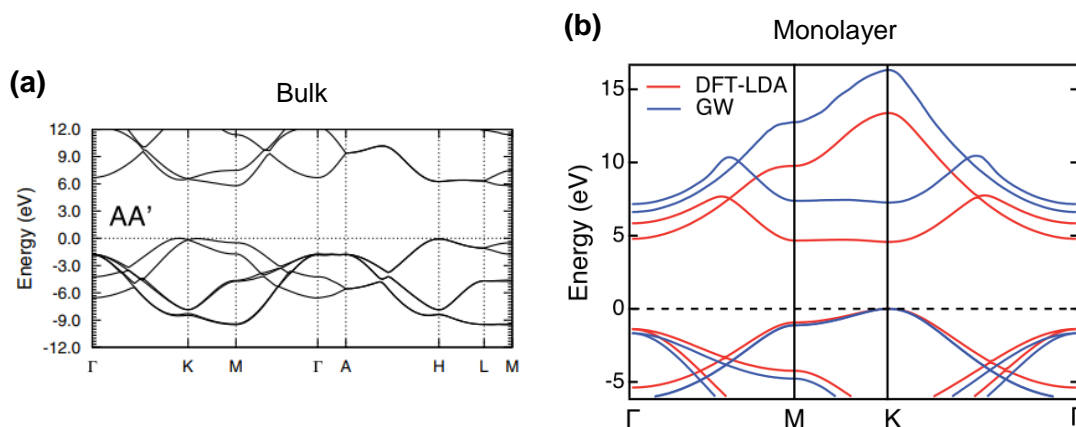


**Figure 3-3** Band structures of bulk (AA' stacking) (a) and monolayer h-BN (b).[4,5] In (b), both the density functional theory-local density approximation (DFT-LDA) and GW approximation results are shown.

### 3.1.4　Dielectric properties

Theoretical calculation indicates that bulk h-BN has different dielectric constants for in-plane (6.93) and out-of-plane (3.76).[7] Interestingly, the out-of-plane dielectric constant also depends on the h-BN thickness (see Table 3-1)[7] The anisotropic dielectric properties of h-BN was also studied experimentally, and in-plane and out-of-plane dielectric constants were investigated by measuring dielectric break down.　The obtained values are comparable to those obtained by the theoretical calculations (Figure 3-4a).[8] Also, it was pointed out that this large difference can be attributed to anisotropic band gaps of bulk h-BN. For example, the band gap of (out-of-plane) c-axis direction is ~5.9 eV, while that of in-plane is ~10.6 eV. Furthermore, as h-BN is a layered material, the behavior of dielectric breakdown is different from that of conventional insulators. The breakdown behavior was studied by using single crystal h-BN, and it was observed that the breakdown gradually proceeds as compared with other insulating materials, such as $SiO_2$ (see Figure 3-4c).　This is because the breakdown process a layer-by-layer manner in the case of bulk h-BN, as illustrated in Figure 3-4b,c).[9] Tunneling barrier height for electrons has also been investigated by some groups. According to one of these studies, for 1-3 layers of h-BN, a direct tunneling current flows in the out-of-plane direction when a low-bias voltage is applied vertically (Figure 3-4d).[10] In the case of thicker h-BN with more than 4 layers, the tunneling current can be explained by a Fowler-Nordheim tunneling model for relatively high applying bias voltages. The barrier height for electron tunneling and the dielectric breakdown strength were estimated to be 3.03 (± 0.3) eV and 7.94 MV/cm, respectively.

| Number of layers | ε(//c) | ε(⊥c) |
|---|---|---|
| 1 | 6.82 | 3.29 |
| 2 | 6.86 | 3.44 |
| 3 | 6.86 | 3.52 |
| 4 | 6.86 | 3.58 |
| 5 | 6.86 | 3.62 |
| bulk | 6.93 | 3.76 |

**Table 3-1** In-plane and out-of-plane dielectric constants of h-BN with the different number of layers. //c and ⊥c show parallel and normal to the c-axis, respectively. (modified from ref. 7)
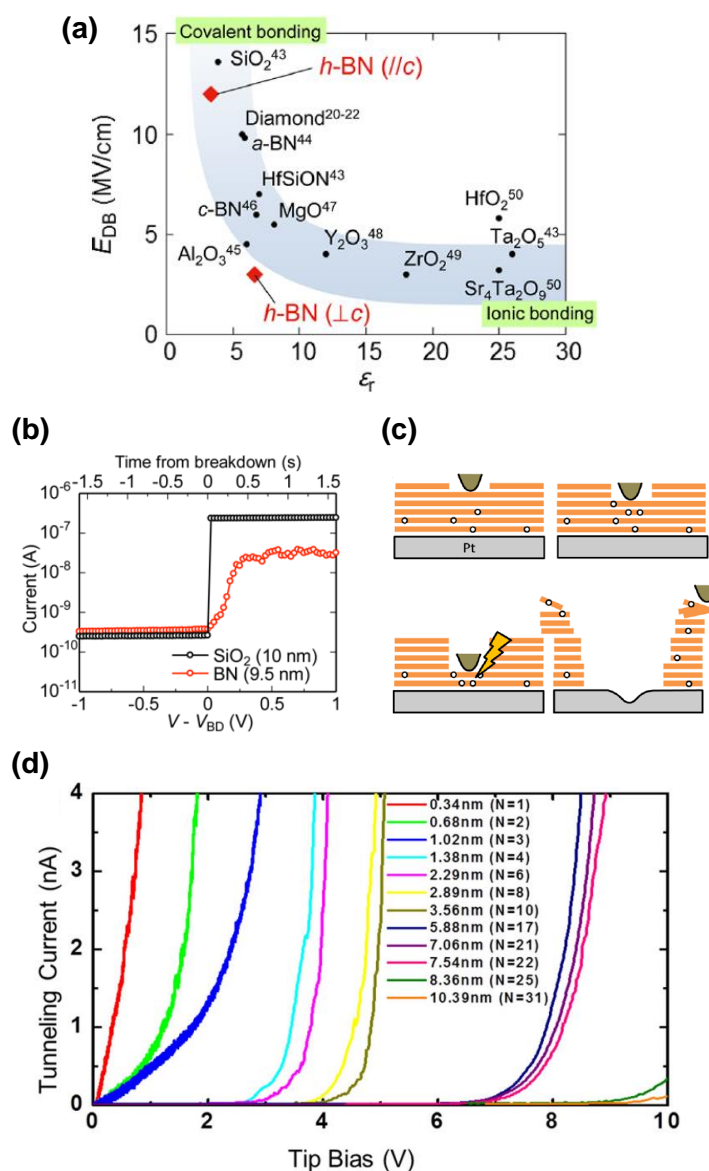


**Figure 3-4** (a) Measured break down strength and dielectric constants of in-plane and out-of-plane directions of exfoliated h-BN flakes.[8] (b) *I-V* curves measured for $SiO_2$ and h-BN.[9] (c) Schematic model of "layer-by-layer" breakdown in multilayer h-BN.[9] (d) Tunneling currents with different bias voltages measured for h-BN with the

### 3.1.5  Surface roughness

The planar structure of h-BN is attributed to the $sp^2$-network, which makes its surface atomically flat. Surface roughness, root-mean-square (RMS) of single crystal h-BN measured by atomic force microscope (AFM) is 68 pm-170 pm, according to previous literatures.[11,12] This value is comparable to that of graphite surface which is also atomically flat. The surface flatness is also influenced by the substrate on which either h-BN or graphite (graphene) is deposited.   On $SiO_2$ substrate whose surface is slightly rough, the increase of the h-BN thickness makes the h-BN surface, as shown in Figure 3-5a,b. Table 3-2 compares RMS values obtained for various materials.[12] The surface of h-BN is flat when compared with other conventional insulating materials. In addition, the h-BN surface is chemically inert and free from dangling bonds. Therefore, the using h-BN as a substrate makes other two-dimensional materials (such as graphene) flat (Figure 3-5c),[13] contributing observation of intrinsic physical properties of two-dimensional materials by reducing the surface roughness of the original substrate and also screens effects from charged impurities and dangling bonds existing on the original substrate.

**Table 3-2** surface roughness of different materials (modified from ref. 12).

| | h-BN | WSe$_2$ | MoS$_2$ | SiO$_2$ | Fused silica | Sapphire | Silicon | SrTiO3 | AlN | SU-8 |
|---|---|---|---|---|---|---|---|---|---|---|
| RMS surface roughness (nm) | 0.17 | 0.19 | 0.09 | 0.53 | 2.3 | 0.63 | 1.0 | 2.8 | 26.2 | 3.7 |
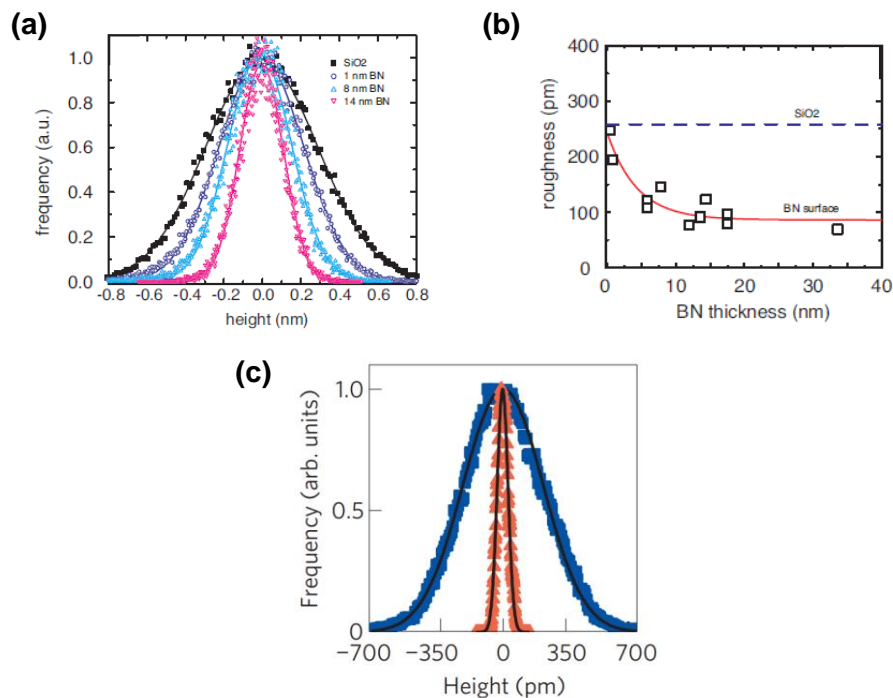
**Figure 3-5** (a) Height distributions of h-BN surfaces with different thicknesses on SiO$_2$ surface.[11] (b) Relationship between roughness and thickness of multilayer h-BN.[11] (c) Height distributions of monolayer graphene on h-BN (xxx nm thickness, red triangles) and SiO$_2$ (blue squares) surfaces.[13]

## 3.1.6   Surface charged impurities

Charged impurities cause fluctuations in Coulomb potential, strongly affecting physical properties of various 2D materials. This fluctuation effect has been mainly observed as degradation of electronic and optical properties. Thanks to sp$^2$ bonding in a h-BN layer, the h-BN surface is free from dangling bonds and charged impurities. The density of charged traps was experimentally investigated, and it was found the potential fluctuation is 1-2 order of magnitude lower than that of SiO$_2$ , as seen in Figure 3-6a,b.[14] This low density of charged traps of h-BN was shown to improve Fermi level fluctuation in graphene as compared with graphene on a SiO$_2$/Si substrate. Figure 3-6c,d depicts

that the potential variation in the monolayer graphene is significantly suppressed by employing h-BN as a substrate.[13]
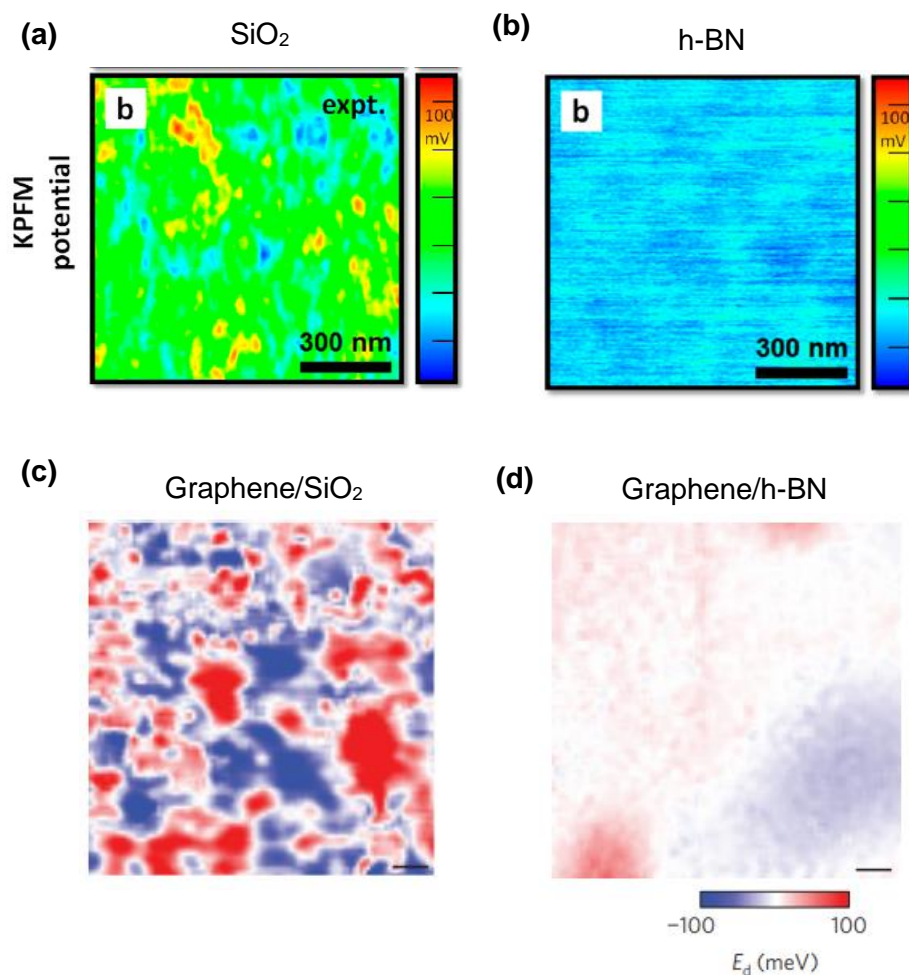


**Figure 3-6** Potential mapping of $SiO_2$ (a) and h-BN (b) surfaces measured by Kelvin probe microscopy under ultra-high vacuum condition.[14] Spatial mapping of Dirac point voltage of graphene deposited on $SiO_2$ (c) and multilayer h-BN (d).

### 3.1.7 Surface optical phonons

Surface optical (SO) phonons in insulators are an important parameter which decide a scattering rate of charge carriers (remote phonon scattering) at a temperature above

room temperature, particularly because the increased temperature enhances lattice vibrations. The SO phonon energy ($\hbar\omega_{SO}$) is determined by[15]

$$\hbar\omega_{SO} = \hbar\omega_{LO} \left( \frac{1 + 1/\varepsilon_0}{1 + 1/\varepsilon_\infty} \right) \tag{1}$$

where $\hbar$ is the Planck constant, $\omega_{LO}$ is the frequency of the longitudinal-optical (LO) phonon of an insulator. $\varepsilon_\infty$ ($\varepsilon_0$) is the high (low) frequency dielectric constant of an insulator. There are two main factors in SO phonons that affects the behavior of carries. First one is the polarizability of an insulator. Highly polarizable materials, such as $HfO_2$ and $ZrO_2$, have highly polarized chemical bonds (Hf-O, Zr-O) due to their large differences in the electronegativities of each element, resulting in "softening" bonds of SO phonons with low energy. The vibrations of the soft bonds induce Coulomb field, which interacts with carriers. Another one is difference between $\varepsilon^0$ and $\varepsilon^\infty$ of insulators. The following equation related to scattering strength (I) describes this point [16]

$$I = \hbar\omega_{SO} \left( \frac{1}{\varepsilon_{\infty(S)} + \varepsilon_{\infty(I)}} - \frac{1}{\varepsilon_{\infty(S)} + \varepsilon_{0(I)}} \right) \tag{2}$$

Where $\varepsilon_{\infty(S)}$ ($\varepsilon_{0(S)}$) and $\varepsilon_{\infty(I)}$ ($\varepsilon_{\infty(I)}$) are high (low) frequency dielectric constants of semiconductor and insulator, respectively. This equation is proportional to coupling strength between two excited electrons in semiconductor and SO phonons in insulator. Therefore, a large difference between $\varepsilon^0$ and $\varepsilon^\infty$ enhance scattering arising from SO phonons. Regarding the SO phonons, h-BN is also suitable as an insulator of 2D materials, because the B-N bond is relatively stiff due to its small electronegativity difference between B and N atoms and it has small difference between $\varepsilon^0$ and $\varepsilon^\infty$. The dielectric constants and SO phonons of several insulators are summarized in Table 3-3.[7,17,18]

|  | h-BN | SiO$_2$ | AlN | Sapphire | HfO$_2$ | ZrO$_2$ |
|---|---|---|---|---|---|---|
| $\varepsilon^0$ | 3.76 | 3.90 | 9.14 | 12.53 | 23.00 | 24.00 |
| $\varepsilon^\infty$ | 3.03 | 2.50 | 4.80 | 3.20 | 5.03 | 4.00 |
| $\omega^1_{SO}$ (meV) | 96.63 | 55.60 | 81.40 | 48.18 | 12.40 | 16.67 |
| $\omega^2_{SO}$ (meV) | 189.96 | 138.10 | 88.55 | 71.41 | 48.35 | 57.70 |

**Table 3-3** High and low frequency dielectric constants and SO phonon energies calculated for different insulators.[7,17,18]

### 3.1.8  Oxidation resistance

h-BN has strong oxidation resistance even when it has monolayer thickness. In bulk h-BN, oxidation starts from 1000 °C in air.[19] According to the experimental demonstration that investigated the oxidation resistance using Raman spectroscopy, the resistant temperature of few-layer h-BN is lower (few-layers are stable up to 600 °C) than bulk h-BN. In the case of 1-4 layers h-BN flakes exfoliated on SiO$_2$/Si substrate, their Raman E$_{2g}$ band starts to change from 700 °C. As shown in Figure 3-7a, the E$_{2g}$ intensity decreases and shifts to higher wavenumbers, suggesting the structural damage to the h-BN sheets .In particular, the monolayer h-BN flake is completely oxidized at 800 °C.

Theoretical calculations suggest that h-BN is thermally stable, because the energy barrier for the adsorption of oxygen molecules is higher than that of desorption energy.[20] However, at high temperatures, an oxygen molecule chemisorbed on the h-BN surface form B-O-N bonds, leading to the chemical etching of h-BN.[20–22] The strong oxidation resistance and impermeable in-plane structure of h-BN make it an attractive protection layer for other materials to prevent from oxidation. As shown in Figure 3-7b,c, the

graphene coated with 2 nm-thick h-BN retain its structure even at 1000 °C in air, while bare graphene is completely oxidized at 1000 °C.[23]
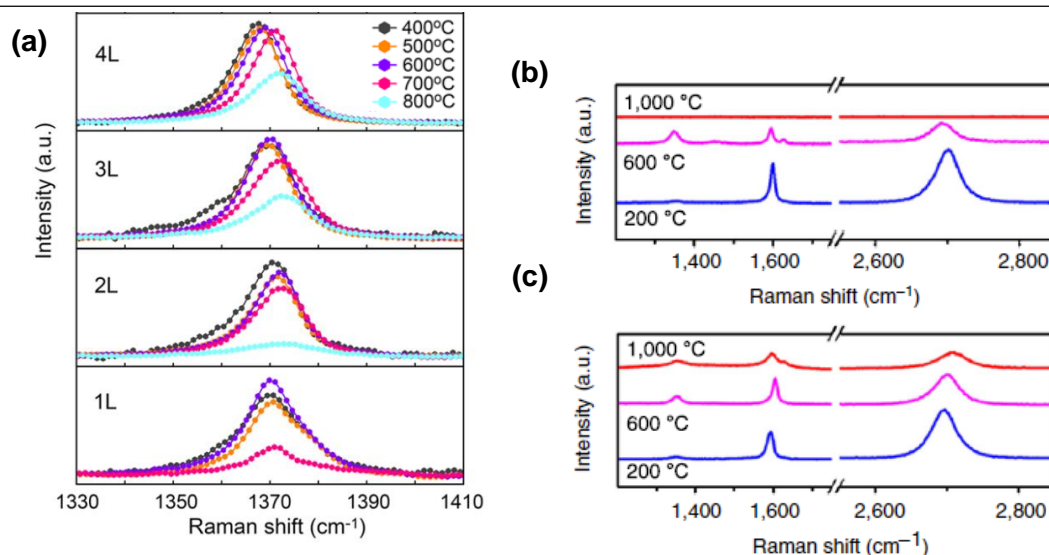


**Figure 3-7** (a) Raman spectra of 1-4 layer and bulk h-BN after sequential heating at 400, 500, 600, 700, and 800 °C in air.[15] Raman spectra of h-BN-covered (b) and uncovered (c) graphene heated at 200, 600, and 1000 °C in air.[19]

## 3.2   Synthesis of 2D h-BN sheets: Top down approach

### 3.2.1   Mechanical exfoliation

For fundamental studies, h-BN flakes are widely obtained from the bulk single crystal by mechanical exfoliation using adhesive tape. Figure 3-12 displays the exfoliation process of h-BN.   This is a simple and facile method to obtain thin h-BN flakes with high-quality, because bulk single crystals are employed as starting material, although highly pure, bulk h-BN crystals can be obtained only in limited groups. Other 2D materials can be also peeled off from the corresponding layered materials. Recently, this simple method has been improved after the success of graphene exfoliation. For example, the mechanical exfoliation of thin graphene flakes with a lateral size of few hundred $\mu$m was

demonstrated by proper annealing SiO$_2$ substrate contacted with graphite decorated adhesive tape, while the conventional method usually gives flakes with a few μm size.[24] More recently, the positions of exfoliated flakes can be controlled by using a stamping method using Polydimethylsiloxane (PDMS).[25] This method allows to prepare various vertically stacked vdW heterostructures efficiently.[26] Also, elimination of contamination at the interface between layers of vdW heterostructure has shown progress. However, this exfoliation method is not suitable for practical applications, because there is large limitations in flake size and uniformity.
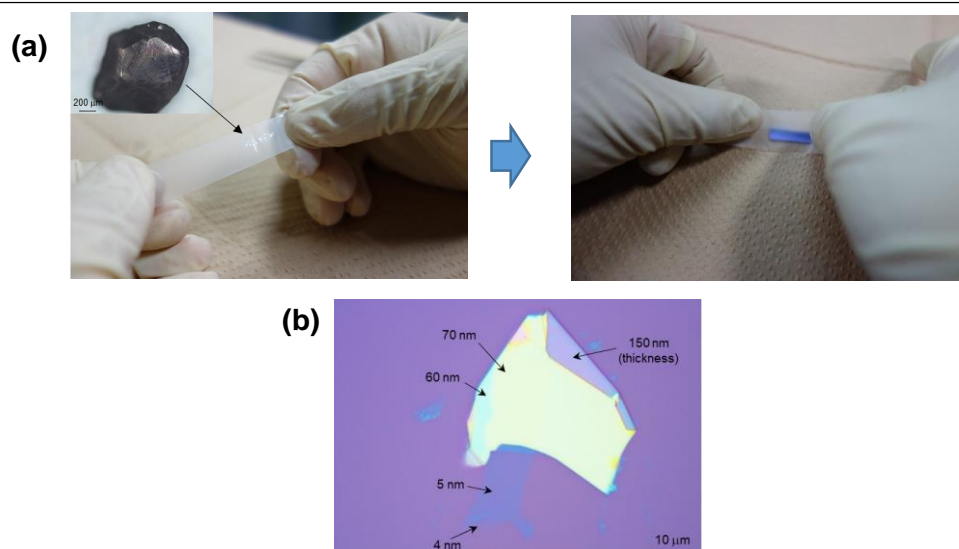


**Figure 3-12** (a) Photographs showing mechanical exfoliation of h-BN using adhesive tape. (b) Optical microscope image of an exfoliated h-BN flake.

## 3.2.2 Liquid-phase exfoliation

Liquid phase exfoliation (LPE) is a promising method to produce large quantities of dispersed thin h-BN flakes at low cost, suitable for mass production.[27] Figure 3-13 shows a schematic of the LPE process. The driving force of exfoliation is weakening the interlayer vdW interaction by intercalating solvent and/or surfactant or inducing chemical reactions at each layer. Also, additional treatments including ultra-sonication and ball

milling are frequently used to promote the exfoliation.[28,29] The exfoliation is relatively difficult as compared with graphene exfoliation due to the ionic nature of h-BN layers, recent studies have demonstrated effective LPE by controlling exfoliation processes as well as solvent.

By spraying the dispersion, a large-area h-BN sheet can be obtained, and this method was applied to prepare various h-BN-based vdW heterostructures by using dispersions of other 2D materials.[30] Furthermore, the solution processable h-BN can be used as functional ink, which allows to "print" 2D materials-based electronics.[31] However, since the lateral size of exfoliated flakes is very small (~ a few μm), the obtained h-BN sheet made by spraying h-BN dispersion has a poor connection between flakes. The crystallinity of exfoliated h-BN flakes degrades during the LPE process as it is difficult to avoid damages introduced by exfoliation, such as sonication. These disadvantages, small flake sizes and unavoidable damages, limit the application to electronic devices.
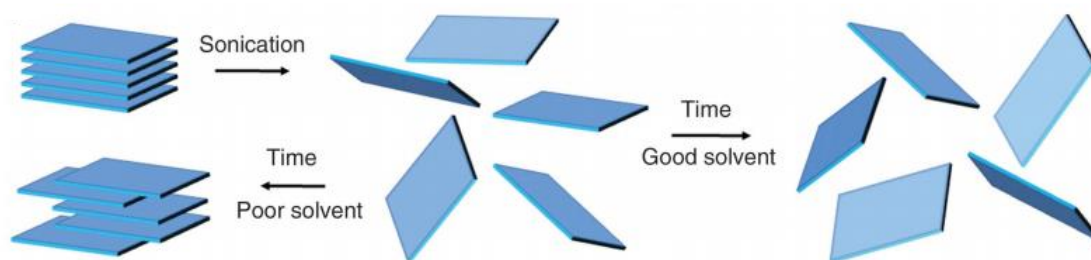


**Figure 3-13** Schematic of the LPE of h-BN.[30]

## 3.3   Synthesis of 2D h-BN sheets: Bottom up approach

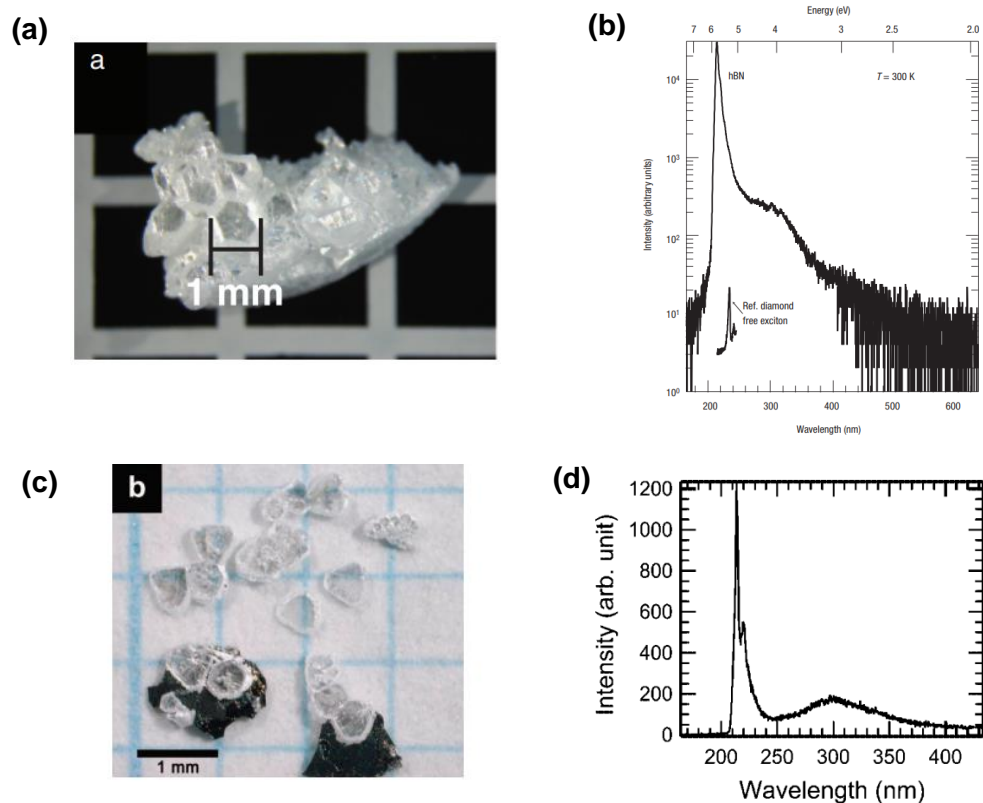### 3.3.1   High pressure, high temperature (HPHT) method

The h-BN used in most of the recent publications is obtained by exfoliating from single-crystal bulk h-BN, which is synthesized by high pressure, high temperature (HPHT) method. This HPHT method is also applied to diamond synthesis. In particular h-BN crystals synthesized by the high-pressure group in NIMS is known to be of high-quality so that a large number of groups are currently using their samples.

The group in the National Institute for Materials Science (NIMS), Japan utilizes the dissolution and segregation processes of B and N atoms in a purified solvent (typically transition metals which are liquefied during the reaction) under an extremely high temperature and high pressure condition.[32] In their method, h-BN powder is used as source material and dissolved in a suitable purified solvent at high temperature. In the very slow cooling process, B and N atoms are segregated as h-BN single crystals due to the reduction of the B, N solubilities in the metal.

In this method, the selection of the solvent is very important, and the following properties of solvent are required for the growth of high-quality h-BN crystals.[32] (1) sufficiently high solubilities for both B and N atoms, (2) thermodynamic stability during the reaction under high temperature and high pressure, (3) availability of refining process to remove impurities, such as oxygen and carbon, and (4) low contamination level of the solvent itself. They found that a solvent that contains barium (Ba), B, and N satisfies the above requirements. Prior to the reaction with h-BN powder, the solvent is annealed at 2100 °C for 2 hours in pure $N_2$ environment in order to remove oxygen impurities. Purified h-BN powder and the solvent are set inside a molybdenum (Mo) sample cell, followed

by applying HPHT (5.5 GPa, 1500-1750 °C) to proceed the dissolution reaction. This condition is maintained for long period of time (20-80 hours). Figure 3-14a shows a colorless, transparent h-BN crystal obtained by the HPHT method. The crystal shows strong cathode luminescence (CL) peak in the deep UV region (Figure 3-15a), signifying high crystallinity of the product.[32]

h-BN is thermodynamically stable under high temperature and atmospheric pressure. This suggests that h-BN can be synthesized at high temperature but without extremely high pressure. Therefore, the group in NIMS also demonstrated the growth of h-BN single crystals under atmospheric pressure using a Ni-based solvents, such as Ni-Mo and Ni-Cr.[33,34] Because solubility of N in Ni metal is very low (Ni has efficient solubility for B), they used Ni-Mo and Ni-Cr solvents to increase the N solubility. This ambient-pressure growth was performed at 1500 °C for 12 hours. After that, the sample cell was gradually cooled down to 1200 °C at a rate of 4 °C/h, resulting in the formation of highly crystalline h-BN crystals (see Figure 3-14c,d). As seen in Figure 3-14a,c, typical lateral size and thickness of the as-grown h-BN crystals are 1 mm$^2$ and 200-500 $\mu$m, respectively. To date, the growth of large area h-BN sheet has not been achieved by this method, limiting the application of the h-BN crystal only to basic science. However. the basic concept is useful for other bottom-up approaches, such as a catalytic CVD method described below.

**Figure 3-14** (a) Photograph of single crystal h-BN obtained by HPHT method and (b) the CL spectrum.[35] (c,d) Photograph and the CL spectrum of the h-BN crystal grown under high temperature and ambient pressure.[37]

### 3.3.2 Physical vapor deposition (PVD)

PVD is a simple but widely used method to deposit a thin film (generally, ranging from a few nm to a few μm) on a desired substrate. The method comprises the following steps: (1) vaporization of solid source materials by several ways, such as thermal evaporation, ion gas collision, irradiating laser with high energy, and electron beam, (2) transportation of vaporized gases to a target substrate under low pressure or high vacuum, (3) adsorption and diffusion of vaporized molecules on the target substrate, (4) nucleation by aggregating diffused atom and molecules, and finally (5) a thin film is formed on the substrate. As shown in Figure 3-15a, PVD can be classified into several

types according to the pressure, the method to deposit a material, and a target substrate. After the first report on graphene/h-BN heterostructure in 2010,[11] many researchers have tried to grow high-quality h-BN films by PVD. Recently, large grain size with controlled orientation was obtained by a sputtering method (Figure 3-15b).[35] Molecular beam epitaxy (MBE) have been also used for the growth of h-BN film.[36] Thanks to the ultra-high vacuum environment used in MBE, there is a possibility of growing h-BN in a more controlled manner, such as controlled crystal morphology and orientation (Figure 3-15c). Segregation process can be also used to obtain a thin film.
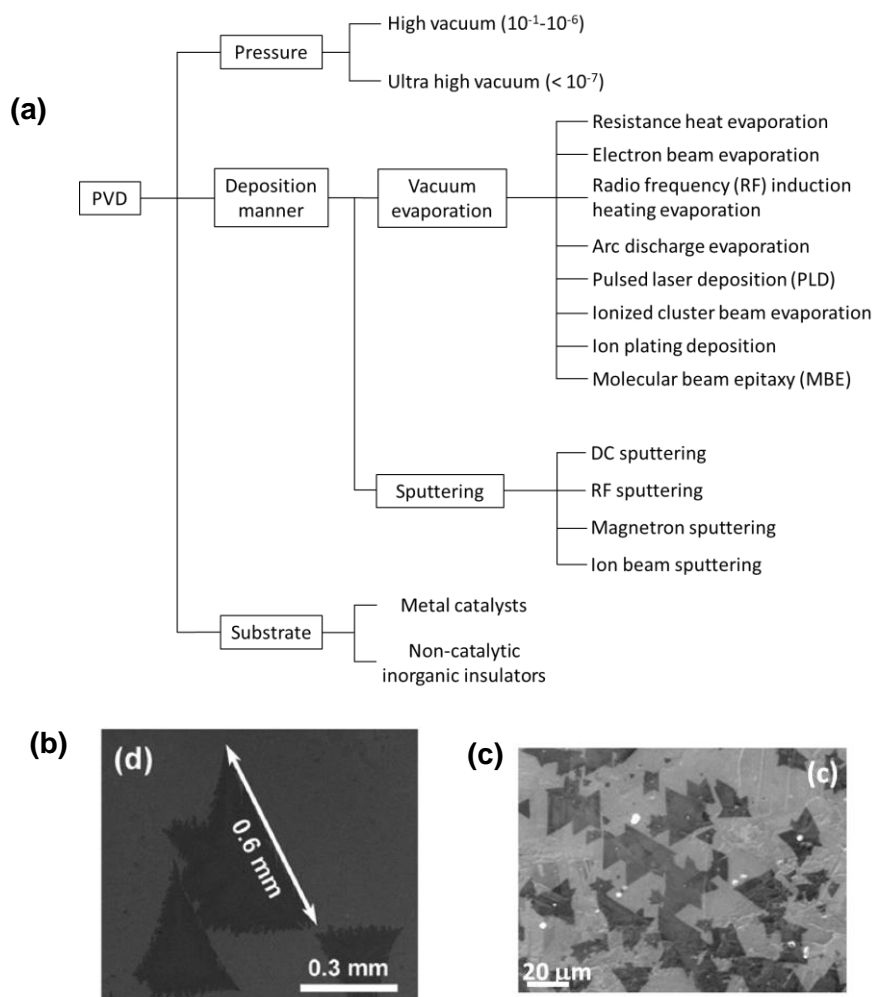


**Figure 3-15** (a) Classification of PVD methods. SEM images of monolayer h-BN grains grown on Ni(111) by sputtering (b)[38] and on Co foil by MBE (c),[39]

### 3.3.3  Chemical vapor deposition (CVD)

A CVD method, like PVD, is well established technology to deposit thin films. CVD methods for growing thin films includes the following steps: (1) Precursor transport via vaporization of a solid or liquid sources or introduction of gases molecules, (2) transportation onto a target substrate, (3) decomposition and/or diffusion of molecules on the substrate, (4) nucleation by agglomerating surface-adsorbed atoms and molecules (or intermediate species) through the surface diffusion or diffusion within a substrate (catalyst), and (5) final formation of a thin film.

The main difference of CVD from PVD is the presence of chemical reaction and feasibility to grow films even under atmospheric pressure. Because chemical reactions are involved in the CVD process, CVD is expected to grow large area h-BN sheet with controllable shape and thickness. Since the reports on the application of h-BN to an ideal dielectric layer for 2D materials, such as graphene,[36] the CVD synthesis of h-BN sheets have been attracting increased interest. In CVD growth of h-BN, various substrates and a wide variety of precursors have been studied. An important point to grow high-quality h-BN is controlled decomposition of precursors. In the case of non-catalytic substrate, very high temperature (1200 ºC) or other methods to activate precursor is necessary for obtaining h-BN sheets.

CVD methods are classified into several types depending on the growth condition, activation method, and substrate, as listed in Figure 3-16. Thermal CVD is the most widely employed method to grow h-BN film, because a high-quality h-BN can be obtained with a simple CVD setup which makes the production cost lower. Also, transition metal films/foils are widely used as substrate which act as a catalyst that promotes decomposition of the feedstock and also assists the formation of hexagonal BN network.

In addition, the thermal CVD also allows to control the morphology of h-BN due to the simple setup. It is noted that in the h-BN CVD, growth the selection of precursor is very important. In the next sections, the CVD growth with different types of metal catalysts as well as precursors are described.
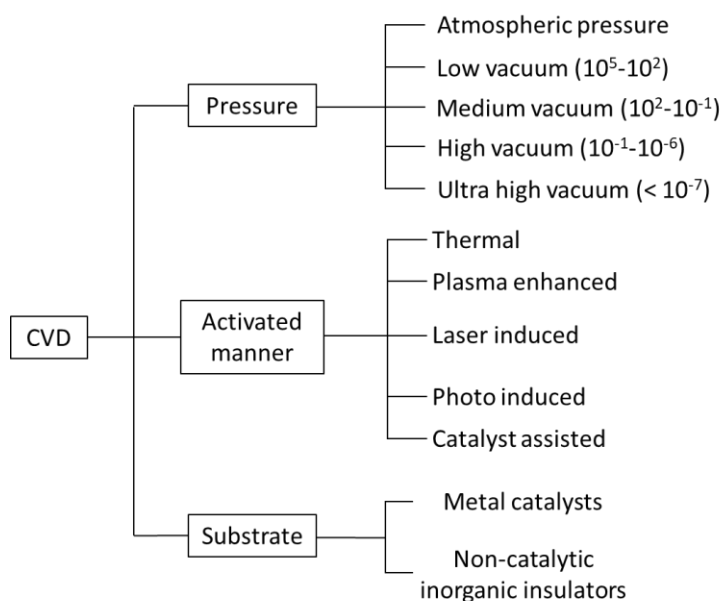


**Figure 3-16** (a) Classification of CVD methods.

### 3.3.4 Metal catalysts for CVD growth of h-BN

In this section, roles of metal catalysts used in thermal CVD is discussed. Figure 3-17 presents schematic of CVD growth of h-BN monolayer on a metal catalyst. Concerning a catalytic activity, metal catalysts tend to reduce the growth temperature (900-1100 °C) of h-BN. On the other hand, on metal oxide substrates, such as $SiO_2$/Si and sapphire, relatively high temperatures are required to form h-BN network (e.g. formation of h-BN from ammonia borane ($BH_3NH_3$) requires the growth temperature as high as 1170-1500 °C).[37] Actually, the crystallinity of h-BN grown on the oxide
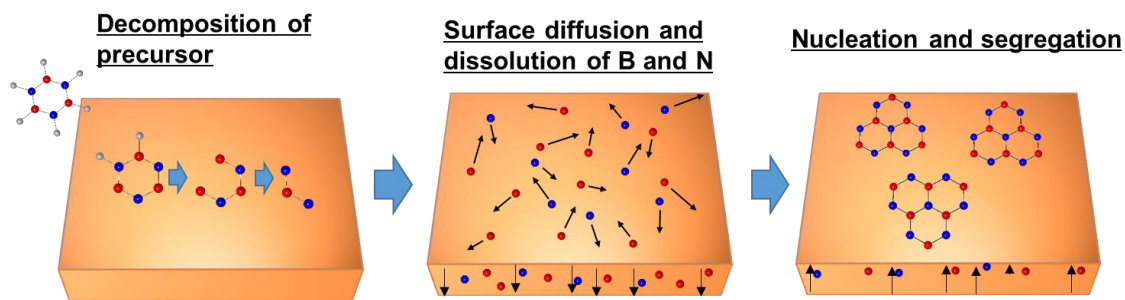
**Figure 3-17** Schematic of CVD reaction on metal catalysts

substrates is generally low. As shown in Figure 3b, the Raman $E_{2g}$ peak of h-BN is very broad when it is grown on $SiO_2$ substrate.[38] On the other hand, most of the metals have a catalytic activity to decompose BN precursors and also to form hexagonal lattice of boron nitride. Therefore, the h-BN grown on a metal catalyst shows relatively sharp $E_{2g}$ peak (see Figure 3-17 c,d).[39] Catalytic activity of several transition metals have been investigated in literatures.[40,41] One paper suggested that Ni tends to dehydrogenate and dissociate B-N bonds of a precursor more effectively, as compared with Cu catalyst, because of the formation of Ni-B and Ni-N phases when Ni is used as catalyt.[40] However, the exact roles of a catalyst in the h-BN growth is still unclear due to lack of systematic investigation on catalytic activity of different metals.

The control of the orientation of h-BN grains (i.e. lattice) is important for a possibility of stitching of neighboring h-BN grains. Although it is not experimentally verified, the aligning of h-BN grains (also for graphene grains) is important for the atomically seamless connection between the neighboring grains. The grain boundaries (GBs) formed in misoriented grains deteriorates the physical properties of h-BN sheets, because mechanical breakage occurs at the GBs. Moreover, the orientation-controlled growth of h-BN at large-scale is also helpful for preparing vertically stacked vdW heterostructures with a controlled stacking angle.[42–44] The $\pi$ orbital of N atoms in h-BN
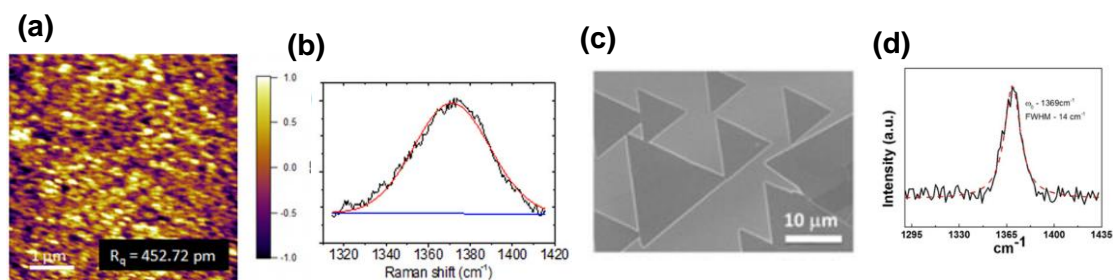
**Figure 3-18** AFM image (a) and Raman spectrum (b) of h-BN nanocrystals grown on SiO$_2$.[42] SEM image (c) and Raman spectrum (d) of h-BN grown on Cu foil.[43]

sheet interacts with d orbital of transition metals due to the overlap of these orbitals.[45] It is known that transition metals having a fcc(111) crystal plane promotes the alignment of h-BN in specific two directions (Figure 3-19a,b).[46]
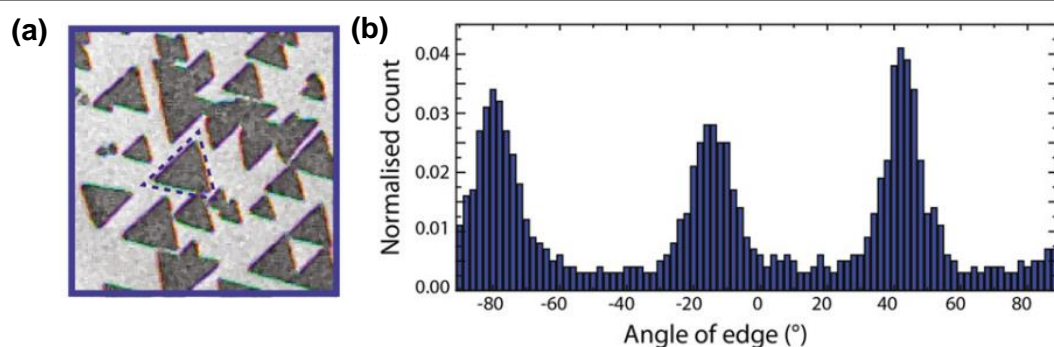


**Figure 3-19** (a) SEM image of aligned h-BN grains grown on Cu foil by thermal CVD method. (b) Distribution of the h-BN orientation on Cu(111) area in the foil.[50]

In addition to the grain orientation, which is related to the grain stitching, thickness of h-BN films is very important for the applications to many fields. Actually, many research groups have tried to control the h-BN thickness by CVD. Cu metal, which is known to give a uniform monolayer graphene sheet, has been frequently studied as a metal catalyst. Because Cu has almost no N solubility and relatively high solubility for B atoms, monolayer h-BN preferentially grows on the surface of Cu, being similar to the surface limited growth seen in the graphene CVD, as illustrated in Figure 3-20a.[47] Therefore, Cu is not a suitable catalyst for the growth of multilayer h-BN which is more

important for practical applications.[48–50] Fe has relatively high both B and N solubility, so that multilayer h-BN with relatively high crystallinity is easily obtained (Figure 3-20b).[51,52] Therefore, B and N solubility should be considered for the management of the thickness of h-BN.

**(a)**

**(b)**
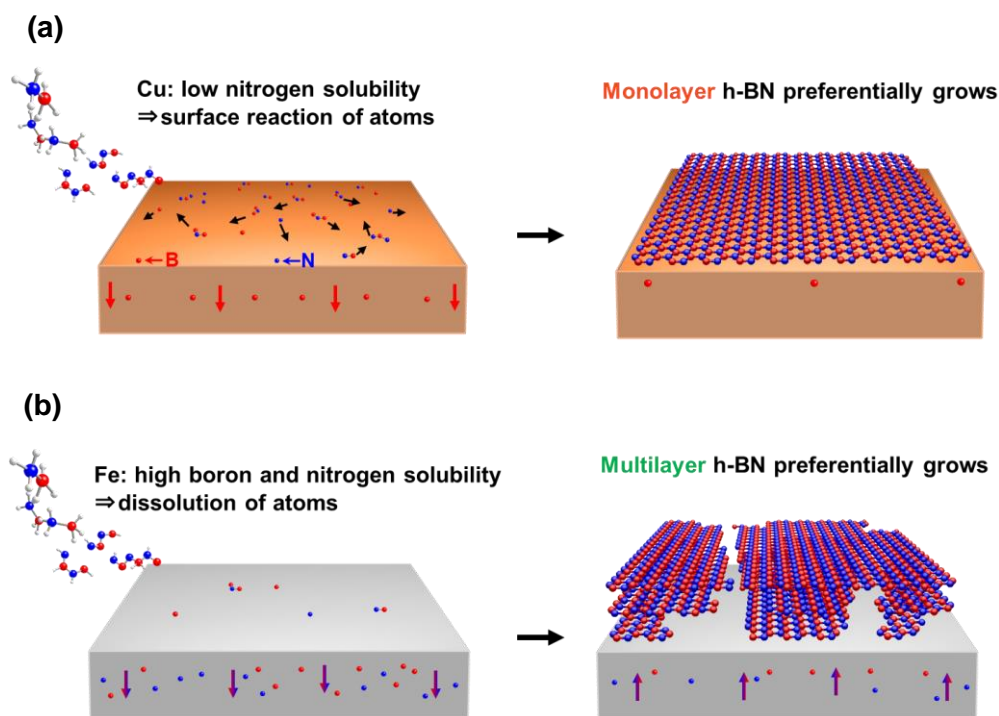


**Figure 3-20** (a) Schematic of the growth of monolayer h-BN on Cu. (b) Schematic of the growth of multilayer h-BN on Fe.

### 3.3.5 Precursors used in CVD growth of h-BN
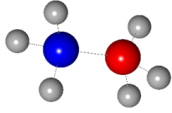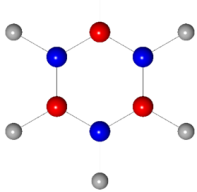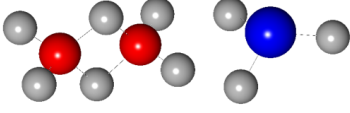
In this section, precursors used in the CVD growth of h-BN are discussed. in the selection of precursors, vapor pressure, thermal stability (ease of decomposition), and controllability should be considered. Various precursors, including solid, liquid, and gas sources, have been investigated. Among them, ammonia borane ($BH_3NH_3$), borazine ($B_3N_3H_6$), and a mixture of diborane ($B_2H_6$) and ammonia ($NH_3$) are the most commonly

used feedstock. Here, ammonia borane and borazine are solid and liquid in ambient condition, respectively. Advantages and disadvantages of these main precursors are summarized in Figure 3-21.

In CVD growth of h-BN, ammonia borane ($BH_3NH_3$) has been widely used, because it is not expensive and easy to handle in air due to its stability.[53] For example, decomposition $BH_3NH_3$ does not occur over two months at room temperature and it does not sublime due to a low vapor pressure of $\sim 10^{-2}$ Pa at room temperature.[53] $BH_3NH_3$ decomposes into the gaseous $B_3N_3H_6$, the solid poly-aminoborane ($BH_2NH_2$) and a small amount of $B_3N_3H_6$.[37,54] In addition, , byproducts are also easily formed due to the polymerization of intermediates, giving polymer particles attributed to $BH_2NH_2$.[41] Therefore, a special attention is necessary, because impurities, such as polymer , are formed duing the decomposition of the $BH_2NH_2$ feedstock.

On the other hand, borazine ($B_3N_3H_6$) is a molecule structurally similar to benzene ($C_6H_6$) and is isoelectronic to benzene. Therefore, $B_3N_3H_6$ is sometimes called as inorganic benzene. Therefore, borazine ($B_3N_3H_6$) is a good candidate for the catalytic growth of h-BN. In addition, according to several reports, it is likely that h-BN produced from $B_3N_3H_6$ is of high purity, because side reactions do not occur frequently is hard to occur.[55–58] However, $B_3N_3H_6$ is flammable liquid, and decomposes quickly at room temperature, and also it is expensive.

Generally, gas precursors are very useful for controlling the flow rate as well as the concentration (partial pressure). The introduction of mixture of $NH_3$ and $B_2H_6$ gases also produce h-BN crystalsm, though the latter is very difficult to handle due to its high chemical reactivity.[59,60] Expensive facilities are required to use these precursors, because these gases are toxic and flammable.

**Figure 3-21** Precursors widely used for the CVD growth of h-BN.

## 3.4 Theory of CVD growth

### 3.4.1 Boundary layer and gas diffusion[61]

In a horizontal CVD furnace, a boundary layer with a slow flow rate is formed on the substrate surface (Figure 3-22). Mass flux velocity along the boundary layer is given by the following equation:[61]

$$J_b = k_b(P - P_i) \tag{3}$$

Here, $k_b$ is mass transfer coefficient, $P$ is partial pressure (or concentration) of precursor outside of the boundary layer, and $P_i$ is partial pressure (or concentration) at the interface of the boundary layer. $k_b$ is expressed by the following equation (Fick's first law of diffusion):

$$k_b = \frac{D}{\delta} \tag{4}$$

Where $D$ is diffusion coefficient and $\delta$ is thickness of the boundary layer. Therefore, growth rate of a film is influenced by pressure (or concentration) gradient between the boundary layer and thickness of the boundary layer. The thickness can be controlled by changing a flow rate of gase, which is described by following equation:[61]

$$\delta \approx \sqrt{\frac{vx}{u}} \tag{5}$$

where $v$ is kinetic viscosity, $x$ is distance from the edge of the substrate, and $u$ is flow rate of gases. In case of relatively thick boundary layer, after switching the gas, the response in the boundary layer is delayed. For example, delayed response results in difficulty to make steep heterostructures. Recently vacuum ($10^{-1}$-$10^{-2}$ Pa) CVD is expected to exclude such delay, because of its high flow rate.
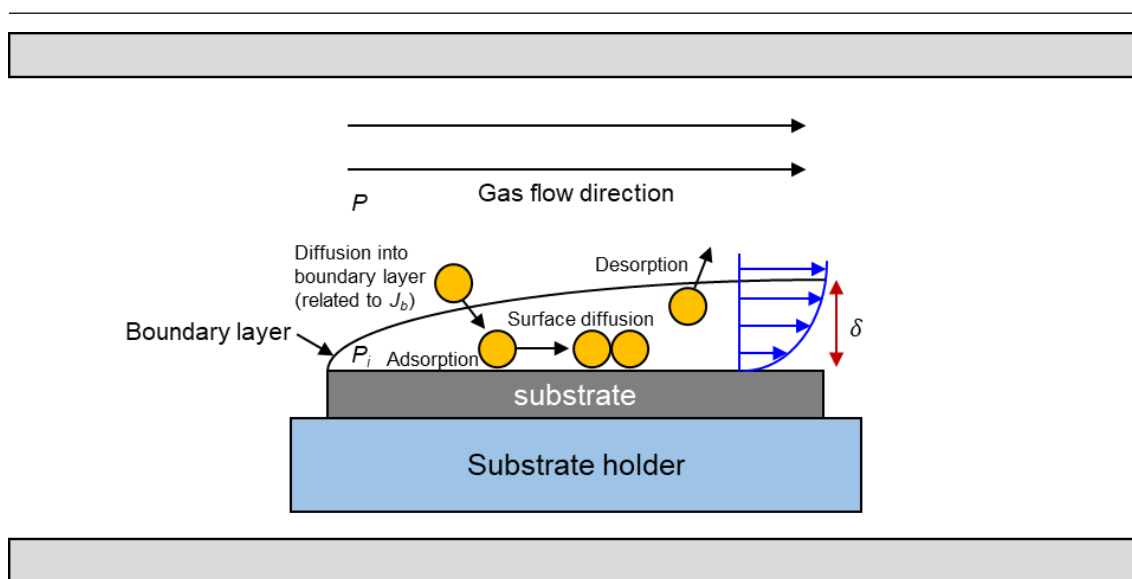


**Figure 3-22** Behavior of gaseous molecules in the tubular CVD reactor.

### 3.4.2  Nucleation of crystals on substrates[62]

Phase change, such as solidification from gases, is driven by the chemical potential difference ($\Delta\mu = \mu_{gas} - \mu_{solid}$), as shown in Figure 3-23a. Growth rate of crystals ($V$) is proportional to the chemical potential gradient, which is given by the following equation:[62]

$$V = K\Delta\mu \tag{6}$$

Here, $K$ is Kinetic growth coefficient, depending on temperature and substrate surface condition including crystal orientations. In isothermal process, chemical potential gradient between two different phases is determined by the concentration gradient. Thus, concentration gradient in the interface between substrate surface and its surroundings leads to nucleation of crystals. However, when nuclei are formed, the free energy increases in proportion to the surface area of the nucleus until the nuclei become sufficient size, resulting in the high evaporation rate of nuclei. Therefore, sequential crystal growth requires seed crystals with a certain size or larger. Figure 3-23b-d shows size dependence of seed crystal on incidence rate of precursors and evaporation rate of seed crystals per unit area in different incident rate conditions. As can be seen in this figure, the evaporation rate decreases with increasing the size of seed crystals. In the unsaturated condition ($\Delta\mu < 0$) (Figure 3-23b), the evaporation rate is higher than the incident rate, which means that no nucleation of crystals occurs. By increasing the incident rate or decreasing temperature for reducing evaporation rate, equilibrium ($\Delta\mu \approx 0$) or supersaturated ($\Delta\mu > 0$) conditions can be made (Figure 3-23c,d). In the supersaturated condition, sequential crystal growth occurs by seed crystals with a size larger than $N_c$ (critical nucleus size) (Figure 2-23d).

**(a)**

Gas precursors: $\mu_{gas}$

Crystals: $\mu_{solid}$

substrate

$$\Delta\mu = \mu_{gas} - \mu_{solid}$$

$\Delta\mu > 0 \Rightarrow$ solidification
$\Delta\mu < 0 \Rightarrow$ evaporation of crystals

**(b)**

Concentration of gases

Evaporation rate of seed crystals

**Unsaturated condition**
**($\Delta\mu < 0$ )**

Incident rate of precursors

Size of seed crystal

**(c)**

Concentration of gases

Evaporation rate of seed crystals

**Equilibrium condition**
**($\Delta\mu \approx 0$ )**

Incident rate of precursors

Size of seed crystal

**(d)**

Concentration of gases

Evaporation rate of seed crystals

**Supersaturated condition**
**($\Delta\mu > 0$ )**

Incident rate of precursors

$N_c$

Size of seed crystal

**Figure 3-23** (a) Schematic of relationship between chemical potentials of gas and solid. Size dependence of seed crystal on incidence rate of precursors and evaporation rate of seed crystals per unit area in unsaturated (b), equilibrium (c), and saturated (d) conditions.

### 3.4.3 h-BN growth on metal catalysts with different solubility

Here, as an example, h-BN growth on metal catalysts with different solubility is discussed. Figure 3-24a,d shows schematic of relationship among the precursor flux ($J_i$), B and N flux into bulk ($J_b$), B, N, and their molecules flux on the surface of metal catalysts ($J_s$), and B and N evaporated flux ($J_e$) in two different metal catalysts. Crystal growth driven by these flux diffusions can be described by following equation.[62]

$$J = -D\nabla\mu \tag{7}$$

Here, $D$ is diffusion coefficient in inside of boundary layer ($D_{bo}$), substrate surface ($D_{su}$), or inside of bulk ($D_{bl}$).  $\nabla= \left(\frac{\partial}{\partial x}, \frac{\partial}{\partial y}, \frac{\partial}{\partial z}\right)$, notation for gradient.

In case of metal with low B and N solubility, effect of $J_b$ is eliminated. Given that $J_i$ is larger than $J_e$ (supersaturated condition), h-BN crystals start to grow. If $J_i$ is same as $J_e$ or slightly larger than $J_e$ (Figure 3-24b), it is expected that monolayer h-BN preferentially grows via surface diffusion of B, N, and their molecules until full coverage of h-BN sheet on metal catalysts. If $J_i$ is much larger than $J_e$ (Figure 3-24c), inhomogeneous multilayer h-BN is to be formed. However, such high supersaturated condition relies on gas-phase thermal decomposition (almost no catalytic decomposition) of precursors, so that the crystallinity of formed h-BN is low.[48-50]

In case of metal with high B and N solubility, $J_b$ should be considered and $J_b$ could be controlled by changing the thickness of metal catalysts (Figure 3-24d). In spite of large $J_b$, high supersaturated condition ($J_i \gg J_e$) could lead to inhomogeneous multilayer deposition with low crystallinity. In moderate supersaturated condition ($J_i \gtrsim J_e$), metal acts as reservoir for B and N atoms, which means additional layers can be formed by segregation during cooling after stopping $J_i$. Slow or moderate cooling rate may promote segregation of h-BN as additional layer, which has relatively high crystallinity.[51] In

contrast, fast cooling rate prevents the h-BN segregation. Therefore, control of cooling condition in the metal with high B and N solubility plays an important role to produce uniform and high crystallinity h-BN.
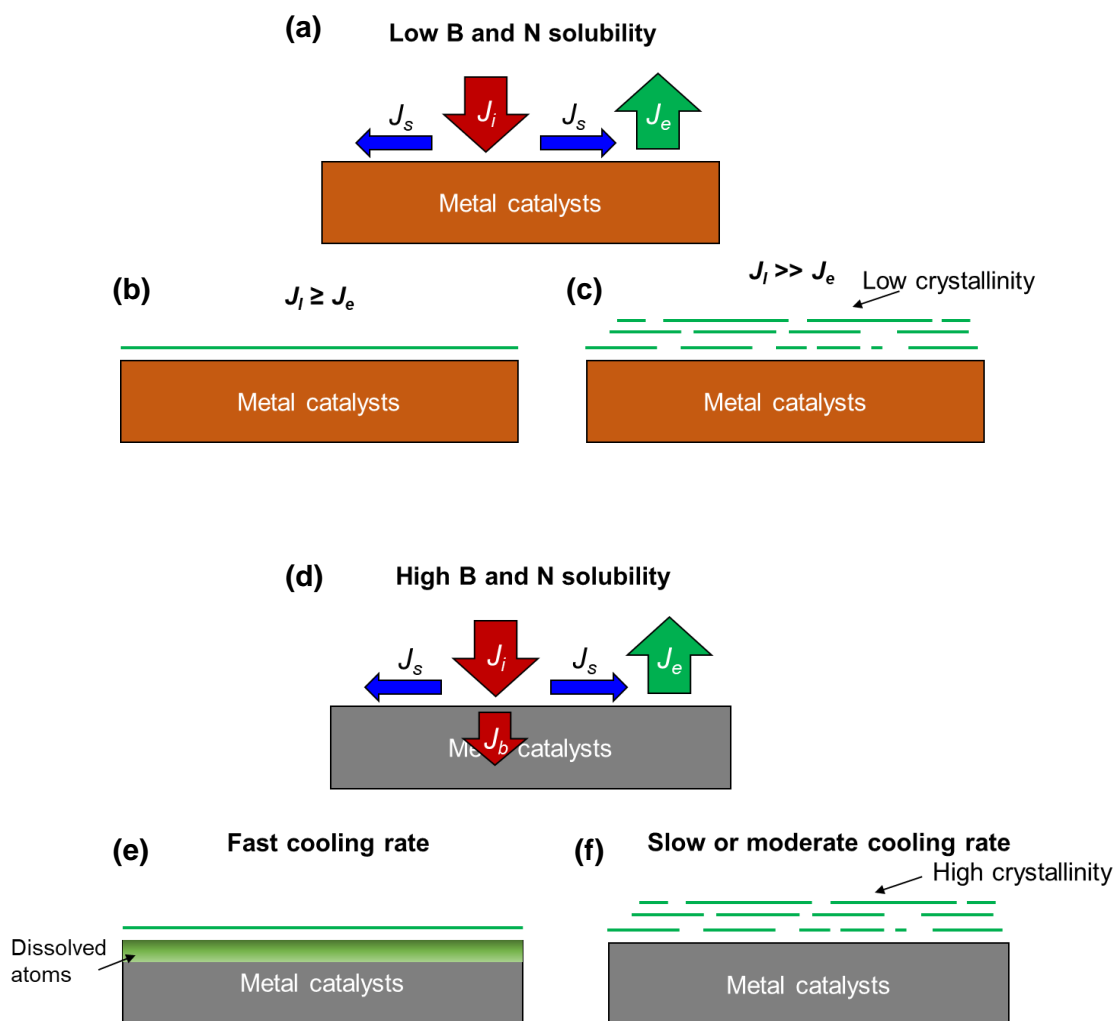


**Figure 3-24** Schematic showing relationship between $J_i$, $J_e$, $J_s$, and $J_b$ in high (a) and low (d) B and N solubility metals. Expected growth of h-BN results from $J_i \geq J_e$ (b) and $J_i \gg J_e$ (c) conditions in low B and N solubility case. Expected growth of h-BN results from fast cooling (e) and slow or moderate cooling (d) rate conditions in high B and N solubility case at $J_i \geq J_e$ relationship.

### 3.4.4  Phase diagram of metals with B and N

To control $J_b$, B and N solubility should be considered from the phase diagram. Here, the phase diagrams of Cu, Ni, and Fe with B and N are discussed. In Cu, Cu-N phase diagram was not found.[63] Cu-B phase diagram is considered as eutectic system (Figure 3-25). In this system, liquid phase with mixture of Cu and B is formed in interface at eutectic point temperature of 1013 ℃ (Figure 3-25). Then, α- or β-rhombohedral boron can be segregated by cooling. Also, B atoms up to ~0.29 at% can be dissolved into interstitial spaces of solid Cu. However, in several cases, it has been reported that N solubility is almost zero,[47,63] so that Cu is not suitable for multilayer h-BN growth via segregation.

Regarding the Ni-N system (Figures 3-26 and 3-27), conventional CVD temperature (900 ℃-1100 ℃) does not reach liquid phase with mixture of Ni and N.[63,64] Also, solubility of N in solid Ni interstitial spaces is very low (0.004-0.03 at%: value depends on references).[63,65] Ni-B phase diagram is eutectic system like Cu-B (Figure 3-26b) and its eutectic point temperature is 1093 ℃. Then, fcc Ni and $Ni_3B$ phases can be segregated by cooling. Also, solubility of B in solid Ni interstitial spaces is moderate (0.3 at% at 1085 ℃).[64]

Regarding the Fe-N phase diagram (Figure 3-28a), γ-Fe (fcc structure) has significant large N solubility (~8.0 at% at 1000 ℃).[63] However, α-Fe (bcc structure) has moderate N solubility (~0.40 at% at 592 ℃). Thus, structural transformation of Fe could trigger large amount of nitrogen compounds. Fe-B phase diagram is eutectic system like Cu-B and Ni-B (Figure 3-28b) and its eutectic point temperature is 1174 ℃.[63] Also, γ-Fe has moderate solubility of boron (~0.1 at%) (Figure 3-29c).[66] Thanks to relatively large B

and N solubility in Fe, it is a potential candidate to produce multilayer h-BN throughout

the segregation process.
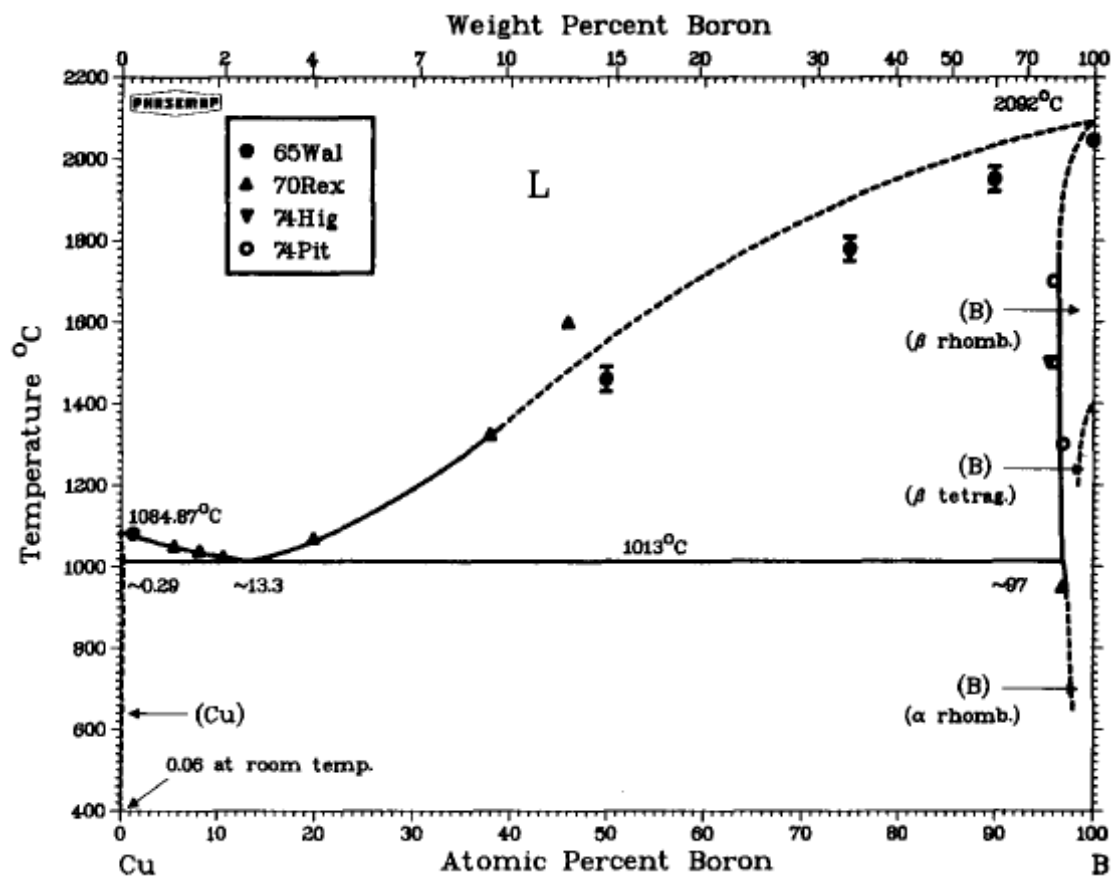


**Figure 3-25** Binary phase diagrams of Cu-B[63]
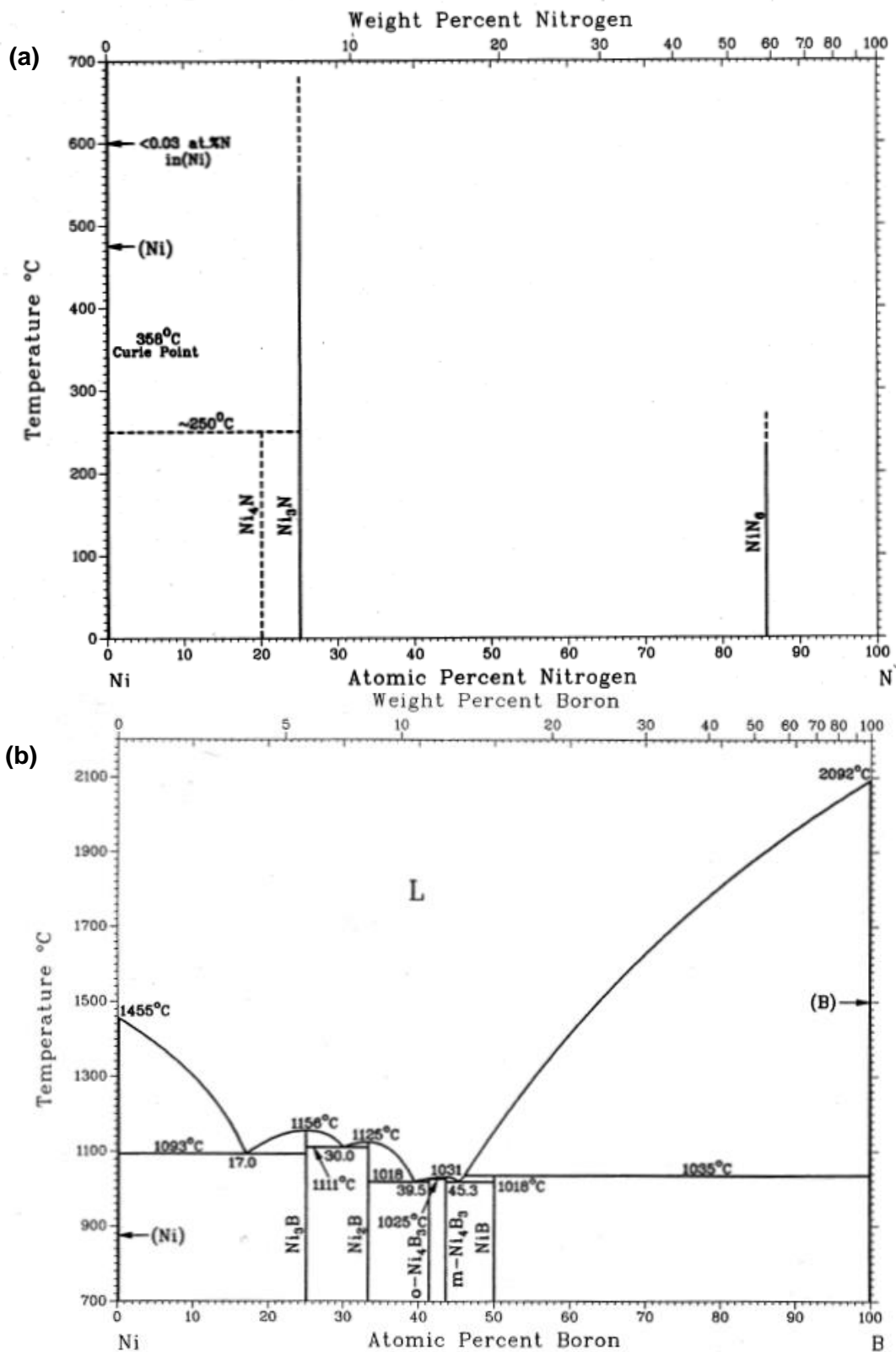
**Figure 3-26** Binary phase diagrams of Ni-N (a) and Ni-B (b).[63]
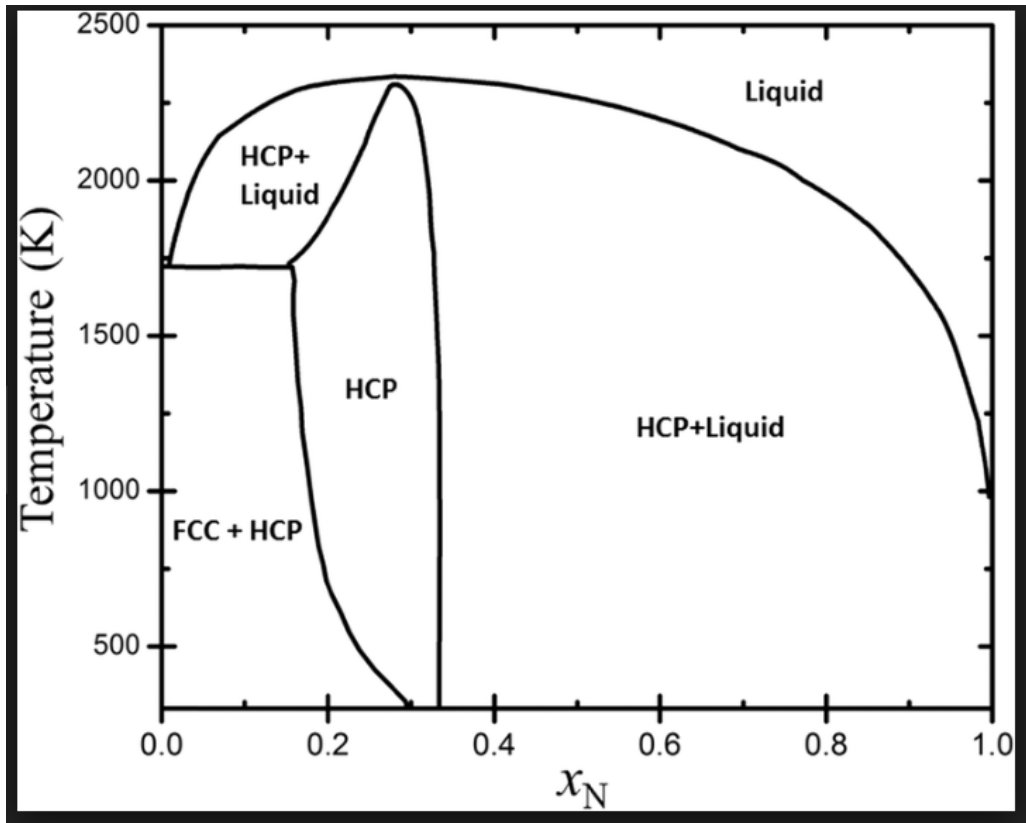
**Figure 3-27** Phase diagram of Ni-N at a wide temperature range.[64]

**(a)**

Weight Percent Nitrogen



**(b)**

Weight Percent Boron
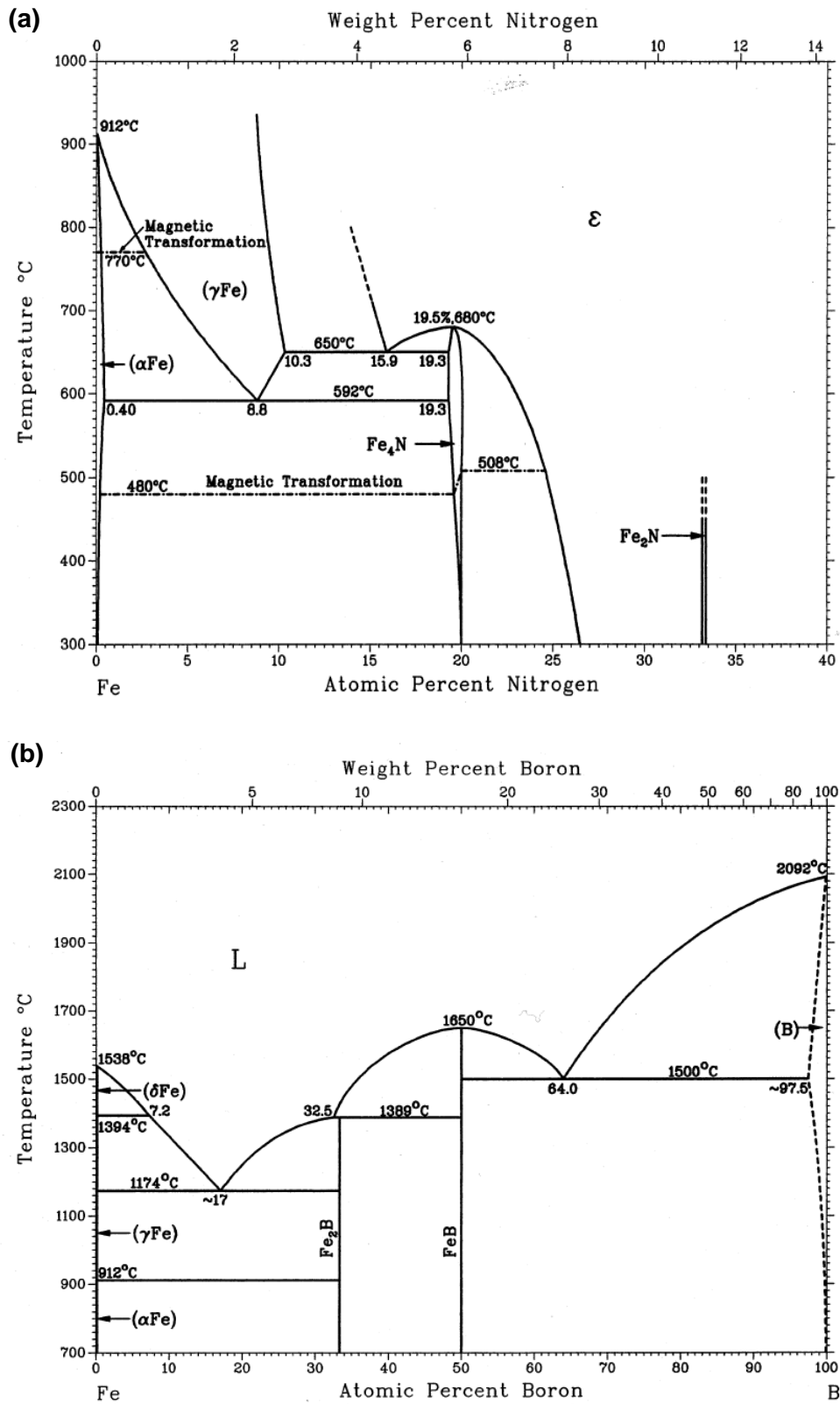


**Figure 3-28** Binary phase diagrams of Fe-N (a) and Fe-B (b).[63]
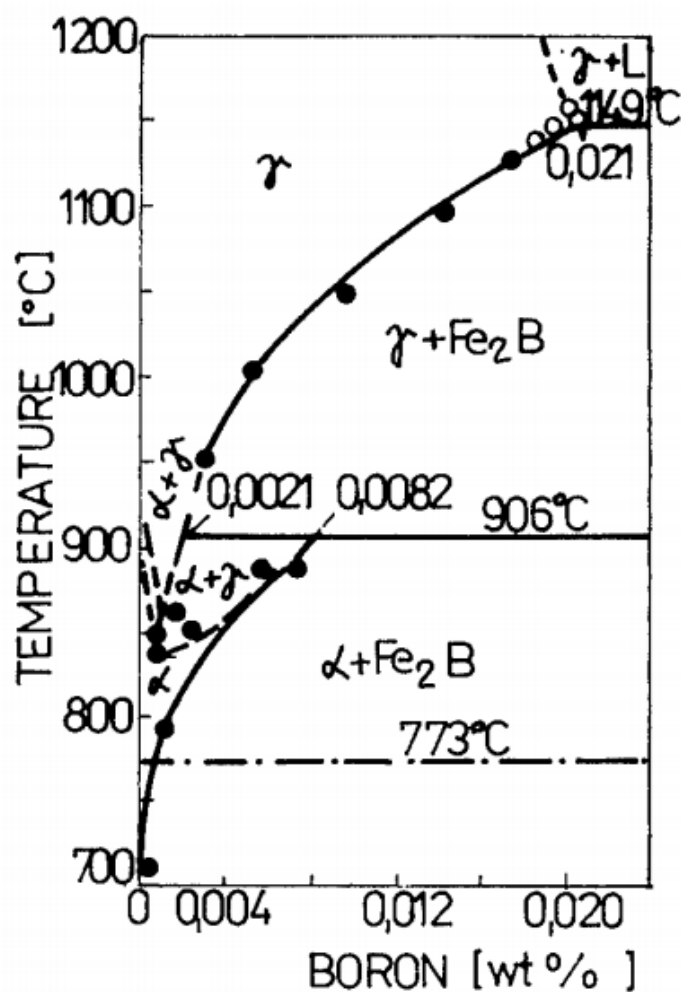
**Figure 3-29** Phase diagram of Ni-B with low boron concentrations.[66]

# References

1. Constantinescu, G., Kuc, A. and Heine, T. Stacking in bulk and bilayer hexagonal boron nitride. *Phys. Rev. Lett.* **111**, 036104 (2013).

2. Mirkarimi, P. B., McCarty, K. F. and Medlin, D. L. Review of advances in cubic boron nitride film synthesis. *Mater. Sci. Eng. R Rep.* **21**, 47–100 (1997).

3. Gorbachev, R. V. *et al.* Hunting for monolayer boron nitride: optical and Raman signatures. *Small* **7**, 465–468 (2011).

4. Sponza, L. *et al.* Direct and indirect excitons in boron nitride polymorphs: a story of atomic configuration and electronic correlation. *Phys. Rev. B* **98**, 125206 (2018).

5. Galvani, T. *et al.* Excitons in boron nitride single layer. *Phys. Rev. B* **94**, 125303 (2016).

6. Schué, L. *et al.* Dimensionality effects on the luminescence properties of hBN. *Nanoscale* **8**, 6986–6993 (2016).

7. Laturia, A., Put, M. L. V. de and Vandenberghe, W. G. Dielectric properties of hexagonal boron nitride and transition metal dichalcogenides: from monolayer to bulk. *npj 2D Mater. and Appl.* **2**, 6 (2018).

8. Hattori, Y., Taniguchi, T., Watanabe, K. and Nagashio, K. Anisotropic dielectric breakdown strength of single crystal hexagonal boron nitride. *ACS Appl. Mater. Interfaces* **8**, 27877–27884 (2016).

9. Hattori, Y., Taniguchi, T., Watanabe, K. and Nagashio, K. Layer-by-layer dielectric breakdown of hexagonal boron nitride. *ACS Nano* **9**, 916–921 (2015).

10. Lee, G.-H. *et al.* Electron tunneling through atomically flat and ultrathin hexagonal boron nitride. *Appl. Phys. Lett.* **99**, 243114 (2011).

11. Dean, C. R. *et al.* Boron nitride substrates for high-quality graphene electronics. *Nat. Nanotechnol.* **5**, 722–726 (2010).

12. Banszerus, L. *et al.* Identifying suitable substrates for high-quality graphene-based heterostructures. *2D Mater.* **4**, 025030 (2017).

13. Xue, J. *et al.* Scanning tunnelling microscopy and spectroscopy of ultra-flat graphene on hexagonal boron nitride. *Nat. Mater.* **10**, 282–285 (2011).

14. Burson, K. M. *et al.* Direct imaging of charged impurity density in common graphene substrates. *Nano Lett.* **13**, 3576–3580 (2013).

15. Perebeinos, V. and Avouris, P. Inelastic scattering and current saturation in graphene. *Phys. Rev. B* **81**, 195442 (2010).

16. Fischetti, M. V., Neumayer, D. A. and Cartier, E. A. Effective electron mobility in Si inversion layers in metal–oxide–semiconductor systems with a high-κ insulator: the role of remote phonon scattering. *J. Appl. Phys.* **90**, 4587–4608 (2001).

17. Ma, N. and Jena, D. Charge scattering and mobility in atomically thin semiconductors. *Phys. Rev. X* **4**, 011043 (2014).

18. Wang, L., Pu, Y., Soh, A. K., Shi, Y. and Liu, S. Layers dependent dielectric properties of two dimensional hexagonal boron nitridenanosheets. *AIP Adv.* **6**, 125126 (2016).

19. Li, L. H., Cervenka, J., Watanabe, K., Taniguchi, T. and Chen, Y. Strong oxidation resistance of atomically thin boron nitride nanosheets. *ACS Nano* **8**, 1457–1462 (2014).

20. Zhao, Y., Wu, X., Yang, J. and Cheng Zeng, X. Oxidation of a two-dimensional hexagonal boron nitride monolayer: a first-principles study. *Phys. Chem. Chem. Phys.* **14**, 5545–5550 (2012).

21. An, W., Wu, X., Yang, J. L. and Zeng, X. C. Adsorption and surface reactivity on single-walled boron nitride nanotubes containing stone−wales defects. *J. Phys. Chem. C* **111**, 14105–14112 (2007).

22. Si, M. S. and Xue, D. S. Oxidation fracturing of the graphitic BN sheet. *J. Phys. Chem. Solids* **71**, 1221–1224 (2010).

23. Liu, Z. *et al.* Ultrathin high-temperature oxidation-resistant coatings of hexagonal boron nitride. *Nat. Commun.* **4**, 2541 (2013).

24. Huang, Y. *et al.* Reliable exfoliation of large-area high-quality flakes of graphene and other two-dimensional materials. *ACS Nano* **9**, 10612–10620 (2015).

25. Wang, L. *et al.* One-dimensional electrical contact to a two-dimensional material. *Science* **342**, 614–617 (2013).

26. Masubuchi, S. *et al.* Autonomous robotic searching and assembly of two-dimensional crystals to build van der Waals superlattices. *Nat. Commun.* **9**, 1413 (2018).

27. Nicolosi, V., Chhowalla, M., Kanatzidis, M. G., Strano, M. S. and Coleman, J. N. Liquid exfoliation of layered materials. *Science* **340**, 1226419 (2013).

28. Yang, H. *et al.* Dielectric nanosheets made by liquid-phase exfoliation in water and

their use in graphene-based electronics. *2D Mater.* **1**, 011012 (2014).

29. Lee, D. *et al.* Scalable exfoliation process for highly soluble boron nitride nanoplatelets by hydroxide-assisted ball milling. *Nano Lett.* **15**, 1238–1244 (2015).

30. Kelly, A. G. *et al.* All-printed thin-film transistors from networks of liquid-exfoliated nanosheets. *Science* **356**, 69–73 (2017).

31. McManus, D. *et al.* Water-based and biocompatible 2D crystal inks for all-inkjet-printed heterostructures. *Nat. Nanotechnol.* **12**, 343–350 (2017).

32. Watanabe, K. and Taniguchi, T. Hexagonal boron nitride as a new ultraviolet luminescent material and its application. *Int. J. Appl. Ceram. Technol.* **8**, 977–989 (2011).

33. Kubota, Y., Watanabe, K., Tsuda, O. and Taniguchi, T. Deep ultraviolet light-emitting hexagonal boron nitride synthesized at atmospheric pressure. *Science* **317**, 932–934 (2007).

34. Kubota, Y., Watanabe, K., Tsuda, O. and Taniguchi, T. Hexagonal boron nitride single crystal growth at atmospheric pressure using Ni−Cr solvent. *Chem. Mater.* **20**, 1661–1663 (2008).

35. Meng, J. *et al.* Aligned growth of millimeter-size hexagonal boron nitride single-crystal domains on epitaxial nickel thin film. *Small* **13**, 1604179 (2017).

36. Xu, Z. *et al.* Large-area growth of multi-layer hexagonal boron nitride on polished cobalt foils by plasma-assisted molecular beam epitaxy. *Sci. Rep.* **7**, 43100 (2017).

37. Frueh, S. *et al.* Pyrolytic decomposition of ammonia borane to boron nitride. *Inorg. Chem.* **50**, 783–792 (2011).

38. Tay, R. Y. *et al.* Direct growth of nanocrystalline hexagonal boron nitride films on dielectric substrates. *Appl. Phys. Lett.* **106**, 101901 (2015).

39. Stehle, Y. *et al.* Synthesis of hexagonal boron nitride monolayer: control of nucleation and crystal morphology. *Chem. Mater.* **27**, 8041–8047 (2015).

40. Fu, L. *et al.* Direct growth of MoS$_2$/h-BN heterostructures via a sulfide-resistant alloy. *ACS Nano* **10**, 2063–2070 (2016).

41. Lu, G. *et al.* Synthesis of large single-crystal hexagonal boron nitride grains on Cu–Ni alloy. *Nat. Commun.* **6**, 6160 (2015).

42. Dean, C. R. *et al.* Hofstadter's butterfly and the fractal quantum Hall effect in moiré superlattices. *Nature* **497**, 598–602 (2013).

43. Ribeiro-Palau, R. *et al.* Twistable electronics with dynamically rotatable heterostructures. *Science* **361**, 690–693 (2018).

44. Yankowitz, M. *et al.* Dynamic band-structure tuning of graphene moiré superlattices with pressure. *Nature* **557**, 404 (2018).

45. Laskowski, R., Blaha, P. and Schwarz, K. Bonding of hexagonal BN to transition metal surfaces: an ab initio density-functional theory study. *Phys. Rev. B* **78**, 045409 (2008).

46. Wood, G. E. *et al.* van der Waals epitaxy of monolayer hexagonal boron nitride on copper foil: growth, crystallography and electronic band structure. *2D Mater.* **2**, 025003 (2015).

47. Kidambi, P. R. *et al.* In situ observations during chemical vapor deposition of hexagonal boron nitride on polycrystalline copper. *Chem. Mater.* **26**, 6380–6392 (2014).

48. Jang, S. K., Youn, J., Song, Y. J. and Lee, S. Synthesis and characterization of hexagonal boron nitride as a gate dielectric. *Sci. Rep.* **6**, 30449 (2016).

49. Koepke, J. C. *et al.* Role of pressure in the growth of hexagonal boron nitride thin films from ammonia-borane. *Chem. Mater.* **28**, 4169–4179 (2016).

50. Lin, W.-H. *et al.* Atomic-scale structural and chemical characterization of hexagonal boron nitride layers synthesized at the wafer-scale with monolayer thickness Control. *Chem. Mater.* **29**, 4700–4707 (2017).

51. Kim, S. M. *et al.* Synthesis of large-area multilayer hexagonal boron nitride for high material performance. *Nat. Commun.* **6**, 8662 (2015).

52. Caneva, S. *et al.* Controlling catalyst bulk reservoir effects for monolayer hexagonal boron nitride CVD. *Nano Lett.* **16**, 1250–1261 (2016).

53. Mayer, E. Symmetrical cleavage of diborane by ammonia in solution. *Inorg. Chem.* **11**, 866–869 (1972).

54. Baitalow, F., Baumann, J., Wolf, G., Jaenicke-Rößler, K. and Leitner, G. Thermal decomposition of B–N–H compounds investigated by using combined thermoanalytical methods. *Therm. Acta* **391**, 159–168 (2002).

55. Sutter, P., Lahiri, J., Albrecht, P. and Sutter, E. Chemical vapor deposition and etching of high-quality monolayer hexagonal boron nitride films. *ACS Nano* **5**, 7303–7309 (2011).

56. Joshi, S. *et al.* Boron nitride on Cu(111): an electronically corrugated monolayer. *Nano Lett.* **12**, 5821–5828 (2012).

57. Roth, S., Matsui, F., Greber, T. and Osterwalder, J. Chemical vapor deposition and characterization of aligned and incommensurate graphene/hexagonal boron nitride heterostack on Cu(111). *Nano Lett.* **13**, 2668–2675 (2013).

58. Gibb, A. L. *et al.* Atomic resolution imaging of grain boundary defects in monolayer chemical vapor deposition-grown hexagonal boron nitride. *J. Am. Chem. Soc.* **135**, 6758–6761 (2013).

59. Gomez-Aleixandre, C., Diaz, D., Orgaz, F. and Albella, J. M. Reaction of diborane and ammonia gas mixtures in a chemical vapor deposition hot-wall reactor. *J. Phys. Chem.* **97**, 11043–11046 (1993).

60. Ismach, A. *et al.* Toward the controlled synthesis of hexagonal boron nitride films. *ACS Nano* **6**, 6378–6385 (2012).

61. Murota, J. and Sakuraba, M. Handbook of 21st Century Film Preparation and

Application. NTS 340-349 (2003). (Japanese book)

62. Uwaha, M. Dynamics of crystal growth and pattern formation. BAIFUKAN (2008). (Japanese book)

63. Massalski, T. B., Okamoto, H., Subramanian, P. R. and Kacprzak, L. Binary alloy phase diagrams, 2nd edition. ASM international (1990).

64. Gage, S. H., Trewyn B. G., Ciobanu, C. V., Pylypenko, S. and Richards, R. M. Synthetic advancements and catalytic applications of nickel nitride. *Catal. Sci. Technol.* **6**, 4059-4076 (2016).

65. Suzuki, S., Pallares, R. M. and Hibino, H. Growth of atomically thin hexagonal boron nitride films by diffusion through a metal film and precipitation. *J. Phys. D Appl. Phys*. **45**, 385304 (2012).

66. Dudrová, E., Selecká, M., Burea, R. and Kabátová M. Effect of Boron Addition on Microstructure and Properties of Sintered Fe-1.5Mo Powder Materials. *ISIJ int.* **37**, 59-64 (1997).

# Chapter 4

# Epitaxial CVD growth of monolayer h-BN on Cu(111)/sapphire substrate

(Part of this chapter is published in *Phys. Chem. Chem. Phys.***19**, 8230-8235 (2017))

## 4.1   Introduction

To date, most of the previous studies on stacked 2D-layered devices have used exfoliated h-BN flakes as an insulating material,[1–5] because exfoliation is a simple and facile method to obtain high-quality h-BN flakes from bulk crystals.[6] However, it presents some disadvantages, including the limited size and inhomogeneous thickness of the obtained h-BN flakes, rendering the exfoliation method unsuitable for practical applications.

CVD has been developed to produce h-BN sheets in large area at relatively low cost.[7,8] As described in Chapter 3, in the CVD growth of h-BN a transition metal substrate is used as a catalyst to promote the decomposition of the source gas and the subsequent growth of h-BN atomic sheets. Although most previous works have used polycrystalline metal substrates, mainly Cu foil,[7–14] Ni foil[15–17], and Pt foil,[18,19] these substrates have surfaces with different orientations of metal grains. Consequently, a h-BN film grown on polycrystalline metal substrate consists of a number of h-BN grains with different orientations and even different thicknesses, resulting in polycrystalline h-BN films composed of poorly connected

small h-BN grains. Therefore, the control of both the crystallinity and the crystalline orientation of the metal substrate is essential for the growth of high-quality h-BN films. Thus, single-crystal metal surfaces, such as Co(0001),[20] Ni(111),[21,22] Rh(111),[23] Ir(111),[24] Pt(111)[23,25] and Cu(111),[26–28] have been employed to grow monolayer h-BN. These single-crystalline substrates enable the alignment of the h-BN sheet whose lattice orientation is registered by the underlying metal substrate. However, these single-crystalline metal substrates are very expensive and their sizes are limited to a small scale. Such expensive metal substrates make transfer of h-BN films using a metal etching process inefficient, thus hindering many practical applications, such as large-scale 2D electric and photonic devices. The electrochemical transfer has been also used for the transfer instead of chemical etching of a catalyst, but bubbles formed at the h-BN/metal interface damages the as-grown h-BN, deteriorating the quality of the transferred h-BN. Therefore, a highly crystalline but cost-effective metal catalyst is required for the development of large-area h-BN research.

In this Chapter, the synthesis of a large-area h-BN sheet on thin (~1 $\mu$m) Cu(111) films epitaxially deposited on c-plane (0001) sapphire substrates is reported. Sapphire substrates have become larger and cheaper owing to recent development of light-emitting diodes (LEDs), in which gallium nitride (GaN) is deposited on sapphire by a metal organic CVD (MOCVD) method. The cost effective sapphire substrate and thin Cu(111) film allow to transfer as-grown films to other substrates, such as $SiO_2$/Si, routinely for characterization of h-BN as well as post-growth device fabrication. By using the Cu/sapphire substrate, I have achieved the epitaxial growth of monolayer h-BN in large area, for which the orientation of the hexagon lattice of the h-BN is well controlled

by the Cu(111) lattice.[29] Triangular hBN grains oriented in two definite directions with respect to the Cu(111) thin film were observed. The controlled orientation of the hexagonal lattice was confirmed for a uniform sheet of monolayer h-BN by low-energy electron diffraction (LEED) measurement.

## 4.2 Experimental methods

### 4.2.1 Preparation of heteroepitaxial Cu(111) film and CVD growth of h-BN

Crystalline Cu(111) films with a thickness of ~1 $\mu$m were deposited by radio-frequency (RF) sputtering on c-plane sapphire substrates at 220 °C. The Cu/sapphire was subjected to ambient-pressure CVD using the setup illustrated in Figure 4-1. The substrate was first annealed in a mixed flow of $H_2$ and Ar at 1000 °C for one hour to improve the crystallinity and surface flatness of the Cu film. After elevating the furnace temperature to 1050 °C, ammonia borane ($BH_3NH_3$) vapor was introduced to the quartz tube to grow h-BN on the Cu surface under a $H_2$-Ar mixed flow. The ammonia borane vessel was heated at ~115 °C prior to the introduction to the main chamber while passing Ar gas through the vessel to exhaust. Thus, the ammonia borane vapor can be introduced immediately after reaching the target temperature by changing the gas flow using the gas switch valve. After the reaction was completed, the substrate was moved away from the heating zone to rapidly quench the growth.
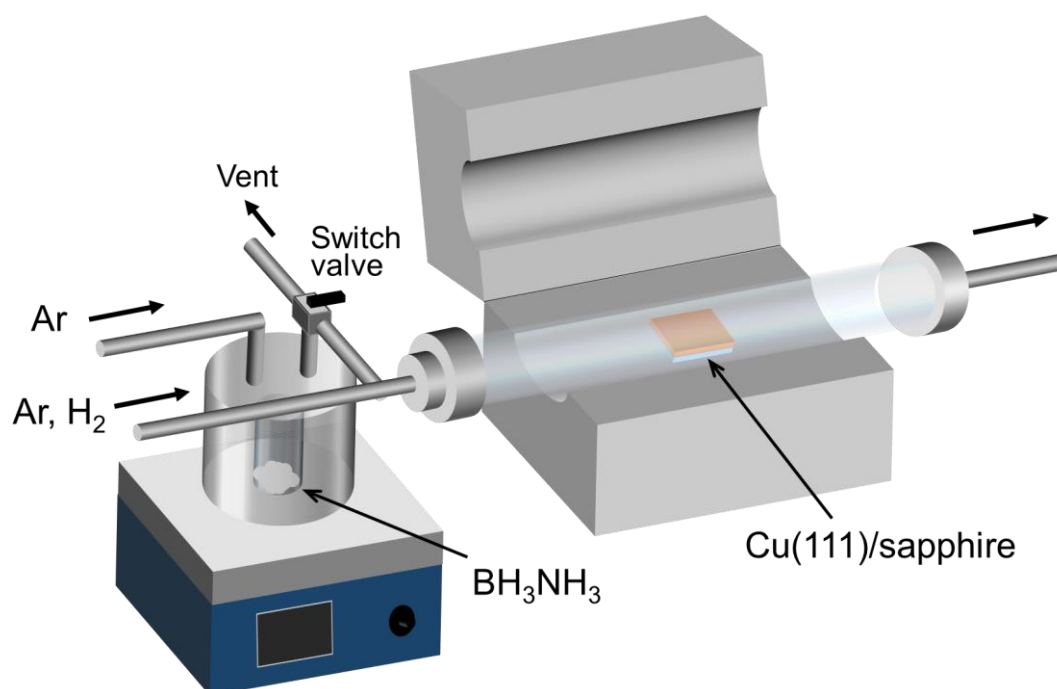
**Figure 4-1** Schematic illustration of the CVD setup used for the h-BN growth.

## 4.2.2   Characterization of h-BN

After the CVD growth, the as-grown h-BN was transferred onto a $SiO_2$/Si substrate using poly(methyl methacrylate) (PMMA) and an ammonium persulfate (APS) aqueous solution for further investigations.[30] Surface structure and film morphology were measured by scanning electron microscopy (SEM, Hitachi S-4800) and atomic force microscopy (AFM, Bruker, Nanoscape V). Raman spectra were collected using a confocal Raman spectrometer (Nanofinder 30, Tokyo Instruments) with a 532 nm laser excitation. LEED was measured for as-grown h-BN/Cu(111) in an ultrahigh vacuum chamber at $8 \times 10^{-9}$ Pa using a BDL600IR

spectrometer (OCI, Canada). X-ray photoelectron spectroscopy (XPS) was performed using a Kratos Axis 165 spectrometer with a monochromatic Al X-ray source. The atomic ratio of B and N atoms was determined from the peak intensities with the correction of sensitivity factor of each element.

## 4.2.3   Fabrication of stacked graphene/h-BN heterostructures and graphene transistors

The vertically stacked graphene/h-BN heterostructure was prepared by transferring monolayer h-BN from Cu(111) on SiO2/Si substrate (SiO$_2$ thickness is 300 nm), followed by transferring monolayer graphene on to the h-BN/Cu(111). The monolayer graphene was also grown on Cu(111)/sapphire substrate by thermal CVD method using methane as feedstock.[30] PMMA and thermal release tape (TRP) were used to transfer both h-BN and graphene.

For making graphene transistors, the graphene was first covered with photoresist (name), followed by photolithography. After developing, exposed areas were etched by O$_2$ plasma treatment. The remaining resist was removed by immersion into acetone. In the next step, the electrode patterns were also made by photolithography and Au electrodes (50 nm thickness) were deposited by thermal evaporation. The channel length and width of the graphene field-effect transistors (FETs) are 50 $\mu$m and 10 $\mu$m, respectively.

The transfer properties of the graphene FETs were measured in vacuum at room temperature using the probe station and Agilent B1500A source-measure unit. Prior to the measurement, the substrate was annealed in vacuum at 200 °C for 2 hours to remove

surface adsorbates, such as oxygen, water, and polymer residues.

## 4.3  Results and discussion

### 4.3.1  Epitaxial growth of monolayer h-BN

The ambient-pressure CVD was performed using a Cu(111)/sapphire substrate. Figure 4-2a-c shows SEM images of as-grown h-BN on Cu(111) surface taken for different growth times. After 5 min of reaction, triangular grains of h-BN with a size of 1~5 $\mu$m were formed, as seen by a bright contrast in Figure 4-2a. The dark contrast corresponds to the bare Cu(111) surface. The triangular shape indicates the formation of single-crystalline h-BN grains. It is also seen that these triangular h-BN grains are aligned along two main directions (colored in Figure 4-2a). The angle distribution of these h-BN grains is presented in Figure 4-2d. Single-crystalline grains are well aligned with a relative orientation of their edges of 0 ± 5° within an interval of 60°. The populations of the two orientations, highlighted in red and blue in Figure 2a, are almost the same, which will be discussed later. The existence of these two preferred orientations strongly suggests an epitaxial growth of the h-BN on the Cu(111) surface. An AFM image of the triangular grains after the transfer on $SiO_2$ is shown in Figure 4-2e. The measured height is about 0.8 nm, suggesting the growth of monolayer h-BN (Figure 4-2f). The nonuniformity of the AFM height inside h-BN grains can be attributed to the PMMA residue and/or the imperfect transfer of h-BN.As seen in Figure 4-2a-c, the lateral size of the h-BN grains increased with increasing the

growth time. After 15 min reaction, h-BN grains were found to completely cover the Cu surface and form a uniform h-BN sheet (Figure 4-2c) .
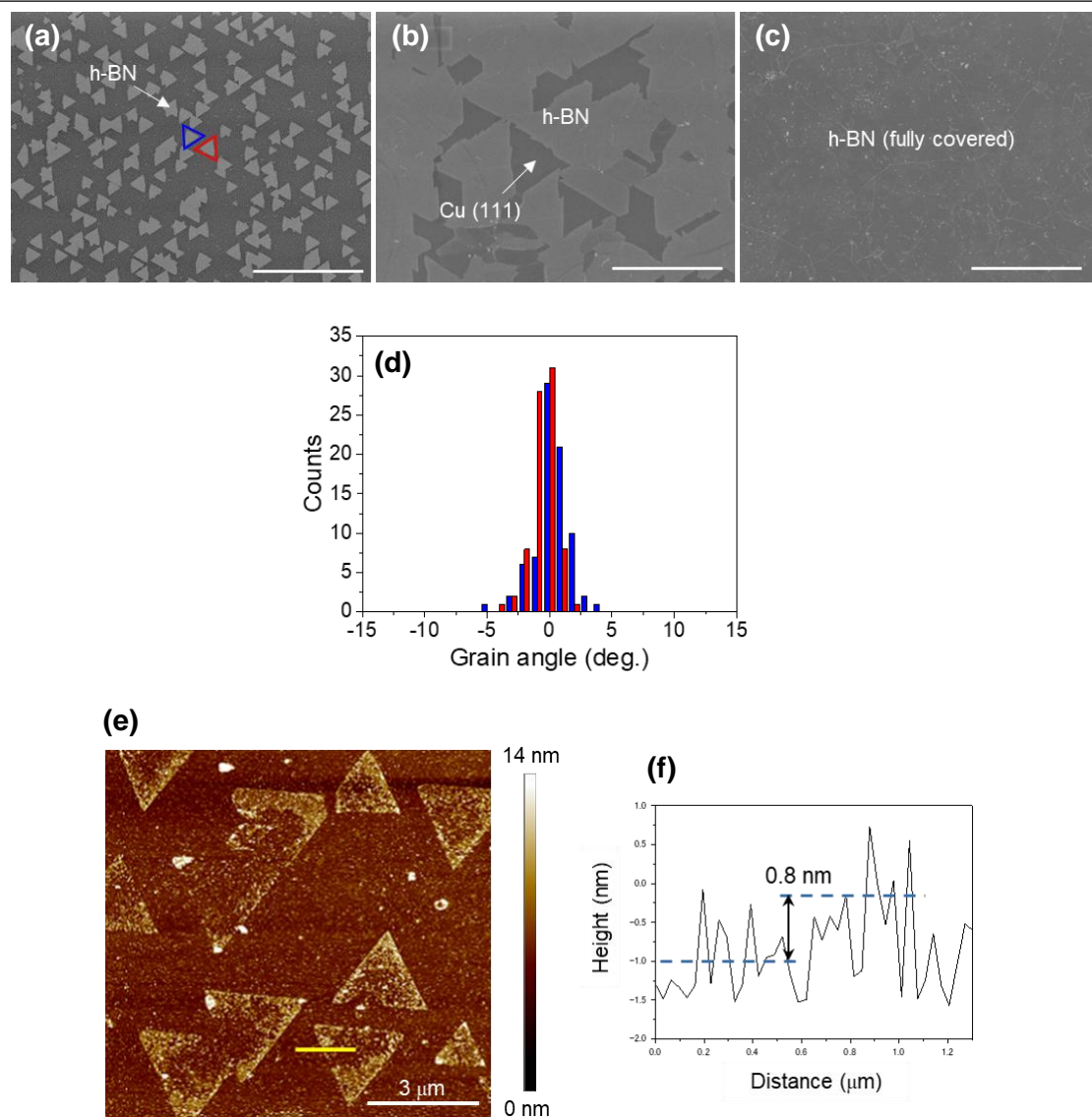


**Figure 4-2** SEM images of h-BN grown on Cu(111) films at growth time of 5 min (a), 10 min (b) and 15 min (c). All scale bars are 20 $\mu$m. (d) Distribution of the orientation of h-BN grains on Cu(111) for the 5 min reaction. The colors represent the two orientations shown in (a). (e) AFM image of triangular h-BN grains transferred on a SiO$_2$ substrate. (f) Height profile of a h-BN grain measured along the yellow line shown in (e).

The relatively uniform SEM contrast seen in Figure 4-2c indicates the absence of multilayer grains. This result implies that h-BN grows preferentially on the Cu surface rather than on the h-BN surface, because h-BN cannot catalyze the decomposition of the precursor molecules. Thus, the h-BN growth is supposed to occur based on a self-limiting process, as was observed in the growth of monolayer graphene on Cu surface.[31]

### 4.3.2  LEED measurements

LEED was performed for the fully covered h-BN sheet, as shown in Figure 4-3a. The spot size of the electron beam is about 1 mm so that we can measure the macroscopic orientation of the h-BN sheet with respect to the underlying Cu(111) lattice. Six hexagonally arranged diffraction spots were clearly observed for the h-BN/Cu(111) sample (diffraction patterns measured with different electron energies are shown in Figure 4-2c). It is noted that such clear diffraction pattern was not observed for a bare Cu(111) substrate without growing h-BN, because Cu surface is easily oxidized due to air exposure during the transport to the LEED chamber. This fact indicates that the h-BN acts as an excellent gas barrier film, protecting the metallic Cu(111) surface from oxidation. From the above observation it is speculated the observed hexagonal diffraction pattern is originated in both h-BN and Cu(111) lattices. As shown by white arrows in Figure 4-3a, three diffraction spots are slightly brighter than other three spots. These bright spots can be ascribed to three-fold rotational symmetry of fcc(111) plane of the Cu single crystal, confirming that the observed six diffraction spots are coming from both h-BN and

**(a)**



**(b)**

**(c)**
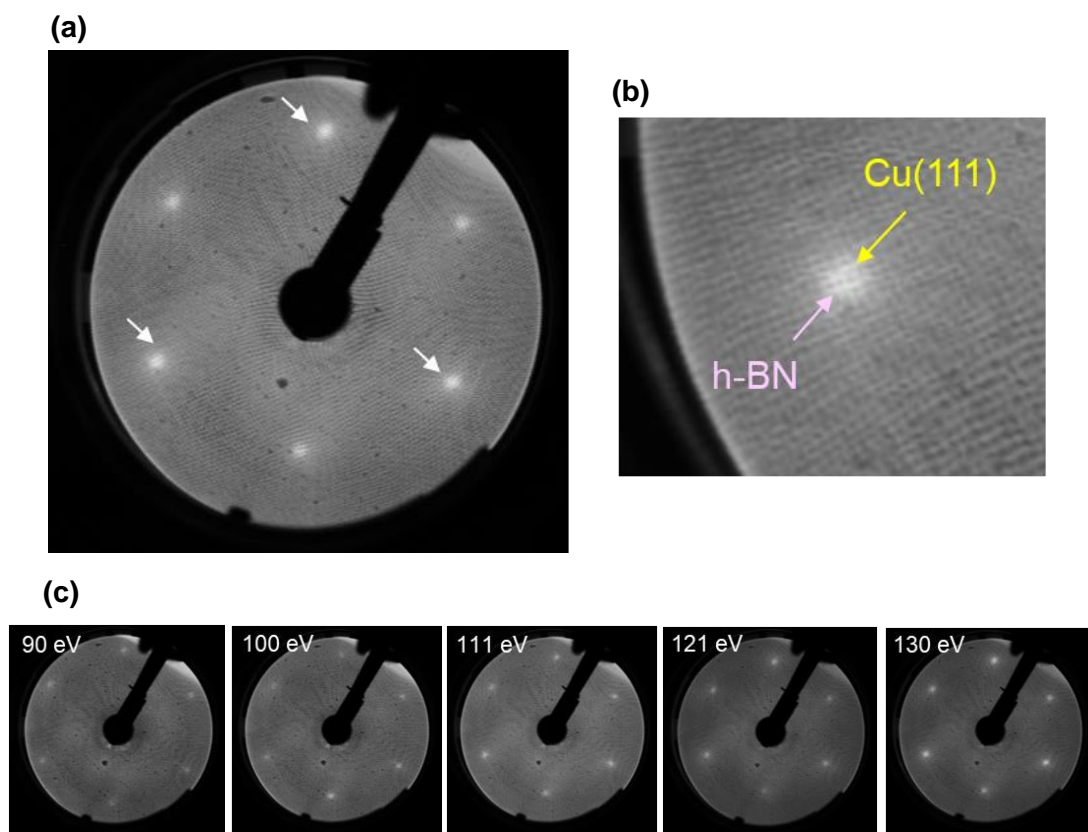
**Figure 4-3** (a) LEED pattern measured for the fully covered h-BN sheet. Electron energy is 130 eV. The three white arrows point to the brighter diffraction spots. (b) Magnified image of one of the diffraction spots. (c) LEED patterns collected with different electron energies.

Cu(111). The clear diffraction pattern seen in Figure 4-3a indicates that h-BN sheet is highly oriented due to the Cu(111) lattice realized by c-plane sapphire substrate.

Figure 4-3b shows an enlarged image of one of the diffraction spots. The spot is slightly elongated in the radial direction, which can be interpreted as an overlap of the diffractions from the h-BN and Cu lattices. As the lattice constants of h-BN and Cu are very close to each other (h-BN: 0.251 nm, Cu: 0.256 nm) and the
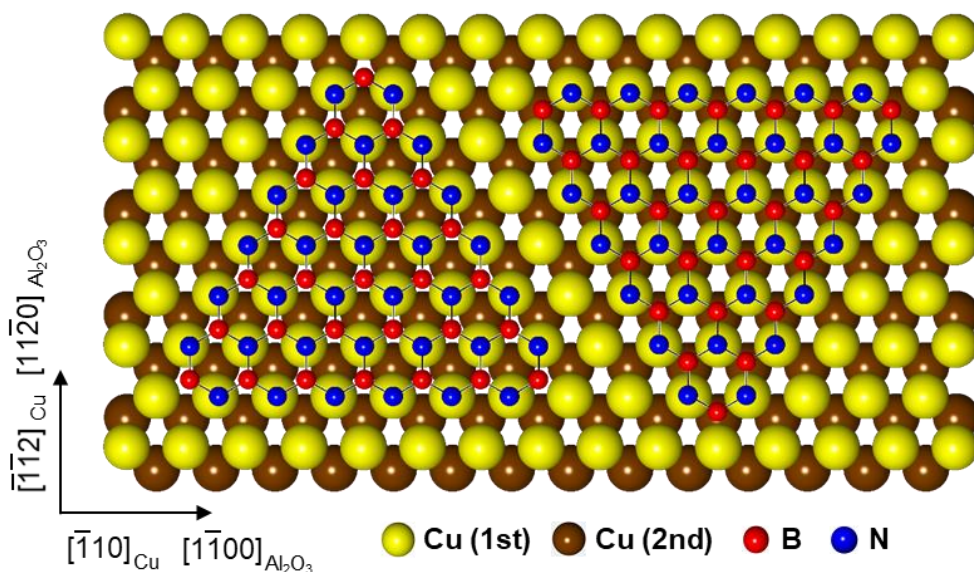
**Figure 4-4** Atomic model of triangular grains of h-BN on Cu(111). Left and right configurations correspond to ($N_{top}$,$B_{fcc}$) and ($N_{top}$,$B_{hcp}$), respectively. The orientations of c-plane sapphire and Cu are indicated by arrows.

diffraction spots are slightly faint, it was difficult to clearly resolve these two diffraction spots.

Figure 4-4 illustrates the atomic model of triangular h-BN grains oriented in two directions with respect to the Cu(111) lattice. The orientations are determined based on SEM and LEED observations. A previous theoretical study suggests that in a triangular h-BN grain, N-terminated edges are more energetically stable than B-terminated ones.[32] According to density functional theory (DFT) calculations, it is energetically stable for N atoms to locate over the top Cu atoms.[33] Given these constrains, there are two possible orientations for the h-BN grains, as shown in Figure 4-4. In the left of Figure 4-4, B atoms locate at face-centered cubic (fcc) position (denoted as $N_{top}$,$B_{fcc}$), while Figure 4-4 right shows B atoms locating at hexagonal closed pack (hcp) positions ($N_{top}$,$B_{hcp}$). DFT calculation suggests that ($N_{top}$,$B_{fcc}$) is more energetically stable than at ($N_{top}$,$B_{hcp}$) by 5

meV/BN on Cu(111) surface.[34] However, as the energy difference of these two configurations is very small, it is highly likely that both configurations appear during the high temperature CVD process (1050 ºC). Furthermore, a large h-BN grain will contain both configurations (i.e., ($N_{top}$,$B_{fcc}$) and ($N_{top}$,$B_{hcp}$)) within one grain due to the lattice mismatch. The preferential growth of h-BN in one direction was experimentally observed for h-BN grown on Ir(111) surface.[24] However, this was observed only under a specific growth condition, and not under a standard high temperature growth process.[24]

### 4.3.3   XPS and Raman measurements

The presence of both B and N atoms after the CVD was confirmed by XPS measurements. Figure 4-5a summarizes the XPS spectra of $B_{1s}$ and $N_{1s}$ core levels and the [B]:[N] atomic ratios determined from the relative intensity of these peaks. XPS spectra were measured for both the as-grown h-BN sheet on Cu(111) and after transfer on a $SiO_2$/Si substrate. The appearance of the $B_{1s}$ and $N_{1s}$ peaks in the as-grown h-BN evidences the presence of B and N in the sample, supporting the formation of h-BN. For the reliable calculation of [B]:[N] ratio, the B and N peaks were subjected to curve fitting before transfer, as shown in Figure 4-5b and Table 4-1, in order to eliminate the effect of $sp^3$-B component.[35] The peak is fitted with two Gaussian-Lorentzian mixed curves (Voigt function) which correspond to B atoms with $sp^2$ (~190.5 eV) and $sp^3$ (~191.1 eV) hybridized orbitals. The intensity of the $sp^2$ component was used to determine the [B]:[N] atomic ratio listed in Figure 4-5a, because only $sp^2$-B atoms contribute to the h-BN formation. The calculated atomic ratio ([B]:[N]=1:0.82) is close to the stoichiometric ratio expected for h-BN ([B]/[N] ratio is 1). This deviation indicates that the amount of B is slightly higher

**(a)**

| | B$_{1s}$ | N$_{1s}$ | [B]:[N] ratio |
|---|---|---|---|
| Cu(111) |  |  | 1 : 0.82 |
| SiO$_2$/Si |  |  | 1 : 1.13 |

**(b)**
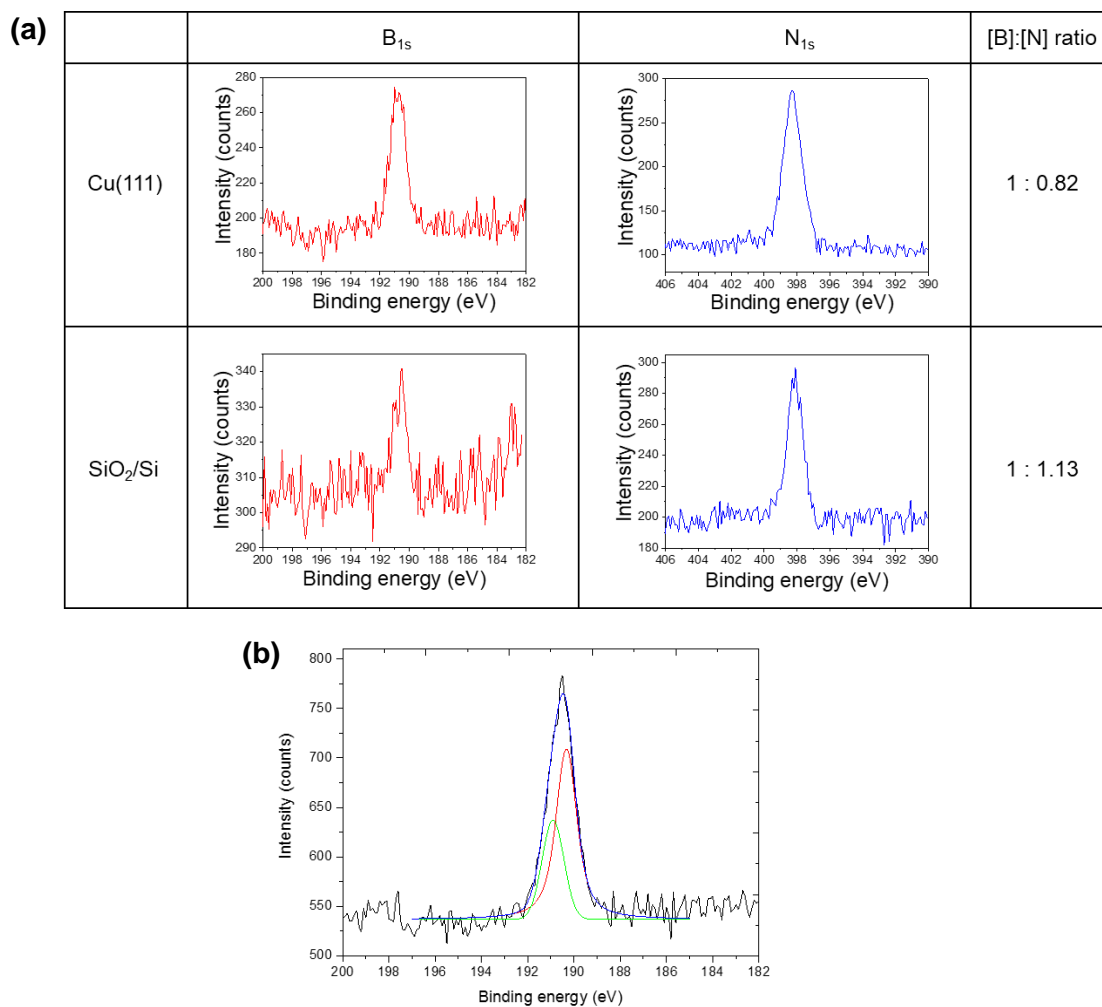


**Figure 4-5** (a) XPS B1s and N1s spectra measured for the as-grown (upper panel) and transferred (lower panel) h-BN sheets. The [B]:[N] ratio was determined from the relative peak intensity. (b) Fitted XPS B$_{1s}$ spectra of as-grown h-BN sheets.

**Table 4-1** Fitting parameter used in Figure 4-5b

| | Peak position (eV) | Percentage of peak area (%) |
|---|---|---|
| sp$^2$ | 190.3 | 69 |
| sp$^3$ | 190.9 | 31 |

than that of N in the as-grown h-BN/Cu(111) sample. It is noted that the solubility of B in Cu is relatively high (0.29 atom% at the CVD temperature, 1050 °C), while that of N is almost negligible.[36] Since the sample was rapidly cooled down to room temperature just after terminating the supply of ammonia borane, I consider that a certain amount B atoms remain in the subsurface of the Cu film, which was observed by $sp^3$-B peak. This probably results in the high observed B concentration. Even though XPS is a surface-sensitive technique, it is difficult for the atomically thin h-BN sheet to completely screen the signal originated in the substrate.

As shown in the lower panel of Figure 4-5a, the transferred h-BN sheet shows a reduced B concentration compared to that of the as-grown sample, supporting the speculation that B atoms detected in the as-grown sample is partly originated in the Cu substrate. The atomic ratio measured after the transfer, [B]:[N]=1:0.88, is closer to ideal stoichiometric ratio, but still slightly deviates from the stoichiometry. The weak B signal, which reduces signal-to-noise ratio may be one of the reasons of such discrepancy.

Figure 4-6a shows an AFM image of the transferred h-BN sheet. It is considered that the nanoparticles observed on the surface are mainly poly(aminoborane) and its dehydrogenated molecules, which were previously observed when ammonia borane was used as feedstock.[37] Similar to the CVD grown monolayer graphene,[30] wrinkles are also seen on the h-BN surface. It is likely that these wrinkles are formed during the growth and subsequent cooling down steps, because the as-grown h-BN on Cu(111) also showed clear wrinkles (Figure 4-6c). In the cooling down step, the Cu lattice shrinks much more than the

h-BN lattice due to different thermal expansion coefficients,[38] thus resulting in the wrinkles on the h-BN surface.

Raman spectroscopy was performed for the transferred h-BN sheet (red spectrum in Figure 4-6b). The $E_{2g}$ peak of h-BN was not observed, suggesting that h-BN sheet grown on Cu(111) is very thin. As indicated by AFM measurements, the h-BN is monolayer. Monolayer h-BN is known to show very weak Raman
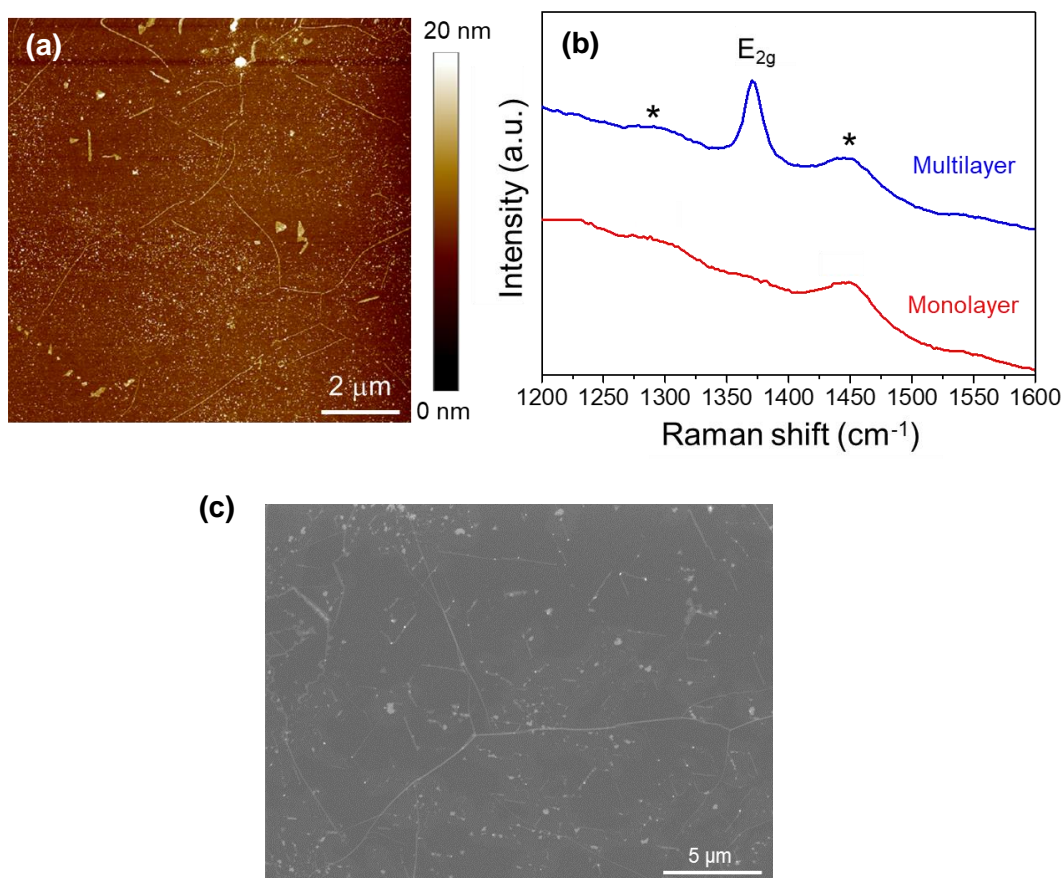


**Figure 4-6** (a) Optical microscope image of multilayer h-BN transferred on a SiO₂/Si substrate. (b) AFM image of the multilayer h-BN sheet. Here, monolayer or few-layer h-BN fully covers the Cu surface. (c) SEM image of as-grown h-BN film on Cu(111) surface.   Wrinkles are observed in the as-grown film.

signal,[20] sometimes below the detection limit, because of the lack of absorption of the excitation laser beam. Grown monolayer h-BN was also difficult to distinguish from the $SiO_2$ substrate surface using an optical microscope (see Figure 4-7a,b) due to low optical contrast. However, when the concentration of ammonia borane was increased during the CVD by about five times, the growth of non-uniform multilayer h-BN was observed, as presented in Figure. 4-7d. The thick multilayer h-BN grains showed a clear optical contrast as well as Raman $E_{2g}$ peak (blue spectrum of Figure 4-6b). It is interesting to note that the multilayer h-BN grains also show two specific orientations, as seen in Figure 4-7d. This suggests that multi-layer grains of h-BN are also grown epitaxially. Thus, the orientation of multilayer h-BN grains can be also controlled by using the epitaxial Cu(111) film.
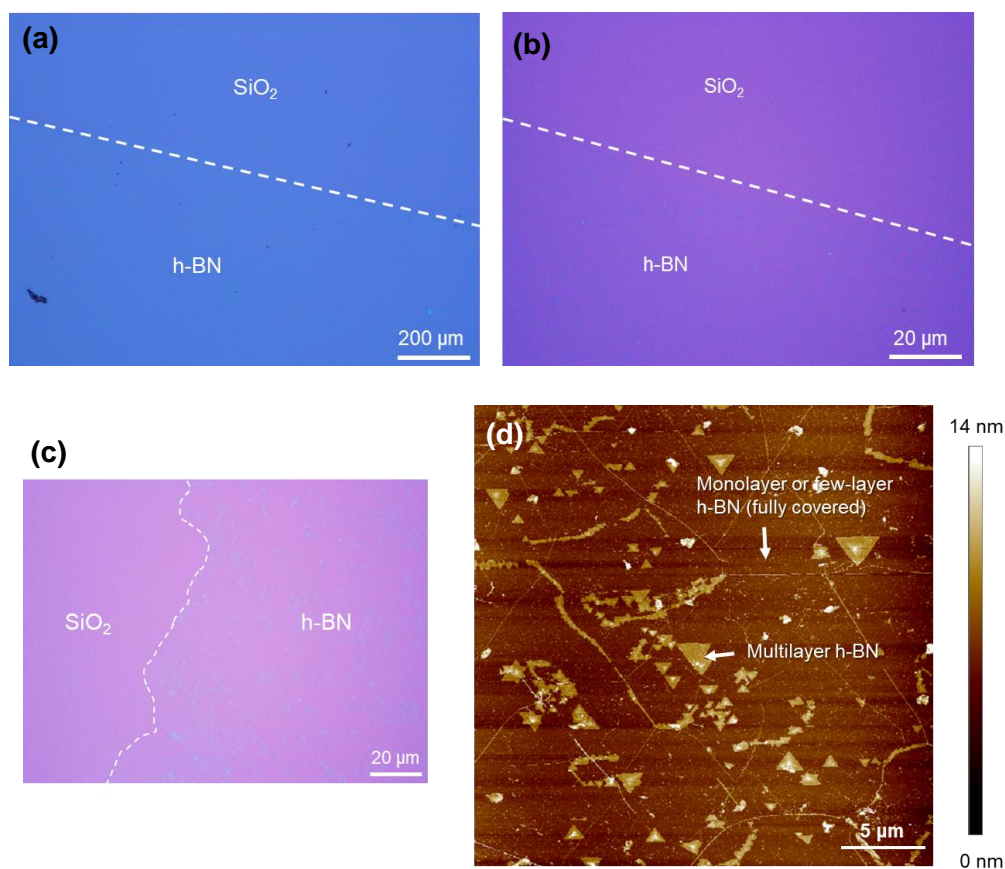
**Figure 4-7** (a,b) Optical micrograph of monolayer h-BN films which were transferred on SiO₂/Si substrates (SiO₂ thickness is 300 nm). (a) low and (b) high magnifications. Image (a) indicates that monolayer h-BN is difficult to be observed by an optical microscope. However, the edge was slightly recognized due to the presence of PMMA residue which was used to transfer the h-BN. (c) Optical microscope image of multilayer h-BN transferred on a SiO₂/Si substrate. (d) AFM image of the multilayer h-BN sheet. Here, monolayer or few-layer h-BN fully covers the Cu surface.

### 4.3.4 Growth mechanism of monolayer h-BN

In this section, the growth mechanism of monolayer h-BN on epitaxial Cu(111)/sapphire substrates is discussed based on the experimental observations. The feedstock, ammonia borane, sublimed by heating at 115 °C decomposes into

gaseous borazine ($B_3N_3H_3$), solid poly(aminoborane) ($BH_2NH_2$) and a small amount of diborane ($B_2H_6$).[39] These species, especially borazine, are carried into the chamber while experiencing further dehydrogenation at 77-627 °C.[40] Then, borazine derivatives are catalytically decomposed on the Cu(111) surface, leaving intermediates which diffuse on the Cu surface. At the same time, B atoms would dissolve into the bulk of the Cu, while little occurs for N atoms, as was suggested by XPS measurements (see Figure 4-5). Finally, h-BN nucleation occurs on the Cu(111) surface mainly via surface diffusion, which interacts with the Cu(111) to orient its hexagonal lattice.

The growth of multilayer h-BN observed in Figures 4-6a and 4-7d cannot be simply explained by the catalytic effect of the Cu thin film, as the Cu surface is covered with monolayer (or few-layer) h-BN (see Figure 4-6c). There are two possible mechanisms of the multilayer growth; (i) the second layer grows below the first layer due to segregation from the Cu bulk, and (ii) the second layer grows above the first layer due to non-catalytic decomposition of ammonia borane. In the former case, twin boundaries existing in the Cu(111) film[41] may increase the solubility of N atoms, resulting in the formation of multilayer h-BN due to segregation. In the latter case, as ammonia borane is much more reactive than $CH_4$ feedstock (ammonia borane suffers from thermal decomposition at high temperature forming borazine and poly(aminoborane)[39,42]), the self-decomposition can also occur during the CVD. Like the case seen in triangular $MoS_2$ grains grown on graphene,[43] where no catalytic effect is expected for the graphene substrate, the triangular h-BN grains may be formed due to epitaxial growth. Further study is necessary to understand the growth mechanism of multilayer h-BN on Cu catalyst.

## 4.3.5  Graphene FETs

To investigate effects of our monolayer h-BN on the graphene FETs, the back-gated graphene field-effect transistors (FETs) were fabricated with monolayer h-BN placed below graphene channel. The uniform graphene sheet was transferred onto the h-BN sheet which was also transferred from the Cu(111) catalyst., followed by photolithography and metal deposition For comparison, the standard graphene-on-SiO2 devices were also fabricated. Figure 4-8a and 4-8b show a schematic of the FET arrays and optical image of a graphene channel, respectively. Figure 4-8c,d indicates the transfer characteristics of the graphene FETs measured in vacuum and air.

In vacuum condition, the devices showed typical "V"-shaped curve widely observed in the graphene FETs. The Dirac point was shifted to positive value, indicating that the graphene is p-type doped probably due to PMMA residue and remaining adsorbates. When the FETs were measured in air, the doping from the adsorbates is significant, as seen in Figure 4-8d. The carrier mobility of the graphene FET was calculated based on the following equation.

$$\mu = \left(\frac{\partial I_d}{\partial V_g}\right)\frac{L}{WC_{ox}V_d} \tag{1}$$

$I_d$: Drain current
$V_g$: Gate voltage
$V_d$: Drain voltage
$W$: Channel width
$C_{ox}$: Capacitance of SiO$_2$ ($1.15 \times 10^{-4}$ F/m$^2$)

In vacuum condition, as shown in Figure 4-9, the average mobility of graphene and graphene/h-BN FETs were 3210 cm$^2$V$^{-1}$s$^{-1}$ and 1810 cm$^2$V$^{-1}$s$^{-1}$, respectively. In addition, the average position of the Dirac point was 24 V and 45 V for graphene and graphene/h-BN, respectively. Figure 4-9 shows that the hole mobility decreases with increasing the
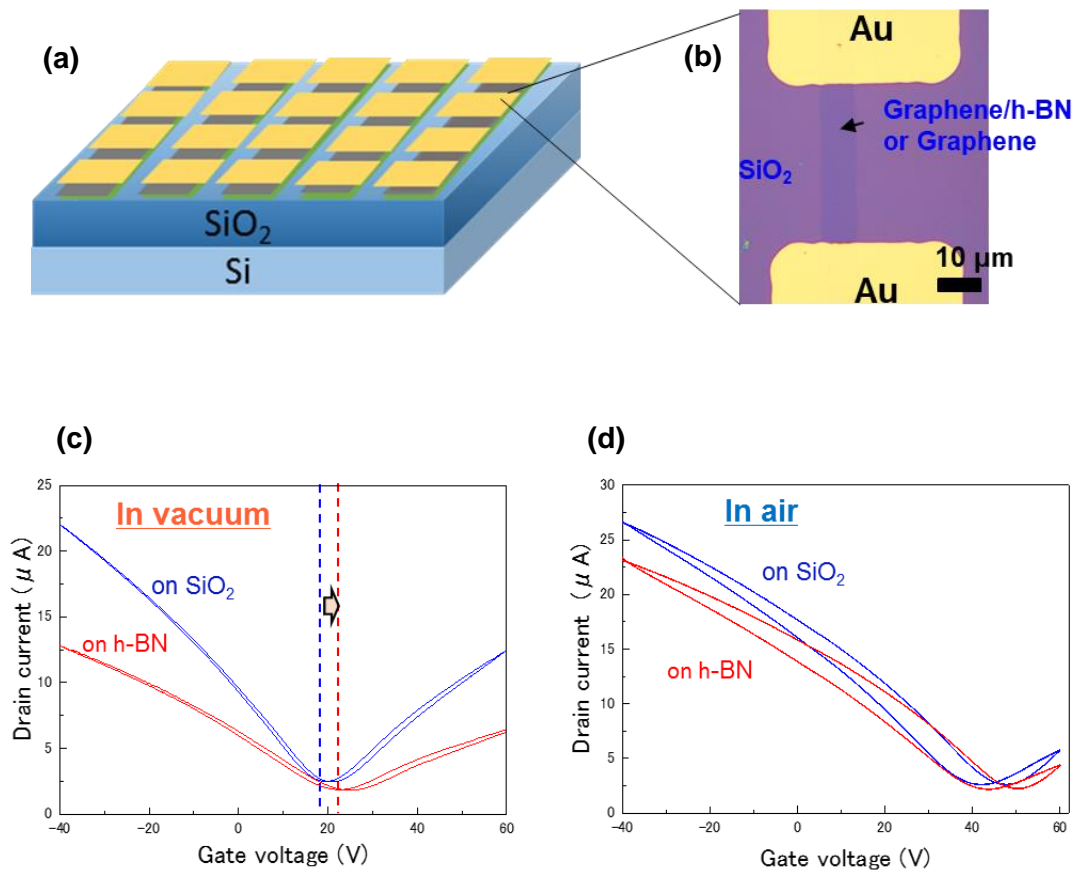
**Figure 4-8** Schematic of FET arrays (a) and an optical image of graphene channel (b). Transfer characteristics of graphene-FETs measured in vacuum (c) and in air (d).

Dirac point voltage.

The decrease of the average mobility and the more intense p-type doping were found for graphene/h-BN when compared with the graphene devices directly fabricated on $SiO_2$ substrate. The reduced mobility and higher doping can be ascribed to multiple transfers and insufficient thickness of monolayer h-BN. Multiple transfer can increase the amount of residual PMMA, because PMMA was used twice when graphene/h-BN devices were fabricated. The PMMA residues induces not only the p-type doping but also charge scattering due to the formation of charge trapping sites. Although h-BN flakes were used to screen out the influence of $SiO_2$ surface, the thickness of monolayer h-BN

may not be enough considering the long-range Coulomb interaction brought by the charge impurities and dangling bonds existing on the $SiO_2$ surface. The present result suggests that sufficient thickness of multilayer h-BN is required to realize the high carrier mobility and near-zero Dirac point for graphene FETs.
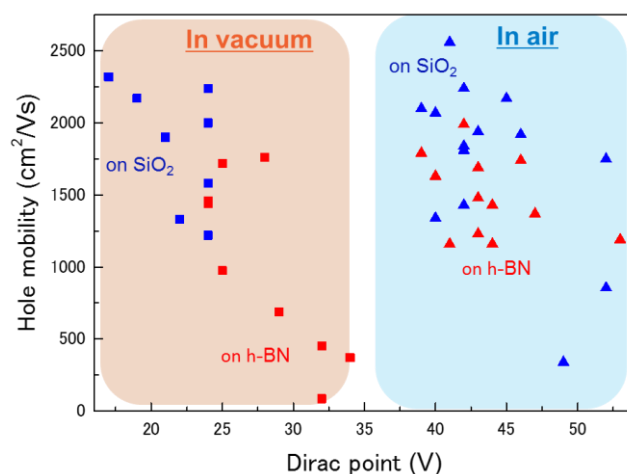


**Figure 4-9** Comparison of the hole mobility as function of the Dirac point measured in vacuum and air.

## 4.4 Conclusions

Monolayer h-BN was epitaxially grown by CVD on Cu(111) thin film deposited on c-plane sapphire substrates. The use of sapphire substrate realizes a large-scale synthesis of transferrable h-BN. The orientations of triangular h-BN grains were highly controlled by the Cu(111) lattcice, pointing to two main directions. Further, a well aligned monolayer h-BN sheet was obtained by extending the growth time, which also presents the epitaxy of the monolayer h-BN on Cu(111). Carrier transport measurements was also performed for graphene FETs by introducing monolayer h-BN between graphene channel and $SiO_2$ substrate. The

multiple transfer process and monolayer thickness of the h-BN did not improve the transfer characteristics of graphene transistors. Although the device performance was not improved, monolayer h-BN is expected to find many applications, such as gas barrier sheet and tunneling barriers.

## References

1. Dean, C. R. *et al.* Boron nitride substrates for high-quality graphene electronics. *Nat. Nanotechnol.* **5**, 722–726 (2010).

2. Britnell, L. *et al.* Electron tunneling through ultrathin boron nitride crystalline barriers. *Nano Lett.* **12**, 1707–1710 (2012).

3. Okada, M. *et al.* Direct chemical vapor deposition growth of $WS_2$ atomic layers on hexagonal boron nitride. *ACS Nano* **8**, 8273–8277 (2014).

4. Cui, X. *et al.* Multi-terminal transport measurements of $MoS_2$ using a van der Waals heterostructure device platform. *Nat. Nanotechnol.* **10**, 534–540 (2015).

5. Piquemal-Banci, M. *et al.* 2D-MTJs: introducing 2D materials in magnetic tunnel junctions. *J. Phys. D: Appl. Phys.* **50**, 203002 (2017).

6. Novoselov, K. S. *et al.* Two-dimensional atomic crystals. *PNAS* **102**, 10451–10453 (2005).

7. Song, L. *et al.* Large scale growth and characterization of atomic hexagonal boron nitride layers. *Nano Lett.* **10**, 3209–3215 (2010).

8. Kim, K. K. *et al.* Synthesis of monolayer hexagonal boron nitride on Cu foil using chemical vapor deposition. *Nano Lett.* **12**, 161–166 (2012).

9. Guo, N. *et al.* Controllable growth of triangular hexagonal boron nitride domains on copper foils by an improved low-pressure chemical vapor deposition method.

*Nanotechnology* **23**, 415605 (2012).

10. Tay, R. Y. *et al.* Growth of large single-crystalline two-dimensional boron nitride hexagons on electropolished copper. *Nano Lett.* **14**, 839–846 (2014).

11. Iqbal, M. W., Iqbal, M. Z., Jin, X., Eom, J. and Hwang, C. Superior characteristics of graphene field effect transistor enclosed by chemical-vapor-deposition-grown hexagonal boron nitride. *J. Mater. Chem. C* **2**, 7776–7784 (2014).

12. Khan, M. H. *et al.* Synthesis of large and few atomic layers of hexagonal boron nitride on melted copper. *Sci Rep* **5**, 7743 (2015).

13. Wu, Q. *et al.* Single crystalline film of hexagonal boron nitride atomic monolayer by controlling nucleation seeds and domains. *Sci Rep* **5**, 16159 (2015).

14. Sinha, S., Takabayashi, Y., Shinohara, H. and Kitaura, R. Simple fabrication of air-stable black phosphorus heterostructures with large-area hBN sheets grown by chemical vapor deposition method. *2D Mater.* **3**, 035010 (2016).

15. Lee, Y.-H. *et al.* Growth selectivity of hexagonal-boron nitride layers on Ni with various crystal orientations. *RSC Adv.* **2**, 111–115 (2011).

16. Ismach, A. *et al.* Toward the controlled synthesis of hexagonal boron nitride films. *ACS Nano* **6**, 6378–6385 (2012).

17. Cho, H. *et al.* Growth kinetics of white graphene (h-BN) on a planarised Ni foil surface. *Sci. Rep.* **5**, 11985 (2015).

18. Gao, Y. *et al.* Repeated and controlled growth of monolayer, bilayer and few-layer hexagonal boron nitride on Pt foils. *ACS Nano* **7**, 5199–5206 (2013).

19. Kim, G. *et al.* Growth of high-crystalline, single-layer hexagonal boron nitride on recyclable platinum foil. *Nano Lett.* **13**, 1834–1839 (2013).

20. Orofeo, C. M., Suzuki, S., Kageshima, H. and Hibino, H. Growth and low-energy

electron microscopy characterization of monolayer hexagonal boron nitride on epitaxial cobalt. *Nano Res.* **6**, 335–347 (2013).

21. Nagashima, A., Tejima, N., Gamou, Y., Kawai, T. and Oshima, C. Electronic dispersion relations of monolayer hexagonal boron nitride formed on the Ni(111) surface. *Phys. Rev. B* **51**, 4606–4613 (1995).

22. Yang, Y. *et al.* Creating a nanospace under an h-BN cover for adlayer growth on nickel(111). *ACS Nano* **9**, 11589–11598 (2015).

23. Preobrajenski, A. B. *et al.* Influence of chemical interaction at the lattice-mismatched *h*-BN/Rh(111) and *h*BN/Pt(111) interfaces on the overlayer morphology. *Phys. Rev. B* **75**, 245412 (2007).

24. Orlando, F. *et al.* Epitaxial growth of hexagonal boron nitride on Ir(111). *J. Phys. Chem. C* **116**, 157–164 (2012).

25. Gao, L. *et al.* A nickel nanocatalyst within a h-BN shell for enhanced hydrogen oxidation reactions. *Chem. Sci.* **8**, 5728–5734 (2017).

26. Preobrajenski, A., Vinogradov, A. S. and Mårtensson, N. Monolayer of h-BN chemisorbed on Cu(111) and Ni(111): the role of the transition metal 3d states. *Surf. Sci.* **582**, 21–30 (2005).

27. Joshi, S. *et al.* Boron Nitride on Cu(111): an electronically corrugated monolayer. *Nano Lett.* **12**, 5821–5828 (2012).

28. Roth, S., Matsui, F., Greber, T. and Osterwalder, J. Chemical vapor deposition and characterization of aligned and incommensurate graphene/hexagonal boron nitride heterostack on Cu(111). *Nano Lett.* **13**, 2668–2675 (2013).

29. Uchida, Y., Iwaizako, T., Mizuno, S., Tsuji, M. and Ago, H. Epitaxial chemical vapour deposition growth of monolayer hexagonal boron nitride on a Cu(111)/sapphire

substrate. *Phys. Chem. Chem. Phys.* **19**, 8230–8235 (2017).

30. Ago, H. *et al.* Epitaxial growth and electronic properties of large hexagonal graphene domains on Cu(111) thin film. *Appl. Phys. Express* **6**, 075101 (2013).

31. Li, X. *et al.* Large-area synthesis of high-quality and uniform graphene films on copper foils. *Science* **324**, 1312–1314 (2009).

32. Liu, Y., Bhowmick, S. and Yakobson, B. I. BN white graphene with "colorful" edges: the energies and morphology. *Nano Lett.* **11**, 3113–3116 (2011).

33. Laskowski, R., Blaha, P. and Schwarz, K. Bonding of hexagonal BN to transition metal surfaces: an ab initio density-functional theory study. *Phys. Rev. B* **78**, 045409 (2008).

34. Gómez Díaz, J. *et al.* Hexagonal boron nitride on transition metal surfaces. *Theor. Chem. Acc.* **132**, 1350 (2013).

35. Kim, D. Y. *et al.* Role of hydrogen carrier gas on the growth of few layer hexagonal boron nitrides by metal-organic chemical vapor deposition. *AIP Adv.* **7**, 045116 (2017).

36. Kidambi, P. R. *et al.* In situ observations during chemical vapor deposition of hexagonal boron nitride on polycrystalline copper. *Chem. Mater.* **26**, 6380–6392 (2014).

37. Lu, G. *et al.* Synthesis of large single-crystal hexagonal boron nitride grains on Cu–Ni alloy. *Nat. Commun.* **6**, 6160 (2015).

38. Paszkowicz, W., Pelka, J. B., Knapp, M., Szyszko, T. and Podsiadlo, S. Lattice parameters and anisotropic thermal expansion of hexagonal boron nitride in the 10–297.5 K temperature range. *Appl. Phys. A* **75**, 431–435 (2002).

39. Frueh, S. *et al.* Pyrolytic decomposition of ammonia borane to boron nitride. *Inorg. Chem.* **50**, 783–792 (2011).

40. Whitman, L. J., Joyce, S. A., Yarmoff, J. A., McFeely, F. R. & Terminello, L. J. The chemisorption of chlorosilanes and chlorine on Si(111)7 × 7. *Surf. Sci.* **232**, 297–306 (1990).

41. Hu, B. *et al.* Epitaxial growth of large-area single-layer graphene over Cu(111)/sapphire by atmospheric pressure CVD. *Carbon* **50**, 57–65 (2012).

42. Paffett, M. T., Simonson, R. J., Papin, P. and Paine, R. T. Borazine adsorption and decomposition at Pt(111) and Ru(001) surfaces. *Surf. Sci.* **232**, 286–296 (1990).

43. Ago, H. *et al.* Controlled van der Waals epitaxy of monolayer $MoS_2$ triangular domains on graphene. *ACS Appl. Mater. Interfaces* **7**, 5265–5273 (2015).

# Chapter 5

# Controlled growth of large-area, uniform multilayer h-BN and application to 2D substrate

(Part of this chapter is published in *ACS Nano* **12**, 6236-6244 (2018))

## 5.1   Introduction

In the CVD growth of h-BN, like the case of graphene growth, Cu films/foils have been widely used, which dominantly produces monolayer h-BN on the Cu surface.[1–6] As described in the Chapter 4, the growth of monolayer h-BN is explained by the self-limiting growth mechanism due to the very low solubility of N atoms in Cu metal.[7] The grain size and growth rate of monolayer h-BN can be increased by utilizing Cu-Ni alloy catalyst.[8,9] However, as presented in Chapter 4, monolayer of h-BN is not thick enough to reduce the influences from underlying substrates due to its single-atom thickness.

Therefore, recent effort has been paid more on the synthesis of multilayer h-BN films.[10–14] The growth of multilayer h-BN on Cu catalyst is possible, but it relies on gas-phase thermal decomposition of feedstock, mainly ammonia borane ($BH_3NH_3$), so that the crystallinity of the h-BN is rather low with very small grain size and it lacks film uniformity.[12–14] It is reported that the catalytic activity of Ni foils toward h-BN growth is strongly dependent on the crystalline planes, thus giving h-BN flakes with a large variation in thickness on the polycrystalline Ni foil.[15]

Recently, Kim *et al.* demonstrated the synthesis of multilayer h-BN with high crystallinity by using Fe foil as a catalyst.[10] Since Fe metal has relatively high solubilities for both B and N atoms, the dissolved B and N atoms in the Fe metal can form multilayer h-BN *via* segregation process. However, there remain difficulties in obtaining a uniform h-BN film using Fe catalyst from two reasons. Firstly, Fe metal changes its crystal structure from body-centered cubic (bcc) to face-centered cubic (fcc) at ~912 °C. Thus, since the growth temperature (typically 1000-1100 °C) is higher than this transition temperature, the Fe catalyst experiences structural deformation during both the heating up and cooling down steps in the CVD. As the h-BN segregation takes place preferentially at grain boundaries of the metal catalyst, such structural transformation is detrimental for the growth of a uniform h-BN film. In addition, this structural change of the metal catalyst would introduce large strain in the as-grown multilayer h-BN. Secondly, as the solubilities of B and N atoms in Fe metal are largely different (B: ~0.1 at% at 1149 °C, N: ~8 at% at 1000 °C),[10,16] it is considered that the unbalanced solubility prevents from uniform segregation of h-BN.

In this Chapter, the CVD synthesis of a highly uniform multilayer h-BN sheet is reported, which was realized by using a Ni-Fe alloy film and borazine ($B_3N_3H_6$) as catalyst and feedstock, respectively. The Ni metal stabilizes the fcc structure, being different from pure Fe films/foils that show polycrystalline feature. Also the mixture of Ni and Fe metal can tune the solubility of B and N atoms, resulting in the uniform segregation of multilayer h-BN. The obtained h-BN has a thickness of 2~5 nm with good uniformity, and Raman spectra indicate that the h-BN is well crystallized due to the catalytic segregation process. To assess the applicability of

the multilayer h-BN to a dielectric layer for 2D materials, the optical property of tungsten disulfide ($WS_2$) grown on the h-BN was investigated. The $WS_2$ grains were aligned on the h-BN surface and showed a much stronger and sharper PL peak compared with those directly grown on $SiO_2$ substrate. The method in this work can be developed to the wafer-scale production of high-quality, multilayer h-BN that will boost various practical applications utilizing 2D materials.

## 5.2   Experimental methods

### 5.2.1   Preparation of Ni-Fe catalyst

For the growth of multilayer h-BN, a Ni-Fe film was deposited on a single crystal substrate (spinel ($MgAl_2O_4$ (CRYSTAL GmbH)) or MgO (Tateho Chemical Industries Co.)) by radio-frequency (RF) sputtering. In the sputtering process, a Ni film (thickness 700 nm, 99.99% from Kojundo Chemical Laboratory Co.) was first deposited, followed by depositing a Fe film (300 nm, 99.9%) on it. The concentration of the Ni and Fe is defined by the nominal thickness of each film. For comparison, the pure Fe and Ni films were independently deposited on the single crystal substrates with a film thickness of 1 $\mu$m. Commercially available Fe foil was also used as a catalyst (Nilaco Co., >99%, 20 $\mu$m thickness).

### 5.2.2   CVD growth of multilayer h-BN

For the growth of h-BN, a catalyst was placed in the CVD chamber which is connected to the borazine supply system that is kept at -10 °C. The CVD setup is

illustrated in Figure 5-1a. While flowing $H_2$ gas, the furnace was heated up to 1100 °C and maintained for one hour to promote alloying of the metal catalyst as well as to improve the crystallinity and surface flatness. Then, borazine vapor was introduced into the CVD chamber with pressure of ~30 Pa. The typical reaction time was 30 min. After the reaction, the borazine supply was stopped, and the furnace was cooled down slowly while controlling the cooling rate, typically 5 °C/min. The as-grown h-BN was transferred from the metal catalyst to a $SiO_2$/Si substrate by the polymer-mediated transfer method using poly(methyl methacrylate) (PMMA) and iron chloride ($FeCl_3$) as support layer and etching solution, respectively.

### 5.2.3   CVD growth of monolayer WS$_2$

Monolayer $WS_2$ growth was performed by ambient-pressure CVD in the presence of the h-BN/$SiO_2$ substrate using $WO_3$ and S powders as precursors. As illustrated in Figure 5-1b, the double-tube configuration was used for the $WS_2$ synthesis in order to avoid the reaction of $WO_3$ source with sulfur before sublimation of $WO_3$. The temperatures of $WO_3$, S, and the substrate were set at 165, 1060, and 800 ºC, respectively.

### 5.2.4   Characterizations

The metal catalysts used for the h-BN growth were characterized by electron back scatter diffraction (EBSD, TSL Solutions OIM) attached to scanning electron microscope (SEM, Zeiss Ultra55). Optical microscope (NIKON Eclipse 300) with the charge-coupled

device (CCD) camera (Nikon SD-Fi1) was used to measure the uniformity of the h-BN film with the aid of the image analysis software (Mitani Co. WinROOF. The surface and the thickness of h-BN films were characterized by atomic force microscope (AFM, Bruker Nanoscope V).  SEM images and energy dispersive x-ray spectroscopy (EDX) data were measured with HITACHI S-4800 and Bruker FlatQUAD, respectively. Cross-sectional transmission electron microscope (TEM) images were measured with HITACHI H9500. The TEM specimen was cut from the as-grown sample by a focused-ion beam (FIB, HITACHI NB5000) after protecting the h-BN surface with amorphous carbon. Raman and photoluminescence (PL) spectra were measured with a confocal Raman spectroscope (Tokyo Instruments Inc. Nanofinder30) using a laser excitation with 532 nm wavelength. Peak deconvolution of PL spectra was performed with Gaussian-Lorentzian mixed curves (Voight function). X-ray photoelectron spectroscopy (XPS) was measured with a Kratos Axis 165 spectrometer with a monochromatic Al X-ray source.
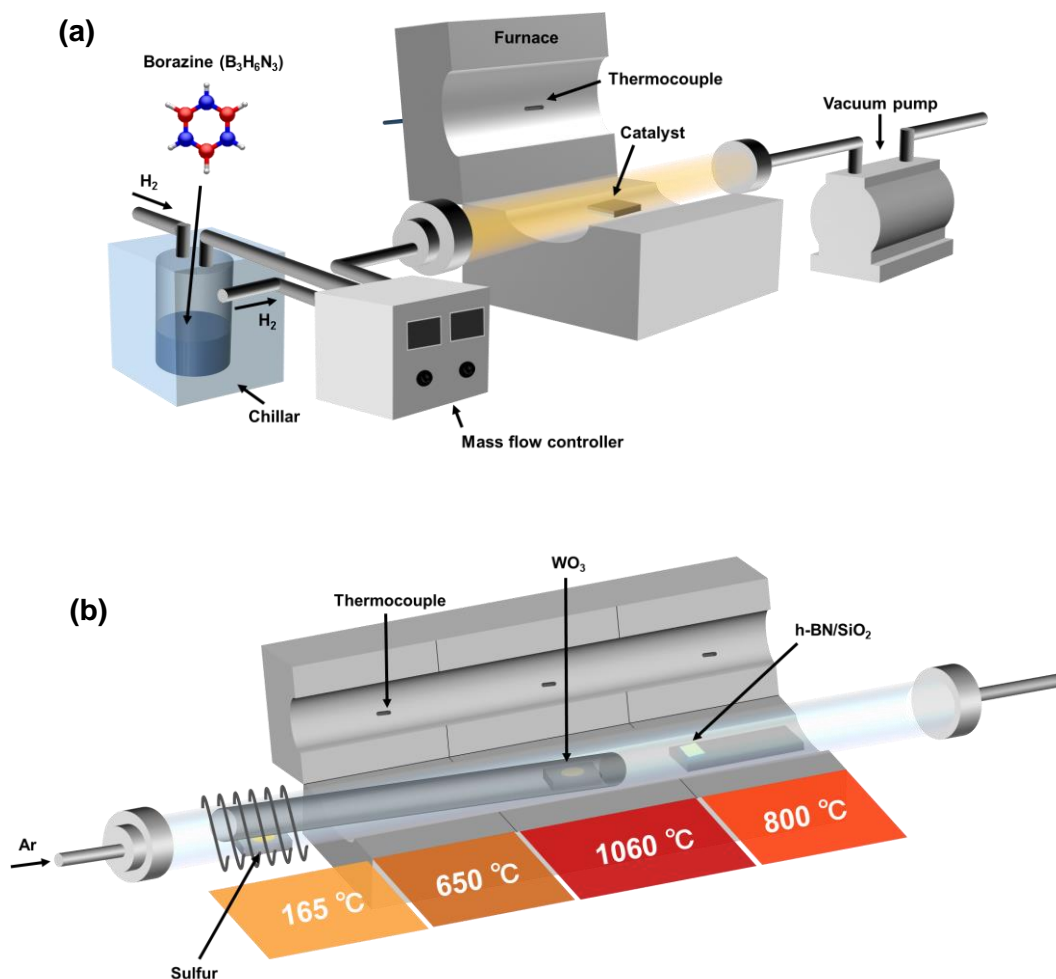
**Figure 5-1.** CVD setups used to grow multilayer h-BN (a) and WS$_2$ (b).

## 5.3   Results and discussion

### 5.3.1   Synthesis of large-area and uniform multilayer h-BN

Figure 5-2a illustrates the procedure used to synthesize uniform multilayer h-BN by CVD process. The multilayer h-BN growth relies on the dissolution of B and N atoms in metal catalyst and the subsequent segregation as hexagonal BN layers. This dissolution-segregation process induced by the metal catalyst is essential to obtain a multilayer h-

BN film with high crystallinity. Multilayer h-BN was synthesized by using the CVD setup shown in Figure 5-1a. Here, borazine was used as a feedstock, because it is possible to avoid the formation of by-products, such as BN nanoparticles, which are frequently observed when ammonia borane is used as a precursor, as discussed in Chapter 4. In addition, since borazine is liquid with a low boiling point (55 °C), it is much easier to control the supply rate as compared with solid ammonia borane. In this Chapter, spinel ($MgAl_2O_4$) and MgO single crystal substrates with (100) and (111) planes were used to deposit metal catalyst films. Single crystalline substrates promote the formation of epitaxial metal films with less grain boundaries compared with conventional metal foils. These substrates also allow to investigate effects of a crystalline plane of a metal catalyst film.

Figure 5-2b shows the optical micrograph of a h-BN sheet grown on a Ni-Fe alloy film (Ni-70%) deposited on spinel(100). For the analysis of thickness and uniformity of h-BN, the as-grown h-BN was transferred on a $SiO_2$(300 nm)/Si substrate using the polymer-mediated transfer technique (described in Experimental Section of Chapter 4).[34] This optical image demonstrates the controlled synthesis of the large-area uniform h-BN sheet. To analyze the surface structure, h-BN surface was measured by AFM, as shown in Figure 5-2c. The area having a hole was measured to show the presence of multilayer h-BN. This image confirms the formation of a uniform and continuous film, being consistent with the optical image. The height of the h-BN film was estimated to be ~3 nm (lower panel of Figure 5-2c), which corresponds to ~8 h-BN layers.

Raman spectra of the transferred film (Figure 5-2e) showed a characteristic $E_{2g}$ band of h-BN at 1365-1370 $cm^{-1}$, verifying the growth of h-BN on the alloy catalyst. It is known
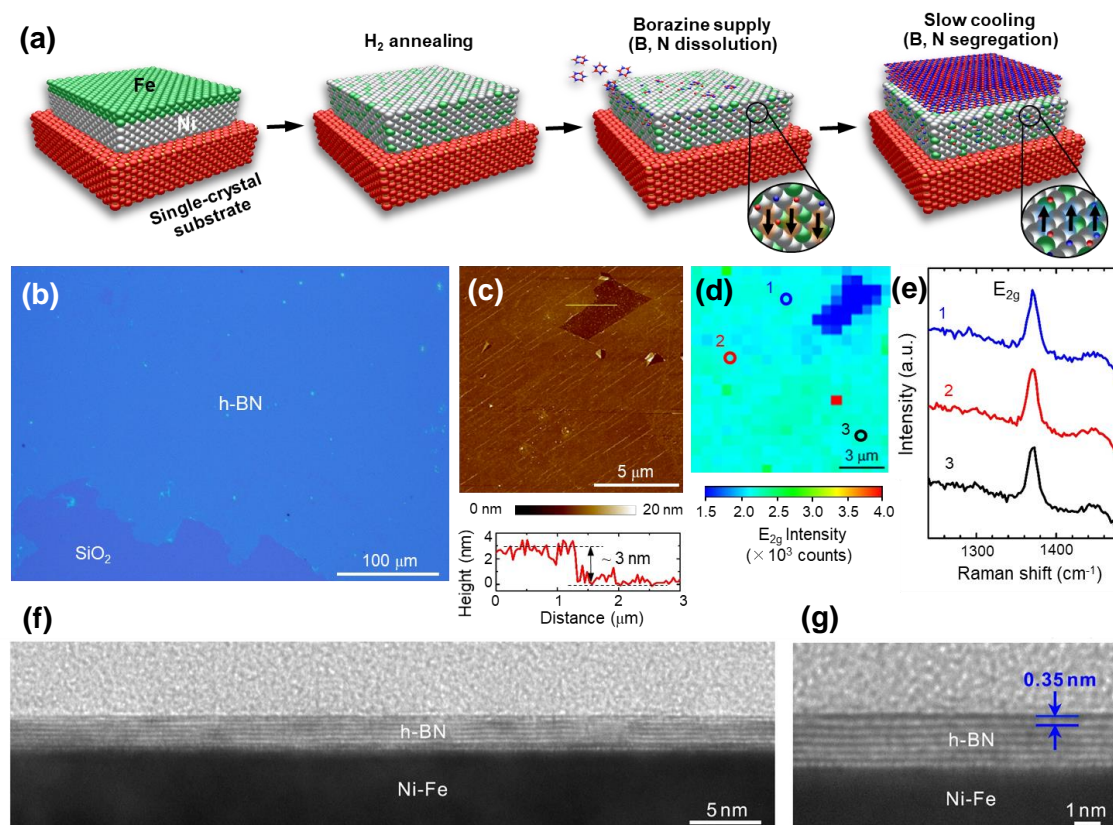
**Figure 5-2.** (a) Schematic of the CVD growth of multilayer h-BN on Ni-Fe alloy film catalyst. (b,c) Optical and AFM images of h-BN grown on Ni-Fe film deposited on spinel(100) substrate measured after the transfer on $SiO_2$/Si substrate. Lower panel of (c) shows the height profile measured along the yellow line in the AFM image. (d) Raman mapping image of $E_{2g}$ intensity of the h-BN film without pixel interpolation. The interval of each measured spot is 0.67 $\mu$m for both x- and y-axes. (e) Raman spectra collected at the positions marked in (d). (f,g) Cross-sectional TEM images of the as-grown h-BN on the Ni-Fe/spinel(100).

that the $E_{2g}$ intensity increases linearly with increasing the h-BN thickness and that for monolayer h-BN the $E_{2g}$ band is very weak and sometimes its intensity is lower than the detection limit.[6,17] Thus, the clear $E_{2g}$ peaks seen in Figure 5-2e indicates the formation of multilayer h-BN. Moreover, the Raman mapping image of the $E_{2g}$ intensity (Figure 5-2d) collected at the same area shown in Figure 5-2c displays uniform color contrast, confirming the high uniformity of the h-BN thickness (except for the small blue area). The
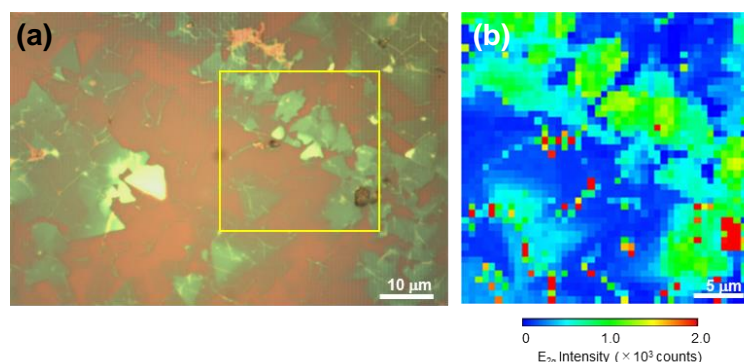
**Figure 5-3.** h-BN grown on the Fe foil. Optical microscope (a) and Raman $E_{2g}$ intensity mapping (b) images of the transferred h-BN. The Raman mapping was measured at the marked area shown in (a). Total 1600 spectra were collected from the 30 μm×30 μm square area (no pixel smoothing process was applied).

deviation from the mean $E_{2g}$ intensity, determined by the Raman mapping, is within 10% in the measured area, again supporting the uniformity of the film thickness. This mapping image is quite different from that of the h-BN sample grown on the Fe foil, shown in Figure 5-3, which has large variation in the $E_{2g}$ intensity. Therefore, the grown h-BN on the Ni-Fe catalyst has a highly uniform film thickness. This is the first time that demonstrates the synthesis of such uniform multilayer h-BN by catalytic CVD method.

The full-width at half maximum (FWHM) of the Raman $E_{2g}$ band is associated with the h-BN crystallinity. As shown in Figure 5-2e, the h-BN transferred from Ni-Fe/spinel(100) showed a sharp $E_{2g}$ band with an average FWHM value of 17 cm$^{-1}$ (see Figure 5-4a for the histogram of the FWHM). This value is much smaller than that of the multilayer h-BN grown on Cu catalyst synthesized *via* non-catalytic decomposition of the feedstock (~30 cm$^{-1}$ or larger).[12–14] Thus, it is highly likely that the multilayer h-BN growth is based on the catalytic segregation from the metal catalyst. Figure 5-4b compares the $E_{2g}$ linewidth of h-BN samples grown by different methods and on different
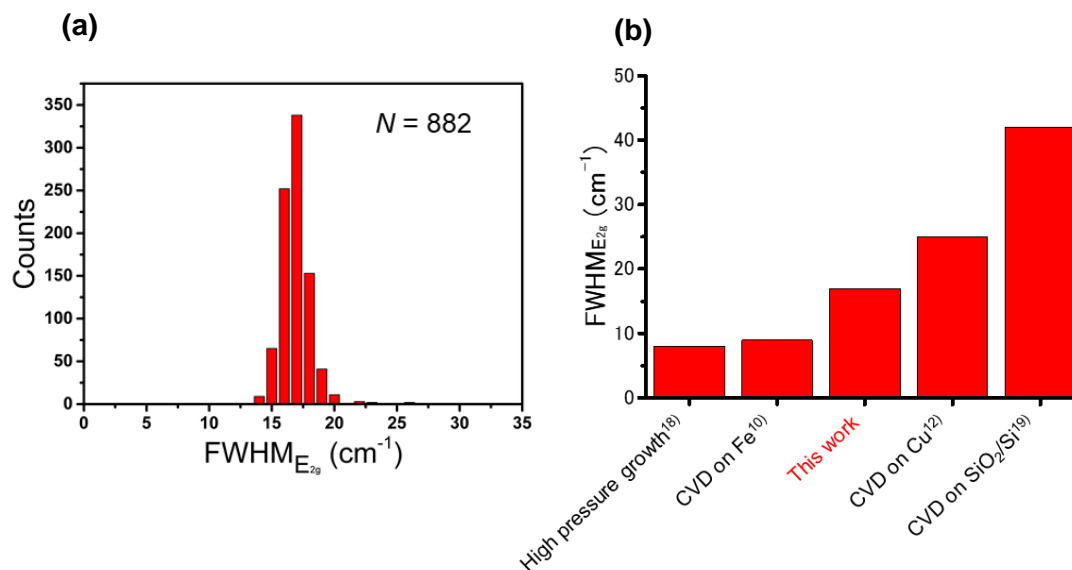
**Figure 5-4.** (a) Distribution of the linewidth of Raman $E_{2g}$ band of the multilayer h-BN grown on Ni-Fe/spinel(100). The Raman was measured after the transfer on a $SiO_2$/Si substrate. (b) Comparison of the $E_{2g}$ linewidth of multilayer h-BN.[10,12,18,19]

catalysts.[10,12,18,19] As the FWHM value of exfoliated h-BN flakes from bulk crystal is narrower (8-9 cm$^{-1}$),[18] there is still space to improve the quality of the h-BN film.

Figure 5-2f,g displays cross-sectional TEM images of the as-grown h-BN on Ni-Fe/spinel(100) catalyst. A well-defined layered structure is clearly seen with an interlayer distance of 0.35 nm (Figure 5-2g). The film thickness determined from Figure 5-2g is ~2.4 nm, being almost consistent with the AFM height (Figure 5-2c). In addition, the TEM image shown in Figure 5-2f indicates uniformity of the h-BN film. The wide area image, shown in Figure 5-5a,b, also supports the uniform film thickness. Electron energy-loss spectroscopy (EELS) analysis confirmed the presence of B and N atoms in the specimen (Figure 5-5c). For reliable macroscopic determination of an atomic ratio of B and N atoms, XPS measurement was also carried out for the as-grown h-BN sample. As shown in

Figure 5-6, the peaks from both B and N atoms were clearly observed. The atomic ratio

determined from their peak intensities, [B]:[N] = 1:0.86, is close to the ideal stoichiometric

ratio of h-BN.
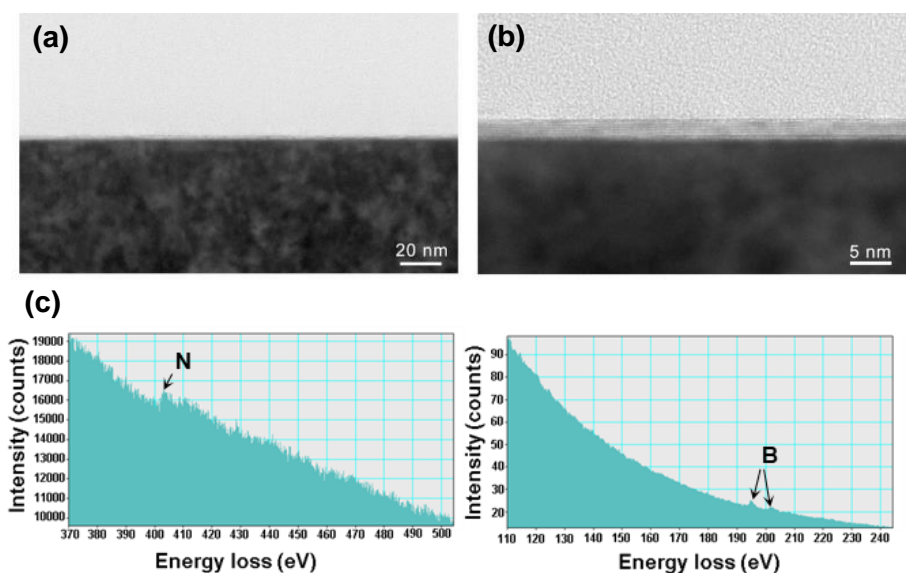


**Figure 5-5.** (a) Low-magnification TEM image of the as-grown h-BN on the Ni-Fe/spinel substrate. (b) shows the magnified image of the square shown in (a). These images indicate that thickness of the multilayer h-BN is highly uniform. (c) EELS spectra showing the presence of both N and B atoms in the specimen.
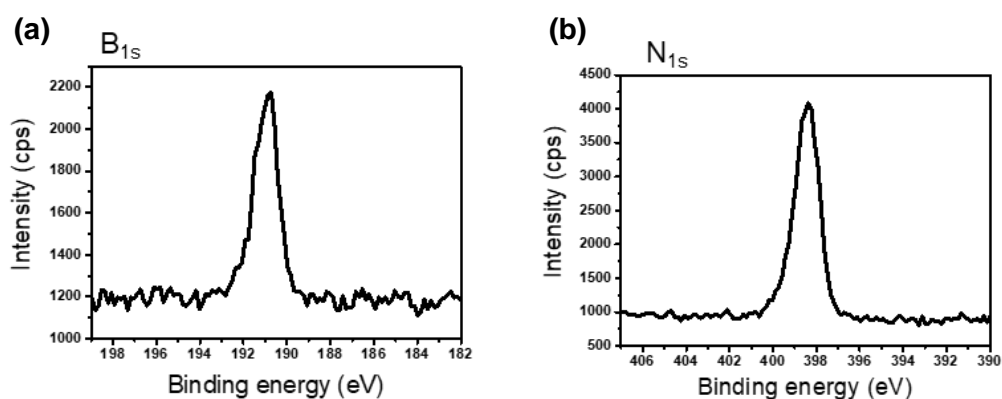


**Figure 5-6.** XPS spectra of the as-grown multilayer h-BN on Ni-Fe/spinel(100). (a) $B_{1s}$ and (b) $N_{1s}$ spectra. The atomic ratio was determined to be [B]:[N]=1:0.86. This ratio is calculated from the relative peak intensity after the correction of the sensitivity factor of each element.

## 5.3.2   Comparison of different catalysts

Figure 5-7a-c compares h-BN films/flakes grown on different metal catalysts which are supported on spinel(100) and MgO(100) substrates. As already mentioned, the Ni-Fe/spinel(100) produced the continuous multilayer h-BN film, which can be also seen in Figure 5-7a. However, when a Ni-Fe film deposited on spinel(111) substrate was employed, no clear optical contrast originated in multilayer h-BN was observed, suggesting that the Ni-Fe/spinel(111) substrate does not give multilayer h-BN (see Figure 5-8a,b). This result can be related to the crystal structure of the alloy metal catalyst, which will be discussed later. Figure 5-7b shows the h-BN grown on the Ni-Fe thin film deposited on MgO(100) substrate instead of spinel(100). Many isolated multilayer h-BN grains were observed whose optical contrast is uniform, suggesting the relatively uniform h-BN thickness. The thickness uniformity within one h-BN grain was also confirmed by Raman mapping measurement, as shown in Figure 5-9c,d. The AFM image (Figure 5-7f
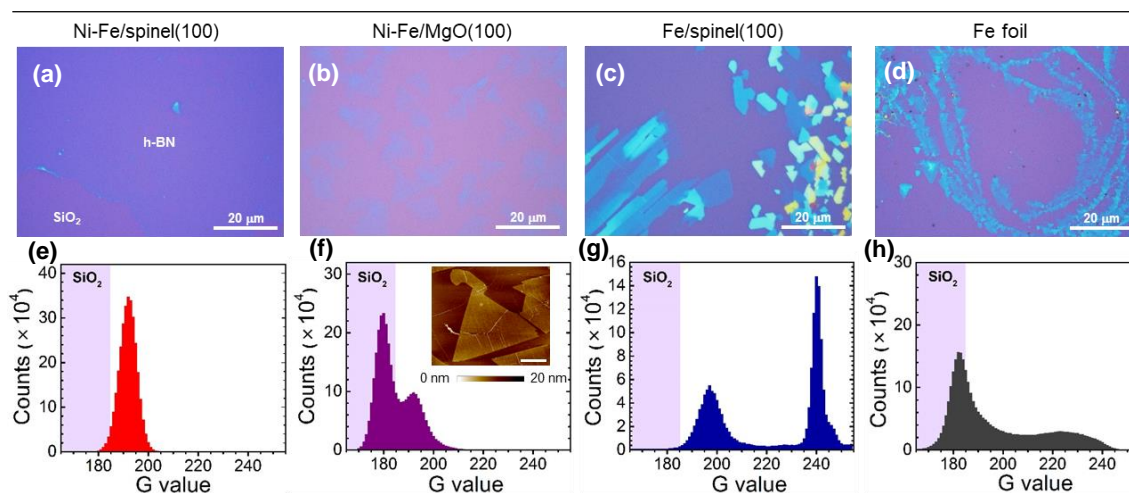


**Figure 5-7.** (a-d) Optical images of the transferred h-BN grown on various catalysts. (e-h) Thickness distribution of h-BN determined form the G value of the optical microscope images. The purple shade indicates the optical contrast corresponding to the $SiO_2$ surface. Inset in (f) is an AFM image of triangular h-BN grain measured after the transfer. Scale bar in the inset is 3 $\mu$m.

inset and Figure 5-9a,b) shows the formation of triangular h-BN grains with a flat surface whose height is around 4.5 nm, supporting the growth of multilayer h-BN. Wrinkles were observed in the AFM image both on the grain surface and outside the grains (see Figure 5-9a), which suggests the formation of thin, 1~2 layer h-BN film covering the Ni-Fe surface in addition to the multilayer h-BN grains.

When a pure Fe film deposited on spinel(100) was subjected to the CVD, the amount of segregated h-BN increased significantly, as shown in Figure 5-7c. However, the h-BN growth occurs inhomogeneously, deteriorating the uniformity of the h-BN film, as compared to the Ni-Fe film (see Figure 5-7a). A number of very thick h-BN flakes were observed in addition to multilayer h-BN covering most of the Fe film surface (Figure 5-7c). The commercial Fe foil (Figure 5-7d) showed the similar tendency with the Fe/spinel(100) catalyst, resulting in the non-uniform formation of thick h-BN flakes. These thick h-BN flakes grown on the Fe foil were linearly arranged, indicating that the h-BN growth occurs *via* segregation of B and N atoms mainly through grain boundaries existing in the Fe foil. The presence of grain boundaries in the Fe foil is reasonable, because the employed Fe foil is polycrystalline and also experiences the phase transformation from bcc to fcc at ~912 $^{\circ}$C that should introduce large strain in the Fe foil. This non-uniform segregation of thick h-BN flakes on Fe foil is consistent with the previous literature.[10] The comparison of Figures 5-7a and 5-7c signifies that the addition of Ni to Fe catalyst greatly improves the uniformity of the h-BN film thickness by suppressing the formation of thick h-BN flakes. On the other hand, a pure Ni films deposited on spinel(100) showed no clear optical contrast on $SiO_2$/Si, indicating the absence of multilayer h-BN (Figure 5-8c,d). These results can be qualitatively understood based on the solubilities of B and N atoms in Fe and Ni metals (see, Table 5-1). At the high temperatures close to the CVD
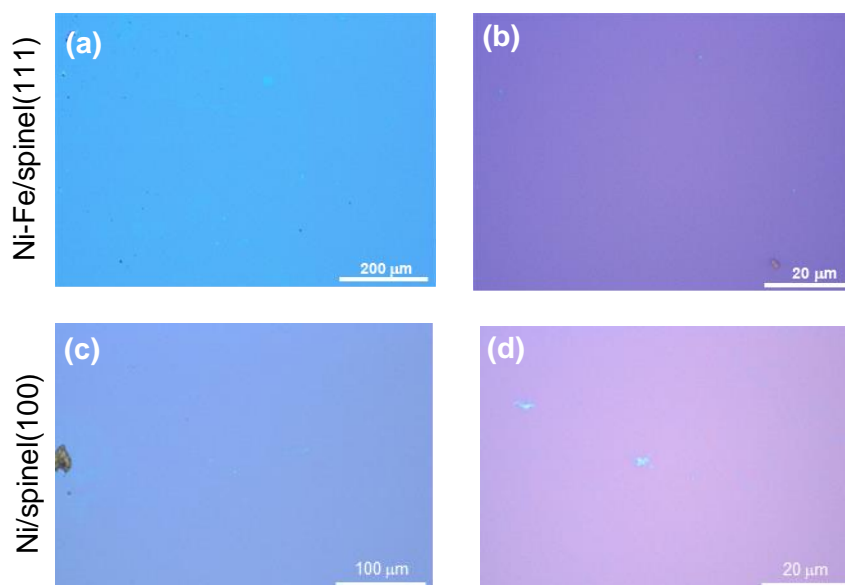
**Figure 5-8.** Optical images with low (a) and high (b) magnifications of the Ni-Fe/spinel(111) substrate. (c,d) Optical images of Ni/spinel(100) substrate. A small number of multilayer h-BN grains were observed in both samples.

**Table 5-1.** Solubilities of B and N atoms in transition metals.

|  | Cu | Ni | Co | Fe |
|---|---|---|---|---|
| B solubility (at%) | ~0.29 [a] (1000 °C) | ~0.3 [c] (1085 °C) | ~0.3 [c] (1110 °C) | ~0.1 [d] (1149 °C) |
| N solubilty (at%) | ~0 [b] | ~0.004 [c] (1550 °C) | ~0.017 [c] (1600 °C) | ~8.0 [e] (1000 °C) |

a) D. J. Chakrabarti *et al., Bull. Alloy Phase Diagram*, **3**, 45 (1982).
b) Okamoto, H. *Phase Diagrams of Binary Iron Alloys* ASM international (1990).
c) S. Suzuki *et al., J. Phys. D: Appl. Phys.*, **45**, 385304 (2012).
d) E. Dudrová, *et al., ISIJ Int.*, **37**, 59 (1997).
e) K. K. Kim *et al., Nat. Commun.*, **6**, 9662 (2015).

temperature, B and N atoms are dissolved in Fe metal with the concentrations of 0.1% and 8%, respectively. On the other hand, almost no N atoms are dissolved in Ni metal, while 0.3% of B atoms can be dissolved in Ni. Therefore, it is speculated that the introduction of Ni to Fe catalyst reduces the solubility of N atoms and modifies the
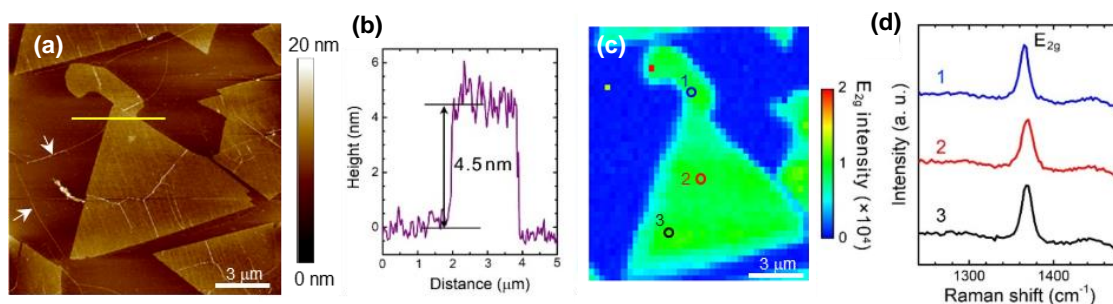
**Figure 5-9.** Multilayer h-BN grains grown on the Ni-Fe/MgO(100). (a) AFM image of the h-BN grain measured after the transfer. It is seen that the surface of the h-BN grain is flat except for wrinkles. Arrows indicate wrinkles on h-BN (outside the grain), suggesting the formation of 1-2L h-BN on the whole catalyst surface. (b) Height profile measured along the yellow line in (a). (c) Raman mapping image of $E_{2g}$ intensity. Total 1600 spectra were collected from the 12 μm×14 μm square area (no pixel smoothing process was applied). (d) Raman spectra collected at the marked positions in (c), signifying the uniform h-BN thickness within the triangular grain.

balance of dissolved B and N atoms, thus enabling the uniform segregation of multilayer h-BN sheet. Also, as discussed later, the single crystal substrates that are used to support the metal alloy film also assist the uniform segregation of h-BN.

The intensity of G (green) component of optical images is found to well correlate with a thickness of transferred h-BN. The details of the optical analysis are described in Figure 5-10. The distributions of the G value are compared in Figure 5-7e-h. Under the measurement condition, a h-BN flake with the G value of 220 roughly corresponds to the thickness of 8 nm based on the AFM measurement. As the G value of a 1-2 L h-BN overlaps with that of the underlying $SiO_2$ substrate (shaded by purple in Figure 5-7e-h), it is difficult to differentiate 1-2L h-BN from bare $SiO_2$ surface based on the optical contrast. However, the existence of multilayer h-BN from the histograms can be clearly seen. For example, in Figure 5-7f the multilayer h-BN can be distinguished from 1-2 layers based on the two separated peaks. Therefore, the histogram shown in Figure 5-

7e presents that the Ni-Fe/spinel(100) catalyst gives a multilayer h-BN sheet with uniform film thickness.
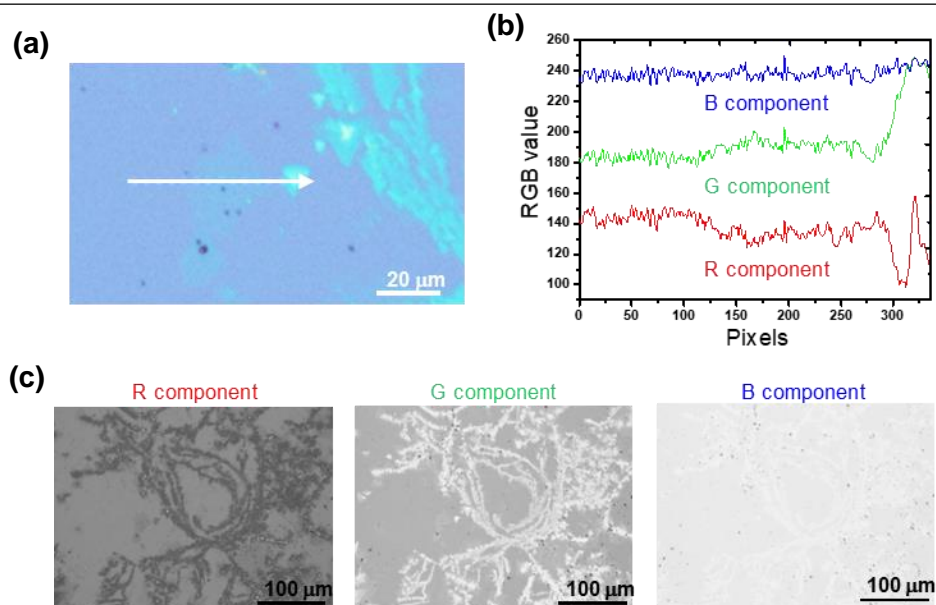


**Figure 5-10.** (a) Optical microscope image of h-BN grown on the Fe foil after the transfer on a SiO$_2$/Si substrate. (b) Intensity of RGB components measured along the white arrow in (a). The G component reflects the optical contrast of the h-BN. (c) Optical microscope image made only from the R, G, and B components. The original optical image is shown in Figure 5-7d.

### 5.3.3 Application of multilayer h-BN to 2D substrate

To demonstrate the feasibility of the grown multilayer h-BN films as a dielectric substrate for 2D materials, the optical properties of transition metal dichalcogenide (TMDC) grown on the multilayer h-BN sheet was investigated. Although the direct synthesis of TMDC/h-BN heterostructure was achieved using sulfide-resistant catalysts, such as Au and Ni-Mo, the thickness of h-BN was not precisely controlled to obtain excellent optical property of the over-grown TMDC.[20,21] After transferring the CVD-grown multilayer h-BN sheet on a SiO$_2$/Si substrate, WS$_2$ was synthesized by the second CVD step using WO$_3$ and S feedstocks using the setup shown in Figure 5-1b.
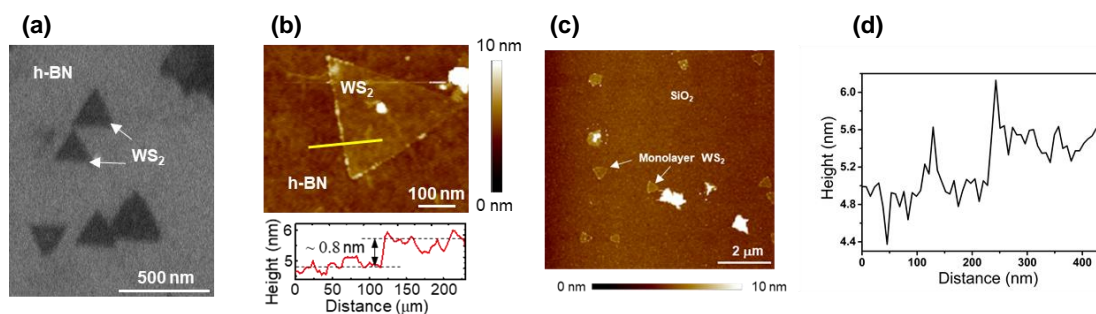
**Figure 5-11.** (a) SEM and (b) AFM images of $WS_2$ grains grown on multilayer h-BN. Lower panel of (b) shows a height profile measured along the yellow line in the AFM image. (c) AFM images of $WS_2$ grains grown on bare $SiO_2$ surface. (d) Height profile measured of the $WS_2$ grain. It is noted that monolayer $WS_2$ grains are randomly oriented on the $SiO_2$ surface.

Figure 5-11a,b shows SEM and AFM images of the $WS_2$ grains grown on the h-BN surface. The triangular shape and the measured AFM height (~0.8 nm) indicate that most of the grains are single-crystalline, monolayer $WS_2$. It is noteworthy that these triangular $WS_2$ grains are aligned in two directions on the multilayer h-BN sheet, indicating the epitaxial growth of $WS_2$. This is consistent with the previous literature that reported the aligned growth of $WS_2$ on mechanically exfoliated h-BN flakes.[22] These results are indicative of the high crystallinity and clean surface of the CVD-grown multilayer h-BN. The grain size of $WS_2$ grown on h-BN is relatively small (< 1 $\mu$m). This size is similar to that of $MoS_2$ grains formed on CVD-grown monolayer graphene, while the grains on sapphire is much larger (10-50 $\mu$m).[23,24] It is also noted that the $WS_2$ grains grown on exfoliated h-BN flakes are also small (a few microns).[22] There are two main reasons for the observed small grain size of $WS_2$ (and $MoS_2$) formed on the CVD-grown h-BN (graphene). Firstly, strong van der Waals interaction limits the grain size due to the limited diffusion of TMDC precursors on these 2D materials. Another reason is that wrinkles and/or contaminants induced during the transfer process of h-BN (or graphene)

can act as nucleation sites, decreasing the TMDC grain size by increasing the nucleation density. It is possible to fully cover h-BN with $WS_2$, as previously demonstrated $MoS_2$/graphene system,[23] by extending the growth time or increase the concentration of the feedstock. However, increasing the grain size can be a more challenging task considering strong van der Waals coupling between the stacked 2D materials.

As shown in Figure 5-12a, the $WS_2$ grains grown on the surface of h-BN exhibited intense PL. The clear PL signal supports that the $WS_2$ grains are monolayer reflecting their direct band gap nature. For comparison, the PL from $WS_2$ grown on the bare $SiO_2$ substrate was also measured (AFM images are shown in Figure 5-11c). Notably, the PL intensity of $WS_2$ grains on h-BN was very strong; ~15 times higher than that grown on $SiO_2$ substrate (Figure 5-12a). Moreover, as shown in the normalized spectra (Figure 5-12b), the PL peak on the h-BN is much narrower than that on the $SiO_2$ substrate. The distributions of PL linewidth are compared in Figure 5-12c. The mean linewidth of $WS_2$/h-BN and $WS_2$/$SiO_2$ are 43 meV and 67 meV, respectively. There is still variation in the linewidth of $WS_2$ on h-BN, indicating that the quality of the CVD-grown h-BN needs to be improved through further optimization of the growth condition. However, it is worthwhile to note that the minimum FWHM value of 24 meV (see Figure 5-12b) obtained for the $WS_2$ grown on the large-area h-BN is comparable or better than that on exfoliated h-BN.[22] This suggests large potential of the CVD-grown multilayer h-BN as an effective insulating layer. Table 5-2 shows the PL linewidths of $WS_2$ samples reported previously.[22,25]

The PL spectrum of $WS_2$ is known to originate in the emission from excitons and charged excitons (trions) that are generated by photo excitation.[26] Excess negative charge supplied from $SiO_2$ surface changes excitons to negative trions. In other words,
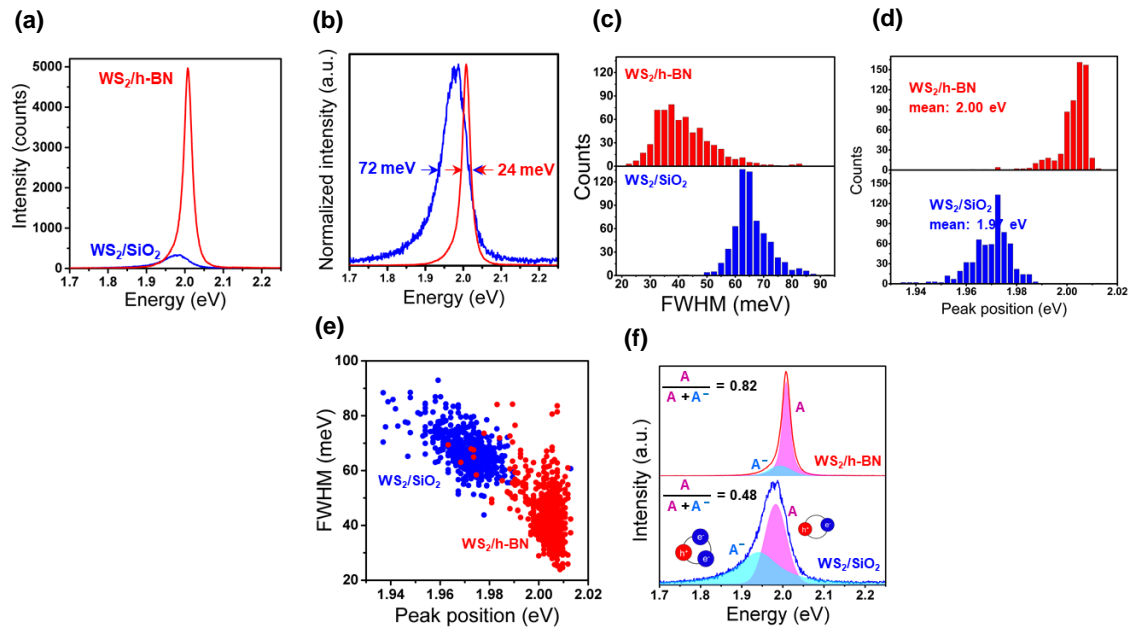
**Figure 5-12.** (a) Representative PL spectra of the WS$_2$ grown on h-BN (red) and SiO$_2$/Si (blue) substrates. (b) Normalized PL spectra. (c,d) Distributions of the PL linewidth and PL peak position (total number of collected spectra is >600 for each sample). (e) Relationship between the PL linewidth and peak position. (f) Curve-fitted PL spectra of WS$_2$ on h-BN (upper) and SiO$_2$/Si substrate (lower). Pink and light blue peaks represent exciton (A) and charged exciton (A$^-$), respectively. The A/(A+A$^-$) ratio is calculated from the peak areas.

the presence of the trion peak indicates that WS$_2$ is negatively doped from the SiO$_2$ surface. To estimate the doping level of WS$_2$ grains grown on h-BN and SiO$_2$, a ratio of exciton-based emission (r) to total PL intensity was calculated based on:

$$r = A / (A + A^-) \qquad (1)$$

where A and A$^-$ are the integrated areas of exciton and trion peaks. The peak deconvolution shown in Figure 5-12f verifies that the ratio of the exciton peak in the observed PL increased substantially for the WS$_2$ on the multilayer h-BN. Therefore, the presence of h-BN strongly suppresses the formation of trions in WS$_2$ by screening out the influence from the charge impurity existing on the SiO$_2$ surface.

**Table 5-2.** Comparison of FWHM of PL peak from several monolayer WS$_2$ samples.[22,25]

|  | WS$_2$/ CVD h-BN | WS$_2$/ exfoliated h-BN | WS$_2$/ SiO$_2$/Si | WS$_2$/ sapphire |
|---|---|---|---|---|
| FWHM of PL peak | 24 meV (this work) | 22[22], 26[25] | 61[22] | 53[22] |

In Figure 5-12d and 5-12e, the PL peak position and the relationship with the PL line is plotted. It was found that the emission energy from the WS$_2$ on SiO$_2$ (blue data) is lower than that on the multilayer h-BN (red). As seen in the fitting curves of Figure 5-12f, the intensity of trion peak (A$^-$; light blue) is stronger on the SiO$_2$ substrate which slightly shifts the PL peak position. At the same time, the exciton peak (A; pink) also shifted to the lower energy on the SiO$_2$. In addition, the exciton peak (A) of h-BN was found to be broader on the SiO$_2$ than that on the h-BN. It is speculated that the shift of the PL energy as well as the broadening of the exciton peak on the SiO$_2$ substrate is originated in strain, because the PL peak position is sensitive to the strain.[27] Considering the low friction observed in WS$_2$ grown on graphite surface,[25] it is reasonable that the WS$_2$ on h-BN surface has less strain than that on SiO$_2$ surface. This low strain in the WS$_2$ directly grown on the h-BN may also contribute to the observed strong PL intensity with a narrow linewidth.

### 5.3.4  Mechanism of catalytic growth of multilayer h-BN

For crystallographic investigation of metal catalysts, EBSD was measured after the h-BN growth. Figure 5-13a-d represent the crystalline phase, while Figure 5-13e-h display the crystalline plane normal to the metal surface. The red color in Figure 5-13a,b signifies that the Ni-Fe films deposited on both spinel(100) and MgO(100) substrates

have a fcc structure. The Ni-Fe film was prepared by depositing a Ni film (700 nm) thickness) on the single crystal substrate, followed by depositing a thin Fe film (300 nm). Thus, an EBSD image of the as-deposited film exhibited a bcc structure originated from the upper Fe layer (not shown here), since the EBSD pattern is generated by the elastic reflection of back scatter electrons near the surface (down to 50 nm). However, as seen in Figure 5-13a,b these metal films showed a fcc structure after the h-BN growth. The observation of the fcc crystal phase (Figure 5-13a,b) implies that Ni stabilizes the fcc structure of Ni-Fe alloy, as reported previously.[28]

The catalyst compositions were measured by EDX. The result is summarized in Figure 5-13i-l. The EDX before the CVD process signified that the surface is pure Fe (Figure 5-13i,k). On the other hand, after the CVD, the catalyst showed the mixture of Ni and Fe with almost the expected ratio (Figure 5-13j,l). This verifies the formation of the Ni-Fe alloy in the high-temperature CVD process.

Unexpectedly, after the CVD, the Ni-Fe films deposited on spinel(100) and MgO(100) substrates exhibited fcc(111) and fcc(110) planes, respectively , as shown in Figure 5-13e,f. Also the EBSD images of Figure 5-13e,f indicate that these Ni-Fe films are highly crystallized with a low density of grain boundaries in the metal alloys. It is highly likely that the high crystallinity of the Ni-Fe film plays an essential role in the segregation of multilayer h-BN with a uniform thickness.

As shown in Figure 5-13c,d, the Fe spinel(100) and Fe foil showed bcc structures after the CVD. This is stark contrast with the results of the Ni-Fe films (Figure 5-13a,b). The observed bcc structure in the Fe catalysts is reasonable, since Fe metal has a bcc structure at room temperature (the Fe metals should have a fcc structure at the growth temperature, then returning to bcc during the cooling down process). The inverse pole
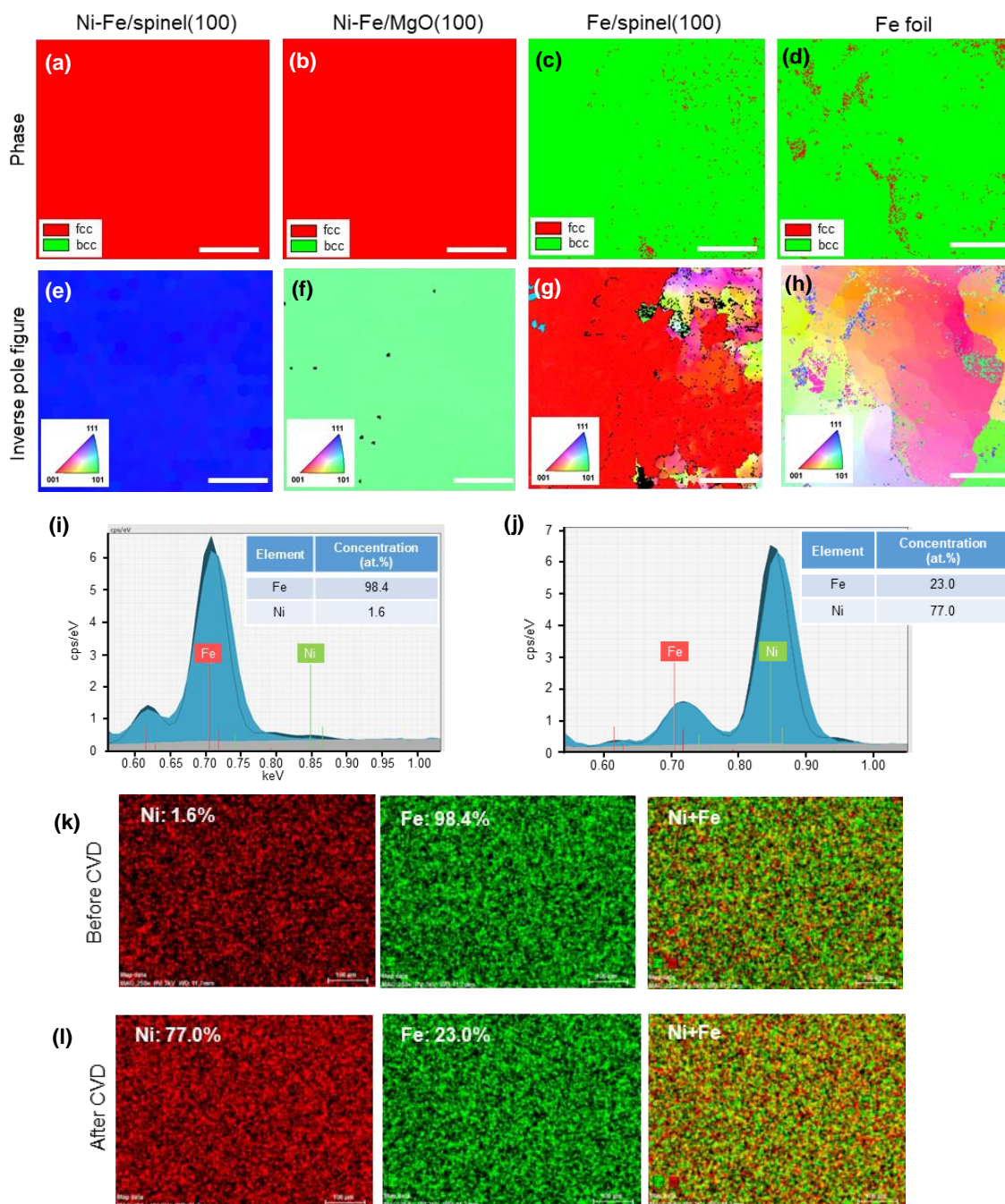
**Figure 5-13.** Phase maps (a-d) and inverse pole figure maps (e-h) of metal catalysts measured by EBSD. All the scale bars are 100 $\mu$m. EDX analysis of the Ni-Fe (Ni-rich) film on spinel(100) substrate measured before (i,k) and after (j,l) the CVD growth of h-BN. (i,j) Original EDX spectra and the calculated atomic ratios. The electron acceleration energy was 3 kV. According to the Monte Carlo simulation, the information from the top surface with 200-300 nm thickness is expected to be detected. The EDX images (k,l) show that both Ni and Fe are uniformly distributed after the CVD.

figures (Figure 5-13g,h) of the Fe foil/film indicate the polycrystalline structures having different crystal planes. This is supposed to be related with the above-mentioned phase transition of the Fe metal. The presence of many grain boundaries and unbalanced solubilities of B and N atoms in the Fe catalysts can be the main reasons of the observed inhomogenous h-BN films with many thick h-BN flakes (see Figure 5-7c,d).

In this work, the Ni-Fe alloy films with a different metal ratio, Ni-30% Fe-70% (a higher Fe concentration than Ni) were also studied as a catalyst using spinel(100) and MgO(100) substrates. The optical images of the transferred h-BN films are shown in Figure 5-14a,b. These alloy films produced multilayer h-BN, but its uniformity is lower than that observed for the Ni-Fe film with the high Ni concentration (Ni-70%). The EBSD data (Figure 5-14c-f) indicates that the metal crystallinity is higher than the Fe film/foils, but it is lower than that observed for the Ni-rich film (see Figure 5-13e,f). This inferior crystallinity compared with Ni-rich alloy film can be one of the reasons that prevents the uniform h-BN segregation, as the grain boundaries stimulate the h-BN formation along the boundaries.

In the case of graphene growth, Cu(111) gives a high-quality graphene sheet with a controlled lattice orientation of the graphene lattice.[29] Thus, a spinel(111) substrate was expected to give h-BN with better quality than spinel(100). However, the Ni-Fe/spinel(111) produced a small number of isolated h-BN grains without forming a continuous sheet (Figure 5-8a,b), suggesting the amounts of dissolved B and N atoms are not large enough to produce uniform multilayer h-BN sheet.

For the further understanding the structural change during the CVD process, the crystal structures of the Ni-Fe films deposited on spine(100) and spine(111) were systematically investigated. The result is shown in Figure 5-15. Figure 5-15b,e is the
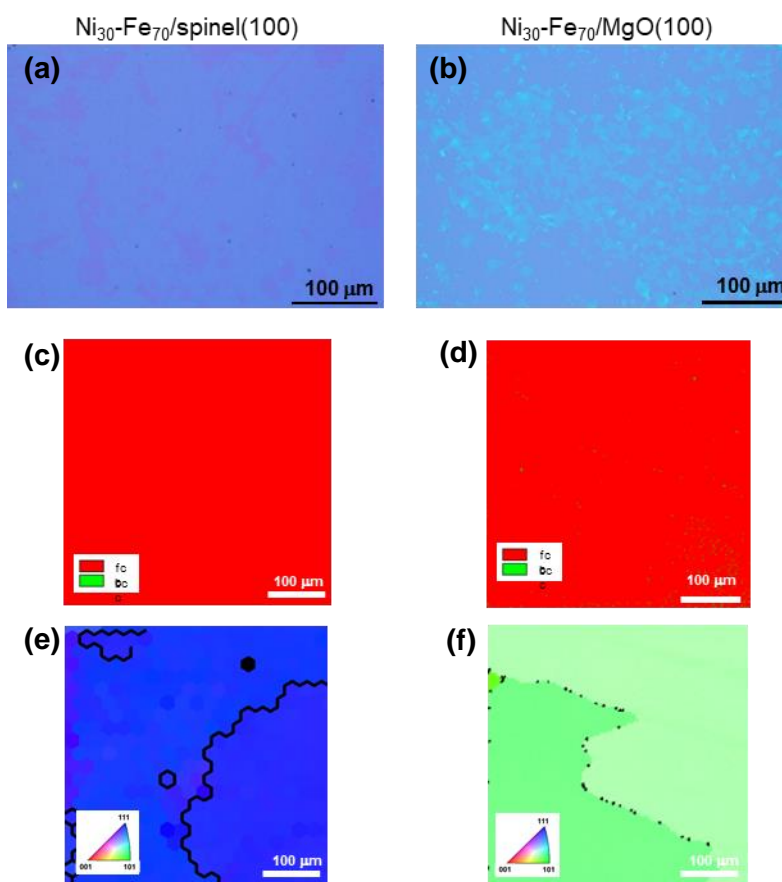
**Figure 5-14.** Optical microscope images of h-BN obtained on the Fe-rich films. (a) $Ni_{30}$-$Fe_{70}$/spinel(100) and (b) $Ni_{30}$-$Fe_{70}$/MgO(100). The thickness of Ni and Fe films are 300 nm and 700 nm, respectively. (c,d) Crystal phases and (e,f) crytal planes of the $Ni_{30}$-$Fe_{70}$ films measured by EBSD.

EBSD measured after hydrogen annealing at 1100 °C, which represent the crystal structure just before the borazine introduction in the CVD process. It was found that the Ni-Fe film on spine(100) shows fcc(100) plane (red contrast), while that on spinel(111) shows fcc(111) (blue contrast).

After the supply of borazine at the growth temperature (1100 ℃) for 30 min, the crystal plane of the Ni-Fe film on spinel(100) changed from fcc(100) to fcc(111) (Figure 5-15c, a part of red area changed to blue). In this experiment, the sample was rapidly cooled just after the switching the borazine supply. In contrast, the Ni-Fe/spinel(111)

showed no obvious change (Figure 5-15f). Therefore, only on the spinel(100), the Ni-Fe film experienced the structural change from fcc(100) to fcc(111). This can be accounted for by the dissolution-segregation process of B and N atoms occurred in the Ni-Fe alloy film when the initial structure is fcc(100). The highest packing density of a fcc(111) plane as well as highest chemical stability among other fcc planes prevents the dissolution of B and N atoms into the Ni-Fe film deposited on spinel(111). Thus, the Ni-Fe/spinel(111) did not catalyze the multilayer h-BN growth. On contrary, the fcc(100) surface has a low packing density, allowing B and N atoms to dissolve into the Ni-Fe film on spinel(100).

The EBSD analysis also revealed that the fcc(100) to fcc(111) conversion proceeds from damaged area of the Ni-Fe/spinel(100) substrate, as shown in Figure 5-15h,i. Because the edge on the Ni-Fe film was damaged while cutting the original wafer, such damaged area becomes more reactive, destabilizing the fcc(100) plane which enhances the conversion to fcc(111) plane. As seen in Figure 5-15c, it is noted that the fcc(100) partly remained after the borazine supply for 30 min.

When the slow cooling process was introduced after the introduction of borazine for 30 min, the fcc(100) of the Ni-Fe film completely changed to the fcc(111), as seen in Figure 5-15d. It is interesting that the Ni-Fe alloy film after this conversion is highly crystallized almost no grain boundaries are seen in Figure 5-15d. Figure 5-15j is the optical micrograph of multilayer h-BN transferred after the reaction with borazine for 30 min (without slow cooling process). Thus, the image corresponds to the h-BN grown on the film indicated in Figure 5-15c. The optical image shows that multilayer h-BN partially covered the Ni-Fe alloy surface. The size and distribution of the h-BN are consistent with those of the fcc(111) plane seen in the Ni-Fe film. Therefore, it is concluded that h-BN segregation occurs simultaneously with the structural conversion of the Ni-Fe catalyst

from fcc(100) to fcc(111). This signifies that the control of the structural conversion is important for the formation of the uniform growth of multilayer h-BN.
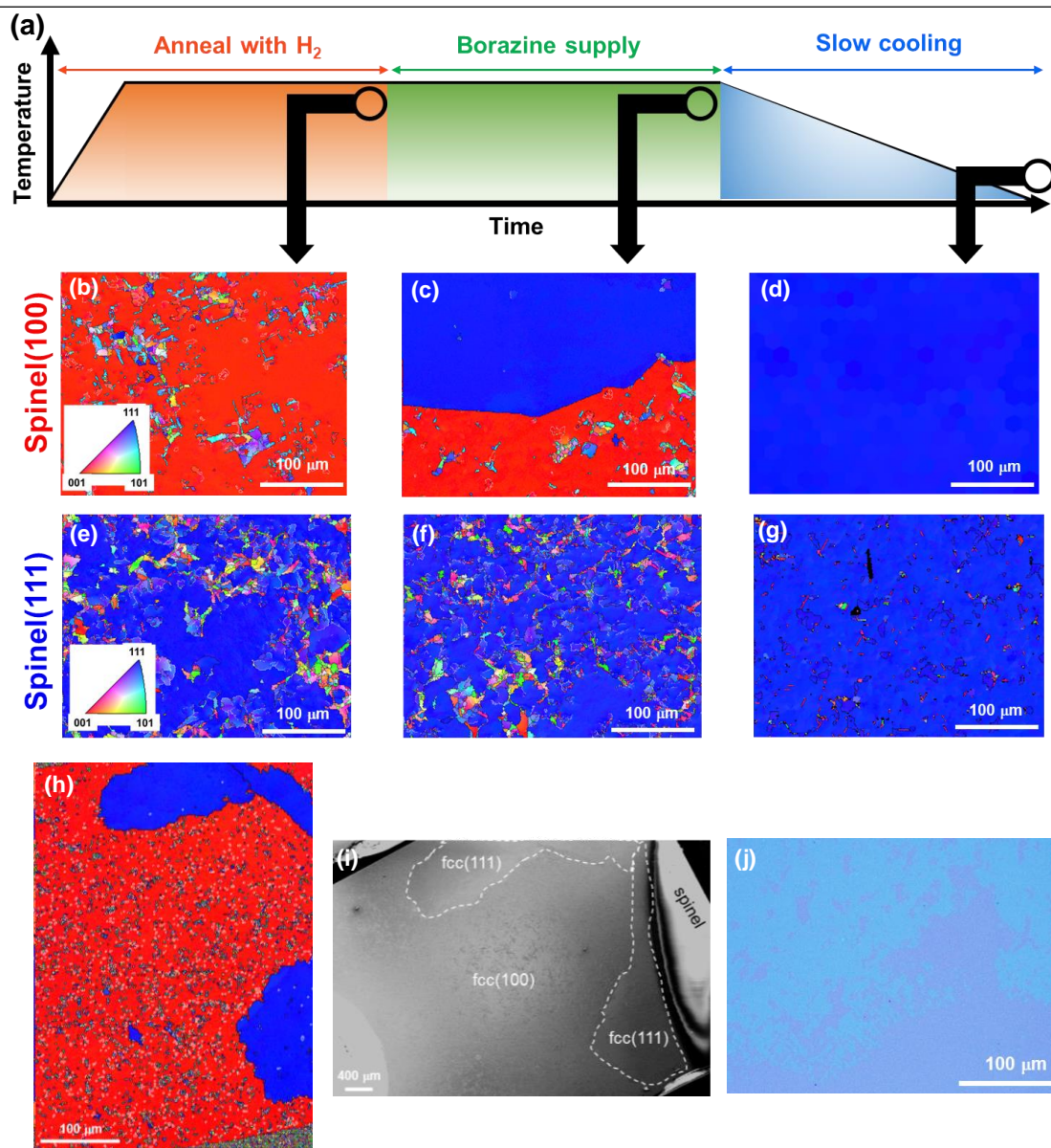


**Figure 5-15.** (a) Temperature profile used during the CVD growth of multilayer h-BN. (b-g) EBSD images of the Ni-Fe films deposited on spinel(100) and spinel(111) substrates. The arrows in (a) indicate that the samples were taken out from the furnace during the CVD process. The growth temperature, annealing time, borazine supply time, and cooling rate were 1100 °C, 60 min, 30 min and 5 °C/min, respectively. Low-magnification crystal plane (h) and SEM images (i) of the Ni-Fe/spinel(100) after 30 min borazine supply. (j) Optical image of h-BN transferred from Ni-Fe/spinel(100) after 30 min borazine supply.

### 5.3.5 Multilayer h-BN growth on sapphire substrates

In the previous section, single crystal spinel substrates were used to deposit Ni-Fe films, because spinel lattices are suitable to form fcc metal films on it. Sapphire is a more widely used substrate, as discussed in Chapter 4. because sapphire is a cost-effective substrate with availability of large wafers (up to 6 inch), as compared with spinel. The prices of spinel and sapphire wafers purchased from Crystal Base Co. and Namiki Precision Co. are compared in Figure 5-16. As the price varies with the number of wafers purchased at one time as well as the wafer size, Figure 5-16 is a simple comparison available in our laboratory.

Therefore, in this thesis, the h-BN growth on the Ni-Fe film supported on sapphire substrates were also studied, because as mentioned above, the development of multilayer growth based on Ni-Fe/sapphire substrate is valuable for the commercial applications. Here, c-plane (0001) and r-plane ($1\bar{1}02$) sapphire wafers were used for the experiments. Figure 5-17a,b shows the optical images of transferred films of h-BN grown on Ni-Fe (Ni-70%) deposited on c-plane and r-plane sapphire. This Ni concentration is the same with that used in Figures 5-2, 5-7a, and 5-9. A clear difference



**Spinel (10 mm²): 7500 JPY**  **Sapphire (4 inch wafer): 8000 JPY**

~7500 JPY/cm²  ~102 JPY/cm²
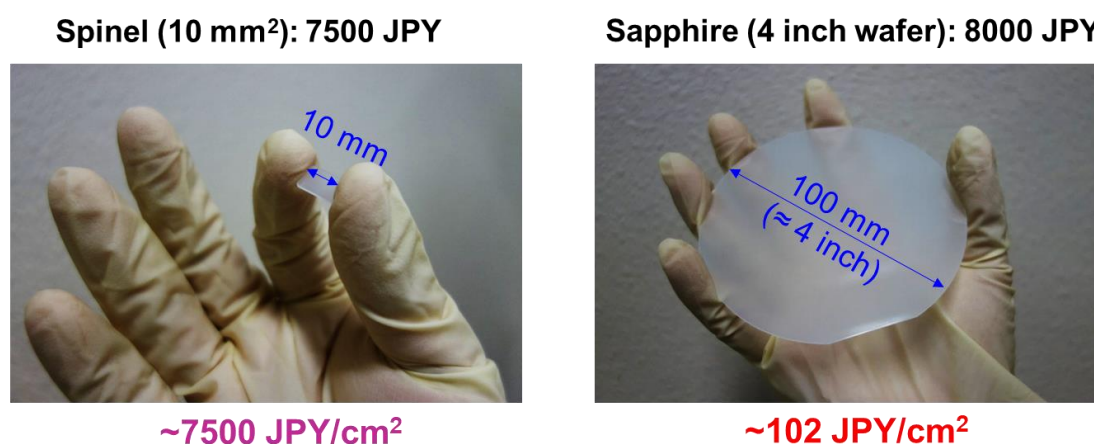
**Figure 5-16.** Photographs of spinel and sapphire substrates purchased in our laboratory with prices of each substrate.

was observed in the h-BN grown on two sapphire samples. The Ni-Fe/r-plane sapphire (Figure 5-17b) produced relatively uniform multilayer h-BN, while h-BN was partially observed on the c-plane sapphire (Figure 5-17a). Using these two sapphire substrates, a Fe-rich alloy with a Ni-30% concentration was also investigated. The result is shown in Figure 5-17c,d. No clear difference was observed in the Fe-rich alloys deposited on c- and r-plane sapphire substrates. Figure 5-17 signifies that the h-BN coverage is the highest when the r-plane sapphire was used with the Ni-rich alloy film.

For better understanding of the observed differences in the h-BN coverage, the crystallographic structures of the Ni-Fe alloy films were analyzed by EBSD. Figure 5-18 shows EBSD data collected at different steps of the CVD (that is, after hydrogen annealing, after borazine supply for 1 min, and after borazine supply for 30 min (see Figure 5-18a for the reaction profile)). The Ni-rich alloy deposited on c-plane sapphire
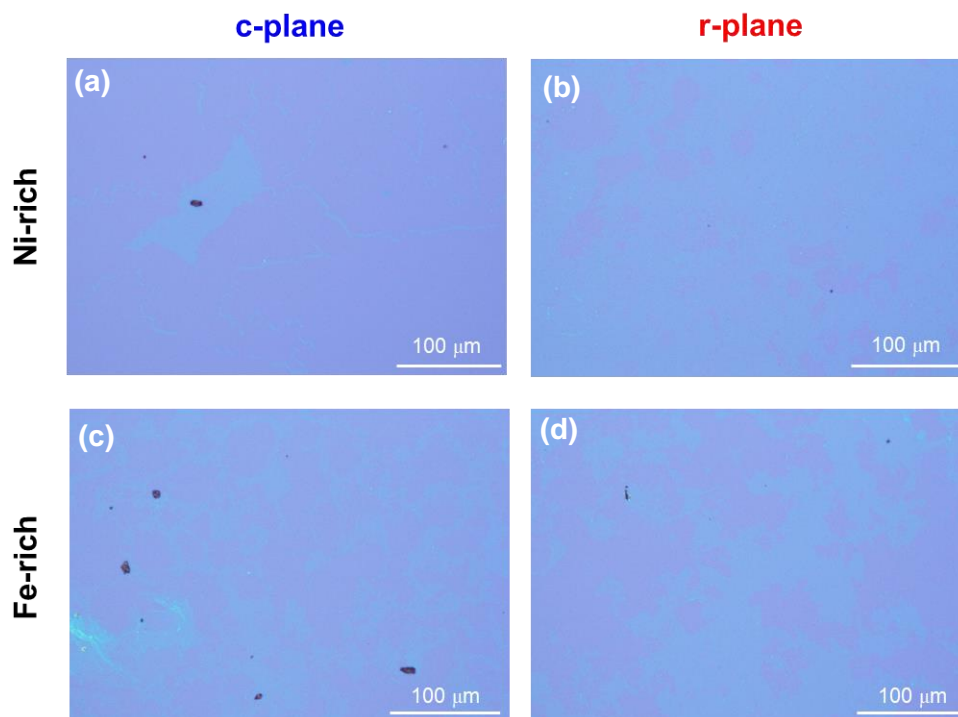


**Figure 5-17.** Optical images of h-BN transferred from Ni-Fe/c-plane and r-plane sapphire. h-BN grown on Ni-rich alloy (a,b) and Fe-rich alloy (c,d).

possessed fcc(111) plane, and it did not show significant change throughout the CVD process (Figure 5-18b-d), being similar to the Ni-Fe film deposited on spinel(111) (see Figure 5-15b-d).

In contrast, on r-plane sapphire, the structural conversion to fcc (111). Unlike the Ni-Fe film deposited on spinel(100), the Ni-Fe/r-plane sapphire after the hydrogen annealing showed a polycrystalline structure consisting of a number of small grains, which are a mixture of several crystal planes ((100), (110) and so on) without fcc(111) plane. In addition, the conversion of the Ni-Fe/r-plane sapphire to fcc(111) was much faster than that seen in the Ni-Fe/spinel(100). This can be explained by the low crystallinity of the alloy film supported on r-plane sapphire. While spinel(100) has a square-shaped crystal plane, r-plane sapphire has a rectangular shaped surface structure. The former can be matted with fcc(100) plane, but the latter is not suitable for forming the a fcc metal film, resulting in a polycrystalline structure with many small grains that promotes the structural transformation.

The EBSD measurements were also performed for the Fe-rich alloy deposited on c- and r-plane sapphire substrate. The result is displayed in Figure 5-18h-m. Only the alloy film on r-plane sapphire showed the significant change of the crystal structure. However, the density of grain boundaries is higher in all the steps, as compared to Ni-rich alloy. This is similar to the Fe-rich alloy deposited on spinel(100) (see Figure 5-14e). Thus, the lower uniformity of the h-BN sheet seen in the Fe-rich alloy on the sapphire substrate is ascribed to the lower crystallinity of the Fe-rich, Ni-Fe alloy.
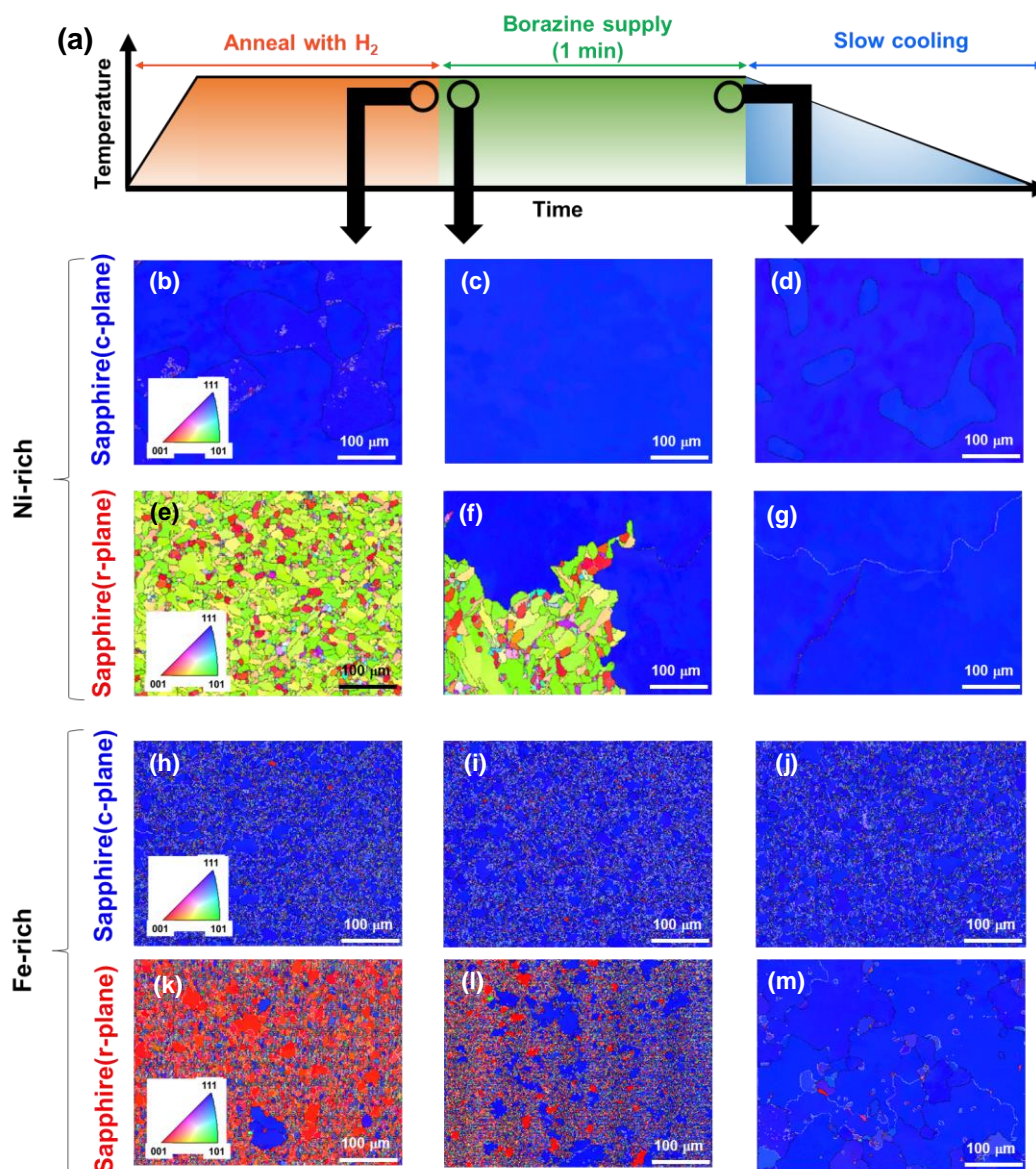
**Figure 5-18.** (a-m) EBSD images for Ni-ich and Fe-rich alloys in 3 steps in CVD scheme. Crystal planes of Ni-Fe/c-plane and r-plane sapphire after 1 hour hydrogen annealing (b,e,h,k), 1 min borazine supply (c,f,I,l), and 30 min borazine supply (d,g,j,m). (n) Crystal plane mapping image with low magnification of Ni-Fe/spinel(100) after 1 min borazine supply.

## 5.4   Conclusions

This chapter presents the effectiveness of the Ni-Fe catalyst for the synthesis of uniform multilayer films. The addition of Ni metal to Fe reduces the amount of the dissolved N atoms and makes balance between B and N atoms dissolved in the catalyst film, contributing to the uniform segregation of multilayer h-BN. In addition, the significant improvement of the crystallinity of the metal catalyst, *i.e.* stabilization of fcc structure and reduction of the density of metal grain boundaries, which also contributes the thickness uniformity of the h-BN. Moreover, a crystal plane of the alloy catalyst was found to be essential for the uniform segregation of multilayer h-BN growth; the fcc(100) plane of the Ni-Fe alloy strongly assists the h-BN segregation combined with its structural change to fcc(111). This was explained by the low packing density in the fcc(100) plane. Further study, such as theoretical calculations and *in situ* measurements, are expected for the deep understanding of this unique h-BN growth process.

The CVD-grown h-BN is proved to be as an ideal insulating substrate for 2D materials, by demonstrating intense and sharp PL spectrum from $WS_2$ grains grown on the CVD-grown h-BN. The important advantage I should emphasize is that the large area availability of the h-BN films owing to the CVD process. The multiple transfer process of exfoliated flakes of various 2D materials has shown great progress. However, it is difficult to prepare large scale devices or device arrays based on mechanical exfoliation. Therefore, the present achievement of the large-area multilayer h-BN synthesis would give strong impact on the 2D materials research and engineering, making practical applications more realistic, due to enhancement of physical properties of 2D materials by h-BN sheets.

# References

1. Kim, K. K. *et al.* Synthesis of monolayer hexagonal boron nitride on Cu foil using chemical vapor deposition. *Nano Lett.* **12**, 161–166 (2012).

2. Guo, N. *et al.* Controllable growth of triangular hexagonal boron nitride domains on copper foils by an improved low-pressure chemical vapor deposition method. *Nanotechnology* **23**, 415605 (2012).

3. Tay, R. Y. *et al.* Growth of large single-crystalline two-dimensional boron nitride hexagons on electropolished copper. *Nano Lett.* **14**, 839–846 (2014).

4. Wu, Q. *et al.* Single crystalline film of hexagonal boron nitride atomic monolayer by controlling nucleation seeds and domains. *Sci. Rep.* **5**, 16159 (2015).

5. Sinha, S., Takabayashi, Y., Shinohara, H. and Kitaura, R. Simple fabrication of air-stable black phosphorus heterostructures with large-area hBN sheets grown by chemical vapor deposition method. *2D Mater.* **3**, 035010 (2016).

6. Uchida, Y., Iwaizako, T., Mizuno, S., Tsuji, M. and Ago, H. Epitaxial chemical vapour deposition growth of monolayer hexagonal boron nitride on a Cu(111)/sapphire substrate. *Phys. Chem. Chem. Phys.* **19**, 8230–8235 (2017).

7. Kidambi, P. R. *et al.* In situ observations during chemical vapor deposition of hexagonal boron nitride on polycrystalline copper. *Chem. Mater.* **26**, 6380–6392 (2014).

8. Lu, G. *et al.* Synthesis of large single-crystal hexagonal boron nitride grains on Cu–Ni alloy. *Nat. Commun.* **6**, 6160 (2015).

9. Lu, G. *et al.* Synthesis of high-quality graphene and hexagonal boron nitride monolayer in-plane heterostructure on Cu–Ni alloy. *Adv. Sci.* **4**, 1700076 (2017).

10. Kim, S. M. *et al.* Synthesis of large-area multilayer hexagonal boron nitride for high material performance. *Nat. Commun.* **6**, 8662 (2015).

11. Caneva, S. *et al.* Controlling catalyst bulk reservoir effects for monolayer

hexagonal boron nitride CVD. *Nano Lett.* **16**, 1250–1261 (2016).

12.     Koepke, J. C. *et al.* Role of pressure in the growth of hexagonal boron nitride thin films from ammonia-borane. *Chem. Mater.* **28**, 4169–4179 (2016).

13.     Jang, S. K., Youn, J., Song, Y. J. and Lee, S. Synthesis and characterization of hexagonal boron nitride as a gate dielectric. *Sci. Rep.* **6**, 30449 (2016).

14.     Lin, W.-H. *et al.* Atomic-scale structural and chemical characterization of hexagonal boron nitride layers synthesized at the wafer-scale with monolayer thickness control. *Chem. Mater.* **29**, 4700–4707 (2017).

15.     Cho, H. *et al.* Growth kinetics of white graphene (h-BN) on a planarised Ni foil surface. *Sci. Rep.* **5**, 11985 (2015).

16.     Dudrová, E., Selecká, M., Burea, R. and Kabátová, M. Effect of boron addition on microstructure and properties of sintered Fe-1.5Mo powder materials. *ISIJ Int.* **37**, 59–64 (1997).

17.     Gorbachev, R. V. *et al.* Hunting for monolayer boron nitride: optical and Raman signatures. *Small* **7**, 465–468 (2011).

18.     Watanabe, K., Taniguchi, T. and Kanda, H. Direct-bandgap properties and evidence for ultraviolet lasing of hexagonal boron nitride single crystal. *Nat. Mater.* **3**, 404–409 (2004).

19.     Tay, R. Y. *et al.* Direct growth of nanocrystalline hexagonal boron nitride films on dielectric substrates. *Appl. Phys. Lett.* **106**, 101901 (2015).

20.     Fu, L. *et al.* Direct growth of $MoS_2$/h-BN heterostructures via a sulfide-resistant alloy. *ACS Nano* **10**, 2063–2070 (2016).

21.     Zhang, Z. *et al.* Direct chemical vapor deposition growth and band-gap characterization of $MoS_2$/h-BN van der Waals heterostructures on Au foils. *ACS Nano* **11**, 4328–4336 (2017).

22.     Okada, M. *et al.* Direct chemical vapor deposition growth of $WS_2$ atomic layers

on hexagonal boron nitride. *ACS Nano* **8**, 8273–8277 (2014).

23. Ago, H. *et al.* Controlled van der Waals epitaxy of monolayer $MoS_2$ triangular domains on graphene. *ACS Appl. Mater. Interfaces* **7**, 5265–5273 (2015).

24. Ago, H. *et al.* Visualization of grain structure and boundaries of polycrystalline graphene and two-dimensional materials by epitaxial growth of transition metal dichalcogenides. *ACS Nano* **10**, 3233–3240 (2016).

25. Kobayashi, Y. *et al.* Growth and optical properties of high-quality monolayer $WS_2$ on graphite. *ACS Nano* **9**, 4056–4063 (2015).

26. Zhu, B., Chen, X. and Cui, X. Exciton binding energy of monolayer $WS_2$. *Sci. Rep.* **5**, 9218 (2015).

27. Wang, Y. *et al.* Strain-induced direct–indirect bandgap transition and phonon modulation in monolayer $WS_2$. *Nano Res.* **8**, 2562–2572 (2015).

28. Swartzendruber, L. J., Itkin, V. P. and Alcock, C. B. The Fe-Ni (iron-nickel) system. *JPE* **12**, 288–312 (1991).

29. Ago, H. *et al.* Epitaxial growth and electronic properties of large hexagonal graphene domains on Cu(111) thin film. *Appl. Phys. Express* **6**, 075101 (2013).

# Chapter 6

# Conclusions and future outlook

## 6.1 Conclusions

In this thesis, controlled CVD growth of h-BN using Cu(111) and Ni-Fe alloy films are demonstrated. A Cu(111) thin film deposited on c-plane sapphire substrate provided epitaxially aligned monolayer h-BN (Chapter 4).[1] The low solubilities of B and N in Cu metal contributed to the formation of monolayer h-BN based on the self-limiting mechanism. The higher stability of N-terminated edges leaded to the formation of triangular h-BN grains with a lateral size around ~5 $\mu$m. SEM and LEED measurements confirmed well-controlled hexagonal lattices of the h-BN sheet whose orientation is registered by the underlying Cu(111). Carrier transport properties of vertically stacked graphene/h-BN heterostructures were also measured, and the result suggested the importance of synthesizing multilayer h-BN to boost the physical properties of other 2D materials, such as graphene and TMDCs.

Being different from the synthesis of monolayer h-BN which is controlled by the self-limiting behavior, controlled synthesis of large-area, multilayer h-BN has been very difficult and thus challenging. Therefore, multilayer h-BN flakes exfoliated from bulk h-BN crystals are now widely used to obtain high performance or novel physics of various 2D materials. In this thesis, for the first time, uniform multilayer h-BN is realized by CVD method using Ni-Fe alloy thin films as a catalyst (Chapter 5).[2] The multilayer h-BN was obtained by controlling the dissolution and segregation processes of B and N atoms. Systematic investigation on effects of the crystal structure of Ni-Fe alloy catalyst was

performed, and it was revealed that the fcc(100) plane of the Ni-Fe alloy is essential to accelerate the segregation of h-BN. During the segregation, the Ni-Fe alloy dynamically changes its crystalline plane to fcc(111). The present work also indicates that the alloy on r-plane sapphire as well as spinel(100) substrates are suitable substrate to stimulate the transformation to fcc(111) phase during the h-BN growth. Moreover, the CVD-grown multilayer h-BN was shown to increase the PL from the $WS_2$ by reducing influences from the $SiO_2$ substrate, opening the possibility of utilizing the multilayer h-BN for future applications.

## 6.2   Future outlook

As discussed in Chapters 1 and 4, multilayer h-BN has a large band gap, the atomically smooth and dangling bond-free surface, high chemical and thermal stability, and high energy optical phonons. The h-BN is an excellent insulating material that can realize intrinsic physical properties of various atomically thin 2D films, such as graphene and TMDCs. Therefore, the production of wafer-scale, high-quality h-BN is highly desired, because it offers an ideal platform for 2D materials from the viewpoints of both fundamental science and industrial applications.

Exfoliated h-BN flakes peeled off from the bulk h-BN crystal has given a large impact on the 2D materials research and applications, because h-BN-based vdW heterostructures showed excellent properties.[3,4] Ultrahigh mobility graphene realized by encapsulation with h-BN layers is a promising candidate for Hall sensors and radio-frequency (RF) transistors.[5,6] This is because the graphene is protected from gas adsorption and chemicals, such as polymer residue, as well as from the charges and optical phonons existing on the $SiO_2$ substrate.   Also, 2D semiconductors encapsulated

by h-BN is expected as excellent switching devices for digital logic circuits due to their relatively high mobility, suitable band gaps, and atomically thin 2D structure.[7–10] Also, h-BN acts as a gas barrier film which prevents degradation of air- or light-sensitive 2D materials, such as black phosphorous and TMDCs. However, scalable fabrications of these vdW heterostructures are still very challenging and that hinders practical applications based on 2D materials.

The scalable approach requires high-quality h-BN sheets and highly sophisticated assembly techniques for making vdW heterostructures. This is also deeply related to development of transfer methods of h-BN from metal catalysts. Thus, defect-free large-area transfer method and/or catalyst-free growth will become important. In addition, as the commercial products require a very low variation in properties, such as mobility.

As demonstrated in Chapter 5, the growth of uniform and large-area h-BN has been achieved in the present thesis, but there is still space to improve the quality, such as crystallinity, lattice orientation, wrinkles and ripples, and uniformity of the film. In particular, a perfectly aligned multilayer h-BN sheet with well-defined thickness is essential to achieve uniform performance of devices using graphene and other 2D materials. This is because some of physical properties of 2D materials strongly depend on stacking angle between a 2D material and h-BN, because the interference or coupling of electronic potentials of two layers alter the physical properties of the 2D material (known as moiré effect).[11–14] Therefore, the development of a large-scale stacking method with controlled orientations is expected together with the progress of the large-scale synthesis of functional 2D materials.

In 2010, C. R. Dean et al demonstrated a versatile multiple transfer technique.[23] This method has been improved and now is called as a "pick-and-lift" method, which utilizes

vdW interaction to pick and assemble 2D materials. This enables us to make multiple stacking and orientation control with reduced contamination between each layer.[4] More recently robotics has been introduced in the transfer process instead of the manual transfer. However, there are limitations of the sizes in the stacking of exfoliated flakes. Direct CVD growth of 2D materials on h-BN can be another route to obtain vdW heterosatructures.[15–22] However, the uniform growth of 2D materials, such as TMDCs, on h-BN is still a challenging task. Therefore, combining CVD-grown 2D materials on a suitable substrate with advanced transfer techniques is expected to give an excellent scalable way to realize high performance of h-BN-based vdW heterostructures in industrial scale.

## References

1. Uchida, Y., Iwaizako, T., Mizuno, S., Tsuji, M. and Ago, H. Epitaxial chemical vapour deposition growth of monolayer hexagonal boron nitride on a Cu(111)/sapphire substrate. *Phys. Chem. Chem. Phys.* **19**, 8230–8235 (2017).

2. Uchida, Y. *et al.* Controlled growth of large-area uniform multilayer hexagonal boron nitride as an effective 2D substrate. *ACS Nano* **12**, 6236-6244 (2018).

3. Geim, A. K. and Grigorieva, I. V. Van der Waals heterostructures. *Nature* **499**, 419–425 (2013).

4. Novoselov, K. S., Mishchenko, A., Carvalho, A. and Neto, A. H. C. 2D materials and van der Waals heterostructures. *Science* **353**, aac9439 (2016).

5. Wang, L. *et al.* One-dimensional electrical contact to a two-dimensional material. *Science* **342**, 614–617 (2013).

6. Banszerus, L. *et al.* Ultrahigh-mobility graphene devices from chemical vapor deposition on reusable copper. *Sci. Adv.* **1**, e1500222 (2015).

7. Cui, X. *et al.* Multi-terminal transport measurements of $MoS_2$ using a van der Waals heterostructure device platform. *Nat. Nanotechnol.* **10**, 534–540 (2015).

8. Xu, S. *et al.* Universal low-temperature Ohmic contacts for quantum transport in transition metal dichalcogenides. *2D Mater.* **3**, 021007 (2016).

9. Chen, X. *et al.* High-quality sandwiched black phosphorus heterostructure and its quantum oscillations. *Nat. Commun.* **6**, 7315 (2015).

10. Li, L. *et al.* Quantum Hall effect in black phosphorus two-dimensional electron system. *Nat. Nanotechnol.* **11**, 593–597 (2016).

11. Hunt, B. *et al.* Massive Dirac fermions and hofstadter butterfly in a van der Waals heterostructure. *Science* **340**, 1427–1430 (2013).

12. Dean, C. R. *et al.* Hofstadter's butterfly and the fractal quantum Hall effect in moiré superlattices. *Nature* **497**, 598–602 (2013).

13. Ribeiro-Palau, R. *et al.* Twistable electronics with dynamically rotatable heterostructures. *Science* **361**, 690–693 (2018).

14. Yankowitz, M. *et al.* Dynamic band-structure tuning of graphene moiré superlattices with pressure. *Nature* **557**, 404-408 (2018).

15. Yang, W. *et al.* Epitaxial growth of single-domain graphene on hexagonal boron nitride. *Nat. Mater.* **12**, 792–797 (2013).

16. Wang, M., Jang, S. K., Song, Y. J. and Lee, S. CVD growth of graphene under exfoliated hexagonal boron nitride for vertical hybrid structures. *Mater. Res. Bull.* **61**, 226–230 (2015).

17. Tang, S. *et al.* Silane-catalysed fast growth of large single-crystalline graphene on hexagonal boron nitride. *Nat. Commun.* **6**, 6499 (2015).

18. Gao, T. *et al.* Temperature-triggered chemical switching growth of in-plane and vertically stacked graphene-boron nitride heterostructures. *Nat. Commun.* **6**, 6835 (2015).

19.    Okada, M. *et al.* Direct chemical vapor deposition growth of WS$_2$ atomic layers on hexagonal boron nitride. *ACS Nano* **8**, 8273–8277 (2014).

20.    Kobayashi, Y. *et al.* Growth and optical properties of high-quality monolayer WS$_2$ on graphite. *ACS Nano* **9**, 4056–4063 (2015).

21.    Wang, S., Wang, X. and Warner, J. H. All Chemical vapor deposition growth of MoS$_2$:h-BN vertical van der Waals heterostructures. *ACS Nano* **9**, 5246–5254 (2015).

22.    Fu, L. *et al.* Direct Growth of MoS$_2$/h-BN heterostructures via a sulfide-resistant alloy. *ACS Nano* **10**, 2063–2070 (2016).

23.    Dean, C. R. *et al.* Boron nitride substrates for high-quality graphene electronics. *Nat. Nanotechnol.* **5**, 722–726 (2010).

# Acknowledgement

I would like to express my special appreciation to Prof. Hiroki Ago, my Ph.D. supervisor, for all the support for my Ph.D. He has always been supportive even when I face problems. His valuable suggestions with his expert knowledge have been very helpful to progress my studies. Also, I have experienced various valuable opportunities including joining conferences, internships for his support. I am really grateful for giving me such great opportunities. Also, I am thankful to Prof. Masaharu Tsuji who gives me various valuable opinions to my studies.

I want to express my gratitude to collaborators in my Ph.D. study. Prof. Seigi Mizuno kindly supported my LEED measurements. Associate Prof. Masatoshi Mitsuhara and Assistant Prof. Shigeto Yamasaki helped me to do TEM observation and EBSD measurement. Also, Mr. Tasuku Iwaizako supported my first work when I was first year master course student. Mr. Sho Nakandakari significantly helped to progress my second work. Mr. Kenji Kawahara has always helped me with his valuable knowledge.

I would like to thank lab members. Pablo san has encouraged and supported me to study. In particular, what I went to Kawagoe girls high school for lecture assistance with Pablo san is a good memory. Kawahara san always kindly supported me to do research. I have learned a lot from kawahara san. Thanks to various support, especially clerical support, by Hino san and Endo san, I have comfortably spent my academic life. Moreover, I have experienced wonderful opportunities with students. This is really a good memory.

I gratefully thank to Green Asia program and Japan Society for the Promotion of Science for financial support to do study. Finally, I really appreciate my parents for all the support for my life.

# List of publication

## Publications included in this thesis

Chapter 4

**Yuki Uchida**, Tasuku Iwaizako, Seigi Mizuno, Masaharu Tsuji, and Hiroki Ago

"Epitaxial chemical vapour deposition growth of monolayer hexagonal boron nitride on a Cu(111)/sapphire substrate"

*Phys. Chem. Chem. Phys.* **19**, 8230–8235 (2017).

Chapter 5

**Yuki Uchida**, Sho Nakandakari, Kenji Kawahara, Shigeto Yamasaki, Masatoshi Mitsuhara, and Hiroki Ago

"Controlled growth of large-area uniform multilayer hexagonal boron nitride as an effective 2D substrate"

*ACS Nano* **12**, 6236-6244 (2018).

## Publications not included in this thesis

H. Ago, Y. Ohta, H. Hibino, D. Yoshimura, R. Takizawa, **Y. Uchida**, M. Tsuji, T. Okajima, H. Mitani, and S. Mizuno

"Growth dynamics of single-layer graphene on epitaxial Cu surfaces"

*Chem. Mater.* **27**, 5377-5385 (2015).

H. Ago, S. Fukamachi, H. Endo, P. Solís-Fernández, R. M. Yunus, **Y. Uchida**, V. Panchal, O. Kazakova, M. Tsuji

"Visualization of grain structure and boundaries of polycrystalline graphene and two-dimensional materials by epitaxial growth of transition metal dichalcogenides" *ACS Nano*, **10**, 3233-3240 (2016).